

SIMULATION OF MULTI-LAYER-LIQUID SLOSING EFFECTS ON VESSEL
MOTIONS BY USING MOVING PARTICLE SIMULATION

A Dissertation

by

KYUNG SUNG KIM

Submitted to the Office of Graduate and Professional Studies of
Texas A&M University
in partial fulfillment of the requirements for the degree of

DOCTOR OF PHILOSOPHY

Chair of Committee,	Moo-Hyun Kim
Committee Members,	Jun Zhang
	Richard Mercier
	David Brooks
Interim Head of Department,	Robin Autenrieth

May 2014

Major Subject: Ocean Engineering

Copyright 2014 Kyung Sung Kim

ABSTRACT

The coupling and interactions between ship motions and inner-liquid tank sloshing have been investigated by a coupled program between ship motion and sloshing analysis programs. For the sloshing program, Moving Particle Simulation (MPS), which is based on the Lagrangian approach, is used. This sloshing program is validated through comparisons with corresponding experimental results both qualitatively and quantitatively. This validated MPS method has been extended to multi-liquid systems by adding newly adopted models which are buoyancy-correction, surface tension, and boundary conditions at interfaces. Each new model is validated either mathematically or theoretically for comparison. Moreover, a new tracing method of interface particles is suggested by modifying the conventional free-surface searching method in MPS for a single-liquid system. The newly developed MPS for multi-liquid system has been tested for three-liquid sloshing and the obtained results have been compared with the corresponding experimental results. The verified MPS system is coupled with a ship motion program to investigate the sloshing effects on vessel motions. The coupled program was applied to two sloshing tanks, partially filled with fresh water, on a barge-type FPSO. The simulation results were compared with experiments by MARIN and showed good agreement. The most noticeable coupling effects on vessel motions show that the peak frequencies are split and shifted, especially in roll motions. Furthermore, comparison between cases of liquid- and rigid-cargo showed the importance of sloshing effects more clearly. The developed program was also applied to the multi-liquid

sloshing problem to consider the wash-tank. In the case of the multi-liquid-layer, there are more than one sloshing natural frequencies, so the relevant physics can be much more complicated compared to the case of a single-liquid-tank. The oscillations of the interfaces have different amplitudes and frequencies. Since the wash-tank contained multi-liquids, short waves at the interface were generated due to Kelvin-Helmholtz instability and the phenomenon was successfully reproduced by the developed MPS-simulation technique.

DEDICATION

This dissertation is dedicated,
with eternity love and infinity respect,
to my family.

Parents

Sung Tae Kim, Chun Ja Kim

Wife

Ki Ha Kim

Daughter

Hailey Kim

ACKNOWLEDGEMENTS

I would like to express my sincere gratitude to my advisor, Prof. Moo-Hyun Kim. Without his help and guidance, this thesis would not have been achieved. His intellectual insight and knowledge were most useful all-around this thesis. I have been extremely lucky to have an advisor who cared so much about my research and encouraged me continuously.

I would like to appreciate my committee members, Dr. Jun Zhang, Dr. Richard Mercier, and Dr. David Brooks, their guidance and support throughout the course of this research. Their excellent service as my academic committee advisors has broadened my view of research.

I would like to express my gratitude to Prof. Jong-Chun Park, and Dr. Byung-Hyuk Lee. They were willing to share their knowledge for numerical method, and always helped me out from abstruse problem. Mr. Han-Sang Kim also help me in many ways. I also owe many thanks to all of the members in Pusan National University alumni in TAMU for encouraging and sharing every moment with my family.

Thanks also go to my friends and colleagues and the department faculty and staff for making my time at Texas A&M University a great experience.

Finally, I would like to express my special gratitude to my parents. Their unconditional support and love can lead me. I would like to express my special love to my wife Ki-Ha Kim and my daughter Hailey Kim. Their patience can make me comport and concentrate to my work.

TABLE OF CONTENTS

	Page
ABSTRACT	ii
DEDICATION	iv
ACKNOWLEDGEMENTS	v
TABLE OF CONTENTS	vi
LIST OF FIGURES	viii
LIST OF TABLES	xii
CHAPTER I INTRODUCTION AND LITERATURE REVIEW	1
1. Introduction	1
2. Scope of Research	4
3. Literature Review	6
CHAPTER II DYNAMICS OF FLOATING STRUCTURE	9
1. Boundary Value Problem of Surface Wave	9
2. Wave Loads on Structures	12
2.1 Diffraction and Radiation Theory	12
2.2 First-order Boundary Value Problem (Linear Boundary Value Problem) ...	13
2.3 The First-order Hydrodynamic Forces and Moments	15
3. Motion of Floating Structure	19
3.1 Wave Loads	19
3.2 Morrison's Formula	22
3.3 Solution for Frequency Domain	22
3.4 Solution of Time Domain	24
CHAPTER III MOVING PARTICLE SIMULATION FOR SINGLE-LIQUID	28
1. Governing Equation	29
2. Kernel Function	29
3. Gradient Model	32
4. Divergence Model	35
5. Laplacian Model	35
6. Incompressibility Model	37
7. Boundary Condition	40

7.1 Free-surface Boundary Condition	40
7.2 Wall Boundary Condition	41
8. Collision Model.....	42
9. Hydrostatic Correction Model.....	43
CHAPTER IV MOVING PARTICLE SIMULATION FOR MULTI-LIQUID	47
1. Interface Searching Model	47
2. Boundary Conditions at Interface	49
3. Buoyancy-Correction Model.....	51
4. Surface Tension Model	54
CHAPTER V APPLICATIONS	57
1. Applications for Single-Liquid MPS.....	57
1.1 Broken Dam	57
1.2 Sloshing Tank for Single-Liquid.....	61
2. Advancement of MPS to Multi-Liquid Problems	65
2.1 Interface Particle Tracking	65
2.2 Buoyancy Force Correction	68
2.3 Surface Tension.....	74
2.4 Sloshing Tank for Multi-Liquid	77
2.5 Kelvin-Helmholtz Instability at Interface	89
2.6 Interface of High Density Contrast	98
3. Vessel-Sloshing Interaction Simulation	101
3.1 Single-Liquid Vessel-Sloshing Interaction	101
3.2 Multi-Liquid Vessel-Sloshing Interaction.....	117
CHAPTER VI CONCLUSION.....	134
REFERENCES.....	139

LIST OF FIGURES

	Page
Figure 1 Schematic concept of kernel function (a) and (b) plot of kernel function	30
Figure 2 Schematic concept of gradient model	34
Figure 3 Example of Laplacian model	36
Figure 4 The free surface layer (a) without and (b) with hydrostatic correction	45
Figure 5 Example for identification of HSC particles	46
Figure 6 Interface particle and imaginary reference particle	51
Figure 7 Self-buoyancy calculations	53
Figure 8 (a) Measurement of curvatures and (b) calculation of normal unit vector for surface tension	56
Figure 9 Schematic model for broken dam	58
Figure 10 Comparison of snapshots of broken dam	59
Figure 11 Pressure history at reference point (a) $l_0 = 0.005$ m (b) $l_0 = 0.01$ m, 0.005 m, and 0.0025 m	61
Figure 12 Schematic model for the sloshing problem	63
Figure 13 Snapshots of sloshing under harmonic oscillation	63
Figure 14 Pressure history comparison between experiment and numerical simulation at (a) $T=1.3$ sec and (b) $T=1.5$ sec	64
Figure 15 Tracing of interface particles	66
Figure 16 Tracing of interface particle under violent motion	67
Figure 17 Schematic model for oil particle rising	70
Figure 18 Vertical position of oil particle (a) $l_0 = 0.01$ and (b) $l_0 = 0.005$	70

Figure 19 Schematic model of lateral oil leaking.....	72
Figure 20 Snapshots of lateral oil spill.....	73
Figure 21 Oil height loss	74
Figure 22 Schematic model for surface tension test on X-Y plane.....	76
Figure 23 Examples of droplet vibration.....	76
Figure 24 Normal vectors of droplet	77
Figure 25 Direction of force.....	77
Figure 26 Schematic model for three liquid sloshing problem	79
Figure 27 Result of free decay test: comparison by tilting angle at (a) CW- (b) WD- interfaces and (c) free-surface; comparison between viscous and inviscid fluid at (d) CW- (e) WD-interfaces and (f) free surface	81
Figure 28 Elevation of interfaces with experiment	84
Figure 29 Interface oscillation for 1-degree roll at 1.83-rad/s at (a) left wall of tank and (b) mid tank.....	84
Figure 30 Snapshots of multi-liquid sloshing tank at time (a) 20 sec and (b) 33 sec.....	85
Figure 31 Spectra of interface at (a) left wall and (b) center	85
Figure 32 Comparisons of interface oscillations for convergence test with different particle size	86
Figure 33 Comparisons of spectra for convergence test	87
Figure 34 Snapshots of violent motion without surface tension model	89
Figure 35 Snapshots of violent motion with surface tension model	89
Figure 36 Schematic model for Kelvin-Helmholtz Instability	91
Figure 37 Example of Kelvin-Helmholtz Instability.....	93
Figure 38 Example of Kelvin-Helmholtz Instability (a) full view (b) enlarged view.....	93

Figure 39 Snapshots of Case I at time 17.5 sec (a) entire and (b) magnified	95
Figure 40 Snapshots of Case II at time 17.5 sec (a) entire and (b) magnified	95
Figure 41 Snapshots of Case III at time 17.5 sec (a) entire and (b) magnified.....	96
Figure 42 Snapshots of Case IV at time 17.5 sec (a) entire and (b) magnified.....	96
Figure 43 Snapshots of Case V at time 17.5 sec (a) entire and (b) magnified.....	97
Figure 44 Snapshots of Case VI at time 17.5 sec (a) entire and (b) magnified.....	97
Figure 45 Snapshots of Case VII at time 17.5 sec (a) entire and (b) magnified	98
Figure 46 Schematic model for sloshing with floater	99
Figure 47 Pressure history at density contrast (1000:300).....	100
Figure 48 Pressure history at density contrast (1000:100).....	100
Figure 49 Pressure history at density contrast (1000:50).....	101
Figure 50 : (a) Model of MARIN-FPSO with sloshing tanks (b) model for panel method	104
Figure 51 Comparisons of simulated and measured RAOs without inner liquids	105
Figure 52 Snapshots of liquid motions and pressure field inside an 18% filled tank	107
Figure 53 comparisons of simulated and measured RAOs of MARIN-FPSO with various filling ratios	108
Figure 54 Comparisons of roll RAOs for $H_s=2.5\text{m}$, 5.0m , and 10m ($T_p=12\text{s}$; 0.52 rad/s) for 18% filled tanks.....	111
Figure 55 Comparisons of roll RAOs for $H_s=2.5\text{m}$, 5.0m , and 10m ($T_p=12\text{s}$; 0.52 rad/s) for 56% filled tanks.....	111
Figure 56 Representative nonlinear snapshots for inner liquid of 18% filled tank with $H_s=5\text{m}$ and $T_p=12\text{s}$	112
Figure 57 Representative nonlinear snapshots for inner liquid of 56% filled tank with $H_s=5\text{m}$ and $T_p=12\text{s}$	112
Figure 58 Comparisons of roll RAOs for $H_s=2.5\text{m}$, 5.0m , and 10m ($T_p=8\text{s}$; 0.78 rad/s) for 56% filled tanks.....	113

Figure 59 Comparison of displacement and RAO between liquid- and rigid-cargo with 18% filled tanks	115
Figure 60 Comparison of displacement and RAO between liquid- and rigid-cargo with 37% filled tanks	116
Figure 61 Comparison of displacement and RAO between liquid- and rigid-cargo with 56% filled tanks	117
Figure 62 Schematic model for wash-tank.....	119
Figure 63 Spectra of wash-tank from free decay test at (a) left-wall and (b) center.....	120
Figure 64 Elevations of interface for beam-wave	122
Figure 65 Spectra of interface for beam-wave	122
Figure 66 Elevations of interface for head-wave	123
Figure 67 Spectra of interface for head-wave	123
Figure 68 Displacements of vessel at beam-sea condition.....	125
Figure 69 Displacement of vessel at head-sea condition	126
Figure 70 Comparisons of RAOs	127
Figure 71. Snapshots of inner liquid cargo in wash tank	129
Figure 72 Snapshots of inner solid cargo in wash tank.....	129
Figure 73 Roll Motion history for liquid- and rigid-cargo.....	130
Figure 74 Comparison of roll RAO between liquid- and rigid-cargo	130
Figure 75 Roll Displacement under operational condition	132
Figure 76 Comparisons of roll RAOs between severe and operational condition	132
Figure 77 Elevation of interfaces under operational condition	133
Figure 78 Spectra of interfaces under operational condition	133

LIST OF TABLES

	Page
Table 1 Table of Parameters Used	67
Table 2 Properties of Fluids for Oil Leaking Simulation.....	72
Table 3 Properties of Liquids	78
Table 4 Angular Frequencies of Natural Modes	82
Table 5 Table of Wavenumbers and Relative Velocities for CW Interface.....	92
Table 6 Table of Wavenumbers and Relative Velocities for WD Interface	92
Table 7 Test Cases for Kelvin-Helmholtz Instability.....	94
Table 8 Circumstance Conditions	102
Table 9 Characteristics of Sloshing Tanks.....	102
Table 10 Principal Particulars of FPSO (bare hull) and Mooring System.....	103
Table 11 Natural frequencies of FPSO and Sloshing Tanks.....	109
Table 12 Angular Frequencies of Natural Modes of Wash Tank.....	120
Table 13 Simulation Conditions of Vessel motion	120
Table 14 Properties of Inner Fluids.....	121
Table 15 Specifications of Wash Tank.....	121

CHAPTER I

INTRODUCTION AND LITERATURE REVIEW

1. Introduction

Free surface fluid flows are significantly important for industrial and environmental applications. Especially, in the sloshing problem, impact loads and violent motions of fluid, which are induced by sloshing, can generate many non-linear problems such as wave breaking, splashing, overturning, etc. Nevertheless, only a few studies of these topics can be found. Moreover, in most circumstances, theoretical analysis is often limited due to assumptions such as small deformations of free surface. In this regard, dynamics of such flows have been studied either theoretically or numerically. In the numerical studies, potential theory shows good agreement when a free surface has small deformations with irrotationality. However, in case of harsh conditions, which may involve high rotational angles or large translational displacement, these assumptions break down due to wave breaking, fragmentation, and coalescence.

By solving Navier-Stoke's equation, mainly with CFD (Computational Fluid Dynamics), free surface fluid flow can be simulated. In most cases, The Eulerian approach, which uses fixed control volume to solve Navier-Stoke's equation, is used to simulate fluid flows with free surface. However, since the proposed Navier-Stoke's equation is for a fixed grid system, it needs to be coupled with a mathematical treatment of the free surface. Despite this special treatment, the grid system has a defect due to numerical diffusion from the discretization of the advection terms. A few algorithms

have been suggested to account for the numerical diffusion. However, it is complicated to implement these sophisticated algorithms into the computational procedure for free surface flows.

Recently, particle methods based on The Lagrangian approach have been applied to many engineering/industrial applications including the free surface flows. Using the particle method based on the Lagrangian approach, the advection term can be directly calculated without numerical diffusion. Furthermore, the particle method uses discrete particles. Thus, there is no connection between particles which make the particle method ideal for simulations of large free surface deformations and discontinued moving from violent fluid motions. In this regard, particle methods have an advantage over the conventional CFD method which is based on a grid system. However, since particle methods are relatively new in the flow analysis field, more research is required to extend their applicability and performance with proper accuracy.

During recent decades, particle methods have been investigated to improve their accuracy for simulations including free-surface flows, impact loads, etc., and were validated with both experiments and theory. Among the several particle methods, SPH (Smoothed Particle Hydrodynamics; Lucy, 1977; Gingold and Monaghan, 1977) and MPS (Moving Particle Simulation; Koshizuka and Oka, 1996) are most widely used. In this thesis, MPS has been selected. The decision was supported by the fact that the Navier-Stoke's equation is used for the governing equation which guarantees momentum conservation and viscous effects. The MPS was originally proposed by Koshizuka and Oka (1996) for incompressible viscosity flows. The improvements of the Possion

equation, gradient/collision model and tracing method of free surface particles were archived by revisiting the original formulation. Through these efforts, the non-physicality has been removed or reduced. The improved MPS is demonstrated through the simulation of numerous non-linear fluid-dynamics problems such as a dam breaking or sloshing.

Recently, the demand for multi-liquid systems has increased dramatically, and so has that for its analyses. The oil/gas separators, for example, contain multiple fluids in the tank which need to be separated from one another. This stimulated the studies on MPS for multi-liquid systems. However, thus far there has been no consideration for the interaction between liquid and container movement such as sloshing. Moreover, there has been no effort to define the interface between the different liquids except for the free surface. In addressing these shortcomings with MPS, interface boundary conditions have been applied as well as free surface boundary conditions. The author suggests that the tracing method is used to achieve this.

In applying MPS to investigate the aforementioned multi-liquid system, numerical instability is prone to occur due to a sudden change in physical quantities including density variation. Consequently, many problems arise; two of which the most critical are grid oscillation and false buoyancy due to numerical error. To account for these, a surface tension model and buoyancy correction model were used, respectively. The newly developed MPS for multi-liquid system has been compared with numerous examples, experimentally and theoretically, such as rising/terminal velocity of oil drop, multi-liquid sloshing, etc.

The present thesis aims to achieve dynamic coupling between ship motion and single- or multi-liquid sloshing using MPS. This allows for back and forth feedback between the ship motions and the sloshing effects. Furthermore, by using the MPS method as described, conventionally ignored phenomenon such as overturning, wave breaking, and splashing, all of which occur at interface and free surface, can be considered. The results have been compared with the experiments, both with and without sloshing effects.

2. Scope of Research

The main objective of the present research is to couple ship motions and sloshing effects by using MPS. In order to analyze ship motions, the BEM based 3-D time domain potential program was used including mooring and riser effects called CHARM3D (Arcandra, 2001). All corresponding hydrodynamic coefficients were obtained by a 3-D panel program WAMIT (Lee, 1999). For the sloshing analysis, the MPS, which is originally suggested by Koshizuka et al (1996) for incompressible viscosity fluid, is used. The original MPS has been developed for more accurate simulation by many researchers. The newly developed MPS by author for single- and multi-liquid and ship motion program was coupled by kinematic and dynamic relations. The entire procedure of the present research is de scribed below by categories:

1. Proposing improved MPS method for single-liquid problems
 - Most updated MPS method is described.

- Hydrostatic pressure correction model is suggested to increase simulation accuracy
 - Developed MPS is validated by experiments
2. Proposing advanced MPS method for multi-liquid problems
 - Interface searching method is suggested
 - Boundary condition at interface is developed
 - Buoyancy correction and surface tension models are employed to reduce numerical instabilities.
 - MPS for the multi-liquid system is validated by experiments and theory
 3. Coupling between the single-liquid sloshing program and ship motion program
 - The improved MPS for single-liquid program is coupled with the ship motion program
 - The coupled program was validated by experiments considering sloshing effects.
 4. Coupling between multi-liquid sloshing program and ship motion program
 - Developed MPS for multi-liquid system was coupled with ship motion program.
 - The coupled program was used to investigate inner fluids motions of wash tank.

Through the above procedures, a fully dynamic coupling program between the ship motions and multi-liquid sloshing program is achieved by using MPS which can

estimate resonant of ship motion including sloshing effects and properly predict liquid motions in liquid tanks.

3. Literature Review

The MPS was originally proposed by Koshizuka and Oka (1996). However, since the original MPS has defects such as non-physicality of particle interaction models including the Poisson pressure equation, pressure gradient and collision models, and the searching method for free surface particles. In order to reduce non-physical pressure fluctuation, multi-terms of the Poisson source is suggested by Toyota et al. (20XX). Lee et al.(20XX) have investigated for a proper method of tracing free surface particles with multi-condition of judgment and improved collision model with appropriate parameters using both numerical and theoretical approaches. The surface tension model is proposed by Nomura et al (2001), Zhang et al (2007) and Duan et al (2003).

The MPS system has been extended to multi-liquid system by many researchers. Shirakawa et al. (2001) have suggested a buoyancy correction model. They claimed that buoyancy force can be underestimated due to the numerical configuration disorder which can cause an indistinct pressure head. The correction term of buoyant is added into the pressure gradient model. Shakibaeinia et al (2012) investigated multiphase flows considering weakly compressibility. Applying weak compressibility to transient areas, which are near the interface between different liquids, can suppress numerical instabilities caused by the multi-liquid system. High density contrast problems such as liquid-air problems have been studied by Khayyer et al (2013). The sudden density

change causes numerical oscillations, thus averaged density within an effective range is suggested.

The 3D panel method based on linear potential theory in the frequency domain, WAMIT, has been studied by Lee (1995). The radiation and diffraction problem can be solved in the frequency domain by using WAMIT; then all hydrodynamic coefficients are obtained such as added mass, damping coefficients, and mean drift forces and moments. All corresponding forces and moments are transferred by using the inverse Fourier Transform to simulate vessel motions including viscous damping in the time domain (Kim et al. 1999).

The coupling method between ship motion and sloshing in the frequency domain has been studied by Molin et al. (2002), Malenica (2003), and Newman (2005). Park et al. (2005) calculated sloshing behavior with ship motion under irregular wave condition without coupling. Lee et al. (2011) studied fully dynamic coupling by using the sloshing program based on the VOF method. Fully dynamic coupling between the single-liquid sloshing program using MPS and ship motion program was achieved by Kim et al. (2011). However, sloshing problems studied by the multi-layer-liquid system have rarely been attempted. Two-liquid-layer sloshing in a rectangular tank was theoretically and experimentally studied by La Rocca et al. (2005). Molin et al. (2012) investigated three-liquid-layer sloshing and their numerical simulations were compared against their experiments. Both potential theory and VOF simulations were used in their numerical predictions. In this paper, a new MPS method has been developed for the multi-liquid-

layer system and the simulation results were compared to the three-liquid-layer-sloshing experiments by Molin et al. (2012).

In present the study, the MPS for multi-liquid sloshing has been validated by comparison with experiments by Molin et al. (2012); by revisiting Kim et al. (2011), coupled program between ship motions and sloshing phenomenon can be developed to account for multi-liquid sloshing.

CHAPTER II

DYNAMICS OF FLOATING STRUCTURE

1. Boundary Value Problem of Surface Wave

In order to derive wave theory, a Boundary Value Problem with dynamic and kinematic conditions is needed. Several assumptions are employed stating that the fluid is incompressible, inviscid, and irrotational. With these assumptions, velocity vectors and pressures are expressed by using velocity potential.

$$\vec{u} = i \frac{\partial \Phi}{\partial x} + j \frac{\partial \Phi}{\partial y} + k \frac{\partial \Phi}{\partial z} \quad (2.1)$$

$$p = -\rho g z - \rho \frac{\partial \Phi}{\partial t} - \frac{1}{2} (\Phi_x^2 + \Phi_y^2 + \Phi_z^2) \quad (2.2)$$

where, \vec{u} is velocity vectors in three-dimensional domain with respect to x , y , and z . p is pressure in the fluid field using the Bernoulli's equation, ρ is fluid density, and g is gravitational acceleration. The equation of motion of fluid can be expressed by the Laplace equation with velocity potential.

$$\nabla^2 \Phi = \frac{\partial^2 \Phi}{\partial x^2} + \frac{\partial^2 \Phi}{\partial y^2} + \frac{\partial^2 \Phi}{\partial z^2} = 0 \quad (2.3)$$

In order to solve Eq. (2.3), bottom, kinematic free-surface, and dynamic free-surface boundary conditions are required. Assuming the sea bed is impermeable, the bottom boundary condition can be expressed as follow:

$$\frac{\partial \Phi}{\partial z} = 0 \quad \text{at } z = -d \quad (2.4)$$

where, d is water depth and a positive sign for upward and zero at mean water level. The Kinematic free-surface boundary condition represent that fluid particle is assumed to remain on the free-surface:

$$\frac{\partial \eta}{\partial t} + u \frac{\partial \eta}{\partial x} + v \frac{\partial \eta}{\partial y} + w \frac{\partial \eta}{\partial z} = 0 \quad \text{at } z = \eta(x, y, z) \quad (2.5)$$

where, $\eta(x, y, z)$ is the free-surface elevation in the spatial coordinate. The dynamic free-surface boundary condition states that the pressure on the free-surface is constant as equal to atmosphere pressure. In general, the atmosphere pressure is zero on the free-surface.

$$\rho \frac{\partial \Phi}{\partial t} + \frac{1}{2} (\phi_x^2 + \phi_y^2 + \phi_z^2) + \rho g z = 0 \quad \text{at } z = \eta(x, y, z) \quad (2.6)$$

Since the Laplace equation contains non-linear terms of free-surface boundary conditions, the perturbation method is popularly employed to solve it. In this case, the wave motion is assumed to have very small amplitude, thus this approximated solution can be partially satisfied.

By using the perturbation method, the linear and second-order wave equations are obtained with the velocity potential, and with that, the wave elevation is obtained as follows:

$$\Phi^{(1)} = \text{Re} \left[-\frac{igA \cosh k(z+d)}{\omega \cosh kd} \right] e^{i(kx \cos \theta + ky \sin \theta - \omega t)} \quad (2.7)$$

$$\eta^{(1)} = A \cos(kx \cos \theta + ky \sin \theta - \omega t) \quad (2.8)$$

$$\Phi^{(2)} = \text{Re} \left[-\frac{3}{8} \omega A^2 \frac{\cosh 2k(z+d)}{\sinh^4 kd} \right] e^{i(2k \cos \theta + 2ky \sin \theta - 2\omega t)} \quad (2.9)$$

$$\eta^{(2)} = A^2 \frac{\cosh kd}{\sinh^3 kd} \cos(2kx \cos \theta + 2ky \sin \theta - 2\omega t) \quad (2.10)$$

where, ω is the wave frequency and θ is the incident wave angle. Since the real sea state is fully developed by wind and current, it is irregular and can be described by using Pierson-Moskowitz and JONSWAP (Joint North Sea Wave Observation Project) which are commonly used by ocean engineers. The wave spectrum $S(\omega)$, which can be obtained by combining a reasonably large number of linear wave components, N , with random phases, is used to simulate irregular waves.

$$\begin{aligned} \eta(x, y, z) &= \sum_{j=1}^N A_j \cos(k_j x \cos \theta + k_j y \sin \theta - \omega_j t + \varepsilon_j) \\ &= \text{Re} \left[\sum_{j=1}^N A_j e^{i(k_j x \cos \theta + k_j y \sin \theta - \omega_j t + \varepsilon_j)} \right] \end{aligned} \quad (2.11)$$

where, A_j is the wave amplitude of i -th wave, and ε_j is random phase angle. The i -th wave amplitude can be calculated as follow:

$$A_j = \sqrt{2S(\omega_j) \Delta\omega} \quad (2.12)$$

where, $\Delta\omega$ is the wave frequency interval. To avoid an increase of wave component, the following modified formula is employed:

$$\eta(x, y, z) = \text{Re} \left[\sum_{j=1}^N A_j e^{i(k_j x \cos \theta + k_j y \sin \theta - \omega'_j t - \varepsilon_j)} \right] \quad (2.13)$$

where, $\omega'_j = \omega_j + \delta\omega_j$ and $\delta\omega_j$ is random a perturbation number and fixed within $-\Delta\omega_j / 2 \leq \delta_j \leq \Delta\omega_j / 2$ to avoid repeatability of simulation in the time domain.

2. Wave Loads on Structures

Since diffraction of wave around the structure is notable for the structure which moves in large displacement in a deep water condition, the appropriate method for diffraction should be employed to predict wave loads on the structure. This section will discuss the diffraction theory and Morrison's equation, which are being used to include inertia and drag forces for the slender member.

2.1 Diffraction and Radiation Theory

Let us consider the boundary value problem for interaction for incident waves. As discussed in the previous section, the velocity potential satisfies the bottom boundary condition, kinematic and dynamic free-surface boundary conditions and Laplace equation. By using the directional normal vector on the body surface, the body boundary condition in the fluid domain can be expressed as follows:

$$\frac{\partial \Phi}{\partial \bar{n}} = V_{\bar{n}} \quad \text{on the body surface} \quad (2.14)$$

where $V_{\bar{n}}$ is the normal vector on the body surface. According to Sommerfeld radiation condition, diffraction and radiation potential can be vanished at far field boundary.

$$\lim_{r \rightarrow \infty} \sqrt{r} \left(\frac{\partial \Phi_{D,R}}{\partial r} \pm ik \Phi_{D,R} \right) = 0 \quad (2.15)$$

where r is the radial distance from the center of structure. Total velocity potential decomposed into incident potential ϕ_I , radiation potential ϕ_R and diffraction potential

ϕ_D . All of these decomposed potentials can be expressed by using the perturbation method as follows:

$$\Phi = \sum_{n=1}^{\infty} \varepsilon^{(n)} \Phi^{(n)} = \sum_{n=1}^{\infty} \varepsilon^{(n)} \left(\Phi_I^{(n)} + \Phi_R^{(n)} + \Phi_D^{(n)} \right) \quad (2.16)$$

The diffraction and radiation wave forces remarkably influence the floating structure in deep water condition. While the diffraction wave is related to the incident wave and presents the scattered term from the fixed body, the radiation wave force is generated and propagated by an oscillating body in calm water.

2.2 First-order Boundary Value Problem (Linear Boundary Value Problem)

In this section, the interaction between incident wave and a freely floating structure will be discussed for first-order accuracy. By separation of variables, the total first-order potential can be re-written as follows:

$$\begin{aligned} \Phi^{(1)} &= \left(\Phi_I^{(1)} + \Phi_R^{(1)} + \Phi_D^{(1)} \right) \\ &= \text{Re} \left\{ \left(\phi_I^{(1)}(x, y, z) + \phi_R^{(1)}(x, y, z) + \phi_D^{(1)}(x, y, z) \right) e^{i(kx \cos \theta + ky \sin \theta - \omega t)} \right\} \end{aligned} \quad (2.17)$$

By referring to the Eq. (2.7), the first-order potential can be re-written as

$$\Phi_I^{(1)} = \text{Re} \left[-\frac{igA \cosh k(z+d)}{\omega \cosh kd} e^{i(kx \cos \theta + ky \sin \theta - \omega t)} \right] \quad (2.18)$$

In order to solve the first-order boundary value problem, following the boundary conditions were employed:

$$\begin{aligned}
\nabla^2 \phi_{D,R}^{(1)} &= 0 && \text{in the fluid } (z \leq 0) \\
\left(-\omega^2 + g \frac{\partial}{\partial z}\right) \phi_{D,R}^{(1)} &= 0 && \text{on the free surface } (z = 0) \\
\frac{\partial \phi_{D,R}^{(1)}}{\partial z} &= 0 && \text{on the bottom } (z = d) \\
\frac{\partial \phi_D^{(1)}}{\partial n} &= \frac{\partial \phi_I^{(1)}}{\partial n} && \text{on the body surface} \\
\frac{\partial \phi_R^{(1)}}{\partial n} &= -i\omega \mathbf{n} \cdot (\boldsymbol{\xi}^{(1)} + \boldsymbol{\alpha}^{(1)} \times \mathbf{r}) && \text{on the body surface} \\
\lim_{r \rightarrow \infty} \sqrt{r} \left(\frac{\partial}{\partial r} \pm ik \right) \phi_{D,R} &= 0 && \text{at far field}
\end{aligned} \tag{2.19}$$

where \mathbf{r} is the position vector on body surface, r is the radian distance from the origin, and \mathbf{n} is the normal vector at the body surface outward direction. The first-order translational motion, $\Xi^{(1)}$, and rotational motion, $\Theta^{(1)}$, can be expressed as follows:

$$\begin{aligned}
\Xi^{(1)} &= \text{Re} \left[\boldsymbol{\xi}^{(1)} e^{-i\omega t} \right] \quad \text{where } \boldsymbol{\xi}^{(1)} = \left[\xi_1^{(1)}, \xi_2^{(1)}, \xi_3^{(1)} \right] \\
\Theta^{(1)} &= \text{Re} \left[\boldsymbol{\theta}^{(1)} e^{-i\omega t} \right] \quad \text{where } \boldsymbol{\theta}^{(1)} = \left[\theta_1^{(1)}, \theta_2^{(1)}, \theta_3^{(1)} \right]
\end{aligned} \tag{2.20}$$

where subscriptions 1, 2, and 3 indicate the x-, y-, and z-axes respectively. In translational motion, 1, 2, and 3 correspond to surge, sway and heave motion, and in rotational motion, 1, 2, and 3 correspond to roll, pitch, and yaw motion. To simplify, it can be expressed with a simplified six degree of freedom equation as follows:

$$\zeta_i^{(1)} = \begin{cases} \xi_j^{(1)} & \text{for } j = 1, 2, 3 \\ \theta_j^{(1)} & \text{for } j = 4, 5, 6 \end{cases} \tag{2.21}$$

The radiation potential can be decomposed into a simplified six-degree-of-freedom mode:

$$\phi_R^{(1)} = \sum_{j=1}^6 \zeta_j^{(1)} \phi_j^{(1)} \quad (2.22)$$

where $\phi_j^{(1)}$ represents the first-order velocity potential of rigid body motion with unit amplitude in the j -th mode when the incident wave does not exist. These velocity potentials should satisfy all of the boundary conditions in Eq. (2.19). Since $\phi_j^{(1)}$ indicates the velocity potential of a rigid body, the body boundary condition, and fifth equation of Eq. (2.19), can be expressed by $\phi_j^{(1)}$.

$$\frac{\partial \phi_j^{(1)}}{\partial n} = \begin{cases} n_j & \text{for } j=1,2,3 \\ (r \times n)_{j-3} & \text{for } j=4,5,6 \end{cases} \text{ on the body surface} \quad (2.23)$$

These boundary conditions are valid on the body surface, and the diffraction potential can be solved in consideration of all the boundary conditions.

2.3 The First-order Hydrodynamic Forces and Moments

The first-order forces, moments, and free-surface elevation can be obtained by solving the first-order potential of diffraction and radiation. By using the perturbation method, the first-order hydrodynamic pressure and free-surface elevation can be described as follows:

$$P^{(1)} = -\rho \frac{\partial \Phi^{(1)}}{\partial t} + gz \quad (2.24)$$

$$\eta^{(1)} = -\frac{1}{g} \frac{\partial \Phi^{(1)}}{\partial t} \quad \text{at } z=0 \quad (2.25)$$

The first-order forces and moments can be obtained by integration over surface pressure on the entire body.

$$\begin{aligned}
F_j^{(1)}(t) &= \iint_{S_B} P \bar{n}_j dS \\
&= -\rho g \iint_{S_B} z \bar{n}_j dS - \rho \operatorname{Re} \left[i\omega \zeta_j e^{-i\omega t} \iint_{S_B} \phi_j \bar{n}_j dS \right] \quad \text{for } j=1 \cdots 6 \quad (2.26) \\
&\quad - \rho \operatorname{Re} \left[i\omega A e^{-i\omega t} \iint_{S_B} (\phi_I + \phi_D) \bar{n}_j dS \right]
\end{aligned}$$

where S_B is the wetted surface of the body when the body is in calm water which satisfies the first-order boundary value problem. The first-order hydrodynamic forces can be decomposed as follows:

$$F^{(1)} = F_{HS}^{(1)} + F_R^{(1)} + F_{EX}^{(1)} \quad (2.27)$$

where, the subscription F_{HS} indicates hydrostatic restoring forces and moments, F_R is the forces and moments which are obtained by the radiation potential, and F_{EX} is the wave exciting forces and moments from the incident and diffraction potential. The hydrostatic restoring forces and moments are defined as the multiplication of the restoring stiffness and the motion responses. The components of restoring stiffness are obtained by integrating the surface of the wetted body.

$$F_{HS}^{(1)} = K \zeta^{(1)} \quad (2.28)$$

where, $\zeta^{(1)}$ is the first-order motion of the body, and K is the hydrostatic restoring stiffness matrix which consists of the following components:

$$\begin{aligned}
K_{33} &= \rho g \iint_{S_B} n_3 dS = \rho g A_w \\
K_{34} &= K_{43} = \rho g \iint_{S_B} y n_3 dS = \rho g A_w y_f \\
K_{35} &= K_{53} = \rho g \iint_{S_B} x n_3 dS = -\rho g A_w x_f \\
K_{44} &= \rho g \iint_{S_B} y^2 n_3 dS + \rho g \nabla_{z_b} - mg z_{cg} \\
K_{45} &= K_{54} = -\rho g \iint_{S_B} x y n_3 dS \\
K_{46} &= K_{64} = -\rho g \nabla_{x_b} + mg x_{cg} \\
K_{55} &= \rho g \iint_{S_B} x^2 n_3 dS + \rho g \nabla_{z_b} - mg z_{cg} \\
K_{56} &= K_{65} = -\rho g \nabla_{y_b} + mg y_{cg}
\end{aligned} \tag{2.29}$$

where, ∇ is the buoyancy force from displacement, A_w is the water plane area, x_f and y_f are the distance from the center of the water plane area to the center of gravity in x-direction and y-direction, respectively, (x_{cg}, y_{cg}, z_{cg}) indicate the center of gravity, and (x_b, y_b, z_b) are the center of buoyancy of the body.

The forces and moments from radiation potential can be obtained by added mass and radiation damping due to first-order motions of the rigid body and can be expressed as follows:

$$F_R^{(1)} = \text{Re} \left([f] [\zeta^{(1)}] \right) \tag{2.30}$$

where,

$$f = f_{ij} = -\rho \iint_{S_B} \frac{\partial \phi_i}{\partial n} \phi_j dS \quad i, j = 1, 2, \dots, 6 \tag{2.31}$$

where, f_{ij} is the complex coefficients which are related to the frequency ω as a result of the free surface conditions. These coefficients consist of real part and imaginary part as follows:

$$f_{ij} = -\omega^2 m_{ij}^a - i\omega C_{ij} \quad (2.32)$$

where, m_{ij}^a is the added mass coefficient and C_{ij} is the radiation damping coefficient.

With two coefficients, Eq. (2.30) can be re-written as follows:

$$F_R^{(1)} = \text{Re} \left[\mathbf{M}^a \cdot \ddot{\zeta}^{(1)} + \mathbf{C} \cdot \dot{\zeta}^{(1)} \right] \quad (2.33)$$

where, \mathbf{M}^a is the added mass coefficient matrix and \mathbf{C} is the radiation damping coefficient matrix. The first-order exciting forces and moments, $F_{EX}^{(1)}$, can be expressed as follows:

$$F_{EX}^{(1)} = \text{Re} \left[-\rho A e^{-i\omega t} \iint_{S_B} (\phi_I + \phi_D) \frac{\partial \phi_j}{\partial n} dS \right] \quad j = 1, 2, \dots, 6 \quad (2.34)$$

According to Eq. (2.34), the first-order exciting forces and moments depend on the frequency and are proportional to incident wave amplitude A . The relationship between incident wave elevation and the first-order diffraction forces on the body can be shown as LTF (Linear Transfer Function) which is the exciting forces from the unit amplitude incident wave. Therefore, the equation of motion can be described as:

$$\begin{aligned} \mathbf{M} \ddot{\zeta}^{(1)} &= F_{HS}^{(1)} + F_R^{(1)} + F_{EX}^{(1)} \\ &= -K \zeta - \left(\mathbf{M}^a \cdot \ddot{\zeta}^{(1)} + \mathbf{C} \cdot \dot{\zeta}^{(1)} \right) + \text{Re} \left[-\rho A e^{-i\omega t} \iint_{S_B} (\phi_I + \phi_D) \frac{\partial \phi_j}{\partial n} dS \right] \quad j = 1, 2, \dots, 6 \end{aligned} \quad (2.35)$$

where, \mathbf{M} is the matrix of body mass which can be defined as:

$$\mathbf{M} = \begin{bmatrix} m & 0 & 0 & 0 & mz_{cg} & -my_{cg} \\ 0 & m & 0 & -mz_{cg} & 0 & mx_{cg} \\ 0 & 0 & m & my_{cg} & -mx_{cg} & 0 \\ 0 & -mz_{cg} & my_{cg} & I_{xx} & I_{xy} & I_{xz} \\ mz_{cg} & 0 & -mx_{cg} & I_{yx} & I_{yy} & I_{yz} \\ -my_{cg} & mz_{cg} & 0 & I_{zx} & I_{zy} & I_{zz} \end{bmatrix} \quad (2.36)$$

where, m is mass of body, and I_{mn} is the moment of inertia which can be obtained by the following equation:

$$I_{mn} = \iiint_V \rho_b (x \cdot x \delta_{mn} - x_m x_n) dV \quad (2.37)$$

where, ρ_b is the density of body and δ_{mn} is the Kronecker delta function from tensor rule.

3. Motion of Floating Structure

The previous section discussed the hydrodynamic forces and moments and the body motion was induced by these hydrodynamic forces and moments. In this section, the formulation of body motion and the solution including numerical integration in both the frequency and time domain will be discussed.

3.1 Wave Loads

Since waves in real situations are random waves, establishing the external wave loads to floating body needs randomly generated wave profiles. In order to make random waves, at least two components, which are linear and second-order wave hydrodynamic

forces, are required. These two wave hydrodynamic forces can be written as two terms of the Volterra series in the time domain.

$$F^{(1)}(t) + F^{(2)}(t) = \int_{-\infty}^{\infty} h_1(\tau) \eta(t-\tau) d\tau + \int_{-\infty}^{\infty} \int_{-\infty}^{\infty} h_2(\tau_1, \tau_2) \eta(t-\tau_1) \eta(t-\tau_2) d\tau_1 d\tau_2 \quad (2.38)$$

where $h_1(\tau)$ is the linear impulse response function, $h_2(\tau_1, \tau_2)$ is the quadratic impulse function at the different unit amplitude inputs at times τ_1 and τ_2 , and $\eta(t)$ is the wave free surface elevation at a reference position. By recalling Eq. (2.11), the wave elevation can be written as a sum of frequency components. Therefore, Eq. (2.38) can be rewritten in the form of summation of N frequency components as follows:

$$\begin{aligned} F_I^{(1)} &= \text{Re} \left[\sum_{j=1}^N A_j L(\omega_j) e^{i\omega_j t} \right] \\ F_I^{(2)} &= \text{Re} \left[\sum_{j=1}^N \sum_{k=1}^N A_j A_k^* D(\omega_j, \omega_k) e^{i(\omega_j - \omega_k)t} \right] + \text{Re} \left[\sum_{j=1}^N \sum_{k=1}^N A_j A_k S(\omega_j, \omega_k) e^{i(\omega_j + \omega_k)t} \right] \end{aligned} \quad (2.39)$$

where $L(\omega_j)$ is a linear transfer function and $D(\omega_j, \omega_k)$ is difference-frequency quadratic transfer function, and $S(\omega_j, \omega_k)$ is the sum-frequency quadratic transfer function. The oscillating body in fluid can generate the propagating waves outward, and these waves continuously influence to fluid pressure. These influenced pressure fields affect the force which is acting on the body. In order to describe this radiation force, the concept of time memory, the retardation function, is employed. The first and second order radiation forces in time domain can be calculated by the following equation:

$$F_R = \left(M^a(\omega) - \int_0^{\infty} R(t) \cos \omega t dt \right) \ddot{\zeta}(t) - \int_{-\infty}^t R(t-\tau) \dot{\zeta}(\tau) d\tau \quad (2.40)$$

where $M^a(\omega)$ is the added mass coefficient at frequency ω , and $R(t)$ is the retardation function for the time memory effect which can be defined as follows:

$$R(t) = \frac{2}{\pi} \int_0^{\infty} C(\omega) \frac{\sin \omega t}{\omega} d\omega \quad (2.41)$$

where $C(\omega)$ is the radiation damping coefficient at frequency ω . The total wave force can be obtained by summation of incident wave forces, Eq.(2.39), and the radiation force, Eq.(2.57).

$$F_T = F^{(1)} + F^{(2)} = F_I^{(1)} + F_I^{(2)} + F_R \quad (2.42)$$

The energy spectrum can easily be obtained by using Fourier transform equations. The energy spectrum of linear, and sum and different frequency forces can be expressed as follows:

$$\begin{aligned} S_F^{(1)}(\omega) &= S_\eta(\omega) |L(\omega)|^2 \\ S_F^{(2)+}(\omega) &= 8 \int_0^{\frac{\omega}{2}} \left| S\left(\frac{\omega}{2} + \mu, \frac{\omega}{2} - \mu\right) \right|^2 S_\eta\left(\frac{\omega}{2} + \mu\right) S_\eta\left(\frac{\omega}{2} - \mu\right) d\mu \\ S_F^{(2)-}(\omega) &= 8 \int_0^{\frac{\omega}{2}} |D(\mu, \omega - \mu)|^2 S_\eta(\mu) S_\eta(\omega - \mu) d\mu \end{aligned} \quad (2.43)$$

where S_η is the wave amplitude spectrum, $S_F^{(1)}$, $S_F^{(2)+}$ and $S_F^{(2)-}$ are the linear wave force spectrum, second order sum and different frequency wave force spectrum, respectively. The viscous damping effects can be considered by using Morrison's formula.

3.2 Morrison's Formula

For the slender cylindrical object, which has a small diameter compared to the wave length, the viscous effect is dominant, while the diffraction effect is neglected. In this case, the added mass effect, inertia effect and the damping effect of the drag force can be evaluated by the Morrison's equation. According to the Morrison's equation, the summation of drag force and inertia force is a total force as follows:

$$F_m = C_m \rho V \dot{u}_n - C_a \rho V \ddot{\zeta}_n + 0.5 \rho C_D D_s (u_n - \dot{\zeta}_n) |u_n - \dot{\zeta}_n| \quad (2.44)$$

where F_m is Morrison's force, $V = \pi D^2 / 4$ is the volume per unit length of the body, D is the diameter of the body, C_m is the inertia coefficient which can be defined as $C_m = 1 + C_a$, D_s is breadth of the body, \dot{u}_n and u_n represent acceleration and velocity of fluid normal to body, respectively, and $\dot{\zeta}_n$ and $\ddot{\zeta}_n$ represent velocity and acceleration of the body. Eq. (2.44) consists of three terms. The first term on the right-hand-side of Eq. (2.44) is the Froude-Krylov force, the second term is added effect, and the last term represents the drag force with respect to relative velocity between body and fluid motion. By adding Morrison's force to the wave forces, the total force on the body can be obtained by:

$$F_T = F_I^{(1)} + F_I^{(2)} + F_R + F_m \quad (2.45)$$

3.3 Solution for Frequency Domain

The equilibrium equation of inertia of body and external forces can be expressed by using momentum conservation known as Newton's second law as follows:

$$\mathbf{M} \frac{d^2 x_{cg}}{dt^2} = \mathbf{f} \quad (2.46)$$

$$\mathbf{I} \frac{d\boldsymbol{\varphi}}{dt} + \boldsymbol{\varphi} \times (\mathbf{I}\boldsymbol{\varphi}) = \mathbf{m} \quad (2.47)$$

where \mathbf{M} is body mass, x_{cg} is center of gravity of body, \mathbf{I} is the moment of inertia, $\boldsymbol{\varphi}$ is the angular velocity, and \mathbf{f} and \mathbf{m} are the external force and moment respectively. The added mass effect part of the second term of Eq. (2.44) and the relative angular motion of the body to the wave motion have a form of non-linearity. In order to consider the angular motion to be linear, the assumption, which is small angular motion, was adopted and then the Eq. (2.47) can be written as follows:

$$\mathbf{M}\ddot{\boldsymbol{\zeta}} = \mathbf{F}(t) \quad (2.48)$$

where $\ddot{\boldsymbol{\zeta}}$ is the normal acceleration of the body motion, and $\mathbf{F}(t)$ is external forces which include hydrostatic, hydrodynamic, and other forces from external condition such as mooring lines, inner cargo tanks, etc. In the frequency domain, Eq. (2.48) can be expanded as:

$$\left[\mathbf{M} + \mathbf{M}^a(\omega) \right] \ddot{\boldsymbol{\zeta}} + \mathbf{C}(\omega) \dot{\boldsymbol{\zeta}} + \mathbf{K}\boldsymbol{\zeta} = \mathbf{F}(\omega) \quad (2.49)$$

where $\mathbf{C}(\omega)$ is the matrix of wave damping, and \mathbf{K} is the matrix of hydrostatic restoring stiffness. For simplification, non-linearity becomes linearity by using the superposition rule. The correspondence of the first-order and second-order wave exciting force can be expressed as:

$$\begin{aligned}\zeta^{(1)}(\omega) &= \mathbf{RAO}(\omega) \cdot \mathbf{F}^{(1)}(\omega) \\ \zeta^{(2)\pm}(\omega^\pm) &= \mathbf{RAO}(\omega^\pm) \cdot \mathbf{F}^{(2)\pm}(\omega^\pm)\end{aligned}\tag{2.50}$$

where RAO (Response Amplitude Operator) is an engineering statistic, this can be obtained by:

$$\mathbf{RAO}(\omega) = \frac{1}{\left[-\omega^2 \{ \mathbf{M} + \mathbf{M}^a(\omega) \} - i\omega\mathbf{C}(\omega) + \mathbf{K} \right]}\tag{2.51}$$

When the RAO is obtained, we can get the response of the body in random waves using linear spectrum analysis as follows:

$$\mathbf{S}_\zeta(\omega) = |\mathbf{RAO}(\omega)|^2 \left[\mathbf{S}_F^{(1)}(\omega) + \mathbf{S}_F^{(2)\pm}(\omega) \right]\tag{2.52}$$

where $\mathbf{S}_\zeta(\omega)$ is the spectrum of body motion, $\mathbf{S}_F^{(1)}(\omega)$ is the first-order wave force spectrum, and $\mathbf{S}_F^{(2)\pm}(\omega)$ is the second-order sum and difference wave force at frequency ω , respectively.

3.4 Solution of Time Domain

The body motion calculation in the frequency domain is straightforward and simple by using a method to turn non-linearity to linearity. Despite the frequency domain analysis potentially having an error caused by the linearized drag force this is a more efficient method than the time domain analysis and is the acceptable practical range. In this case of moored floating, however, it is very important not to neglect the non-linearity effect. Therefore, the advanced time domain analysis including non-linearity should be employed in the mooring body case with the riser system. Using a

non-linear term such as second-order term, the equation of motion in the time domain can be expressed as follows:

$$\left[\mathbf{M} + \mathbf{M}^a(\infty) \right] \ddot{\zeta} + \mathbf{K}\zeta = \mathbf{F}_I(t) + \mathbf{F}_C(t, \dot{\zeta}) + \mathbf{F}_N(t, \dot{\zeta}) \quad (2.53)$$

where $\mathbf{M}^a(\infty)$ is added mass at frequency ∞ obtained by:

$$\mathbf{M}^a(\infty) = \mathbf{M}^a(\omega) - \int_0^\infty R(t) \cos \omega t dt \quad (2.54)$$

$\mathbf{F}_I(t)$ in the Eq. (2.53) is wave exciting forces on the structure for first and second order, $\mathbf{F}_C(t, \dot{\zeta})$ is radiation damping force, and $\mathbf{F}_N(t, \dot{\zeta})$ is the non-linear drag force which can be obtained by Morrison's equation. $\mathbf{F}_C(t, \dot{\zeta})$ can be defined as:

$$\mathbf{F}_C(t, \dot{\zeta}) = \int_{-\infty}^t R(t-\tau) \dot{\zeta} d\tau \quad (2.55)$$

where $R(t)$ is the retardation function. In order to solve non-linearity, many numerical schemes of iterative procedure in the time domain are suggested. In this study, the Adams-Moulton scheme is employed for taking second order accuracy with a fast calculation. Furthermore, the Adams-Bashforth scheme is also employed for the non-linear force integration for time. The scheme, Adams-Moulton can be written as follows:

$$\int_{t^{(n)}}^{t^{(n+1)}} x dt = \frac{\Delta t}{2} \left[x^{(n)} + x^{(n+1)} \right] \quad (2.56)$$

In the first step, the equation of motion is separated into two first order differential equations as follows:

$$\bar{\mathbf{M}} \dot{\zeta} = \mathbf{F}_I(t) + \mathbf{F}_C(t, \dot{\zeta}) + \mathbf{F}_N(t, \dot{\zeta}) - \mathbf{K}\zeta \quad (2.57)$$

$$\dot{\zeta} = \xi \quad (2.58)$$

Where the virtual matrix, $\bar{\mathbf{M}}$, can be obtained as follow:

$$\bar{\mathbf{M}} = \mathbf{M} + \mathbf{M}^a(\infty) \quad (2.59)$$

Next, integrating each equation for time step from $t^{(n)}$ to $t^{(n+1)}$, we can then obtain the followings:

$$\bar{\mathbf{M}}\dot{\xi}^{(n+1)} = \bar{\mathbf{M}}\dot{\xi}^{(n)} + \int_{t^{(n)}}^{t^{(n+1)}} (\mathbf{F}_I + \mathbf{F}_C + \mathbf{F}_N) dt + \int_{t^{(n)}}^{t^{(n+1)}} -\mathbf{K}\zeta dt \quad (2.60)$$

$$\zeta^{(n+1)} = \zeta^{(n)} + \int_{t^{(n)}}^{t^{(n+1)}} \xi dt \quad (2.61)$$

By applying the Adams-Moulton scheme, Eqs. (2.56), (2.60) and (2.61) can be rewritten as follows:

$$\bar{\mathbf{M}}\xi^{(n+1)} = \bar{\mathbf{M}}\xi^{(n)} + \frac{\Delta t}{2} (\mathbf{F}_I^{(n+1)} + \mathbf{F}_I^{(n)} + \mathbf{F}_C^{(n+1)} + \mathbf{F}_C^{(n)} + \mathbf{F}_N^{(n+1)} + \mathbf{F}_N^{(n)}) - \frac{\Delta t}{2} \mathbf{K} (\zeta^{(n+1)} + \zeta^{(n)}) \quad (2.62)$$

$$\xi^{(n+1)} = \frac{2}{\Delta t} (\zeta^{(n+1)} + \zeta^{(n)}) - \xi^{(n)} \quad (2.63)$$

Eqs. (2.79) and (2.80) are the combination of two algebraic equations with unknown quantities $\xi^{(n+1)}$ and $\zeta^{(n+1)}$. In Eq. (2.62), the convolution terms $\mathbf{F}_C^{(n+1)}$ and $\mathbf{F}_N^{(n+1)}$ are unknown variables at time $t^{(n+1)}$. In this procedure, the time integration may have an error due to the arbitrary adoption of the convolution terms. In order to avoid this error, the Adams-Bashforth scheme is employed for non-linear force terms as follows:

$$\int_{t^{(n)}}^{t^{(n+1)}} \mathbf{F}_{C,N} dt = \begin{cases} \Delta t \mathbf{F}_{C,N}^{(0)} & \text{for } n = 0 \\ \frac{\Delta t}{2} (3\mathbf{F}_{C,N}^{(n)} - \mathbf{F}_{C,N}^{(n-1)}) & \text{otherwise} \end{cases} \quad (2.64)$$

Eventually, Eqs. (2.57) and (2.58) can be rewritten as:

$$\left[\frac{4}{\Delta t} \bar{\mathbf{M}} + \mathbf{K} \right] \Delta \zeta = \frac{4}{\Delta t} \bar{\mathbf{M}} \xi^{(n)} + \left(\mathbf{F}_I^{(n+1)} + \mathbf{F}_I^{(n)} \right) + \left(3\mathbf{F}_C^{(n)} + \mathbf{F}_C^{(n-1)} \right) + \left(3\mathbf{F}_N^{(n)} + \mathbf{F}_N^{(n-1)} \right) - 2\mathbf{K} \zeta^{(n)} + 2\mathbf{F}_0 \quad (2.65)$$

$$\Delta \zeta = \zeta^{(n+1)} - \zeta^{(n)} \quad (2.66)$$

where \mathbf{F}_0 is the net buoyancy force for balancing a system which is constant. First, the unknown variable, $\Delta \zeta$, is calculated from Eq. (2.65), and then other unknown variables, $\xi^{(n+1)}$ and $\zeta^{(n+1)}$, can be obtained from Eqs. (2.63) and (2.67), the Adams-Bashforth scheme can avoid the iterative procedure, however; it can cause numerical instability if the time interval is not small enough. The proper time interval, which is large enough to achieve fast simulation but not produce an error due to a too large time interval, can be selected from the numerical test or criterion such as Courant number.

CHAPTER III

MOVING PARTICLE SIMULATION FOR SINGLE-LIQUID

MPS, which is a fully Lagrangian approach CFD (Computational Fluid Dynamics), uses particle interaction models corresponding to differential operators to discretize governing equations for continuum. In general CFD, the Eulerian approach is used to solve governing equations due to its easy applicability and fast calculation; however, as computer performance increases, it is possible to simulate with Lagrangian approach. Since the Eulerian approach system is using a control volume called grid, it has difficulty in generating complicated shapes and applying boundary conditions to the grid. Another issue is the governing equations. In the Lagrangian approach, the convection term can be calculated directly; therefore the mass conservation law can easily be satisfied.

1. Governing Equation

The governing equations for the incompressible viscous fluid consist of the continuity equation and the Navier-Stoke's equation as follows:

$$\frac{D\rho}{Dt} = 0 \quad (3.1)$$

$$\frac{D\vec{u}}{Dt} = -\frac{1}{\rho}\nabla p + \nu\nabla^2\vec{u} + \vec{F} \quad (3.2)$$

where ρ is density, \vec{u} is velocity, p is pressure, ν is kinematic viscosity, ∇ is gradient, and \vec{F} is external force.

In the general CFD with grid, the continuity equation is written with respect to velocity divergence; however, in the MPS, the continuity equation Eq. (3.1) is written with respect to density due to the Lagrangian approach. The left hand side of Navier-stoke's equation denotes the Lagrangian differentiation including convection terms. Since the convection term is included in the total differentiation term, it is directly calculated by particle moving. With direct calculation of the convection term, numerical error can be reduced. The right hand side of Navier stoke's equation consists of the pressure gradient, viscous, and external force terms. In order to simulate the incompressible viscous flows, all terms of differential operators should be replaced with the particle interaction models.

2. Kernel Function

Discretization of differential operators without grid should be considered in the MPS system. Gradient, diffusion and Laplacian exist in the MPS and those terms are

discretized by corresponding particle interaction models. Those models are based on the kernel function which is same meaning of effect from neighboring particle with respect to distance from the center particle. Kernel function can have the same concept as the scheme of grid method. In the MPS, the weight of particle interaction can be expressed by the kernel function. In this study, the following kernel function is employed:

$$w(r) = \begin{cases} \left(1 - \frac{r}{r_e}\right)^3 \left(1 + \frac{r}{r_e}\right)^3 & (0 \leq r < r_e) \\ 0 & (r_e < r) \end{cases} \quad (3.3)$$

where r is distance between particles, and r_e represents the effective range of particle interactions. If particle distance, r , exceeds the effective range, r_e , the kernel function become zero as shown in Fig. 1b.

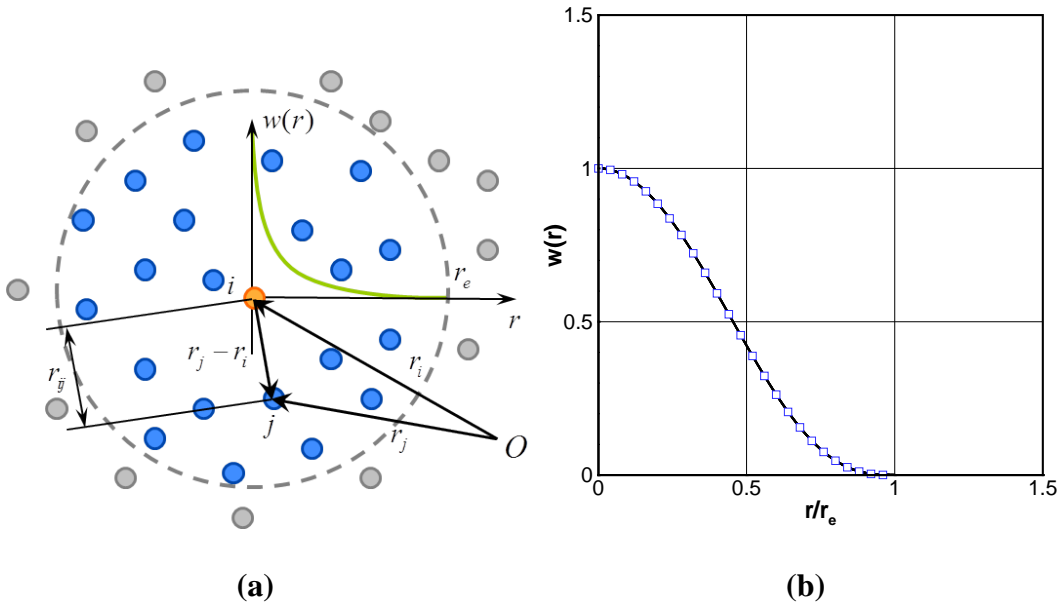


Figure 1 Schematic concept of kernel function (a) and (b) plot of kernel function

By using summation of kernel function for particle i , the particle number density, which corresponds to the density of fluid, can be calculated by the following equation:

$$n_i = \sum_{j \neq i} w(|r_j - r_i|) \quad (3.4)$$

where subscription i denotes centered particle, subscription j denotes neighboring particle, r_i and r_j represent position vector.

Let us assume that if the density of each particle is constant, the particle number density is proportional to the density of fluid. Assuming that N particles exist in volume \bar{V} with mass m , density ρ can be:

$$\rho = \frac{mN}{\bar{V}} \quad (3.5)$$

The volume can be expressed by integration within range Ω , and the number of particles can be expressed by the particle number density. For expressing the number of particles by the particle number density, another kernel function, which is same as delta function is required. Another kernel function has value one in the effective range Ω , otherwise the value is zero.

$$\rho(r) = \frac{m \sum_j w'(|r_j - r_i|)}{\int_{\Omega} w' dv} \quad (3.6)$$

$$w'(r) = \begin{cases} 1 & (0 \leq r < r_e) \\ 0 & \text{otherwise} \end{cases} \quad (3.7)$$

Density from Eq. (3.6) can be calculated by $w'(r)$. In the MPS, $w'(r)$ can be replaced by kernel function $w(r)$. Substituting $w(r)$ into Eq. (3.6), density can be expressed as follows:

$$\rho(r) = \frac{m \sum_j w(|r_j - r_i|)}{\int_{\Omega} w dv} \quad (3.8)$$

In the MPS, particles cannot coincide to satisfy the mass conservation law. Therefore, the centered particle, i , does not count for density calculation and other particle interaction models. Eq. (3.8) can be rewritten with respect to the kernel function as follows:

$$\sum_{j \neq i} w(|r_j - r_i|) = \frac{\rho(r) \int_{\Omega'} w dv}{m} = n_i \quad (3.9)$$

where Ω' is area without a portion of i -th particle. From Eq. (3.9), it is shown that particle number density is proportional to density of fluid if mass of particle is constant.

Since it is incompressible flow, density should be constant, thus the particle number density also should be same as particle number density at the initial arrangement. Hereafter, the particle number density at initial arrangement is set as n^0 .

3. Gradient Model

Let us consider two particles, which are centered particle i and neighboring particle j within the effective range, each particle has position vector \vec{r}_i and \vec{r}_j and

scalar value ϕ_i and ϕ_j shown in Fig. 2. The scalar value ϕ_j can be expressed by Taylor expansion with respect to ϕ_i as follows:

$$\phi_j = \phi_i + \nabla \phi|_i \cdot (\vec{r}_j - \vec{r}_i) + \dots \quad (3.10)$$

To simplify, let us consider only the first order term, and then

$$\nabla \phi|_i \cdot (\vec{r}_j - \vec{r}_i) = \phi_j - \phi_i \quad (3.11)$$

According to the manner of Taylor expansion, there is only position value of i particle; however, in the initial arrangement of particles, it is symmetric between particle i and j . Therefore, we can consider its value is between particles i and j , and then we can get following equation:

$$\nabla \phi|_{ij} \cdot (\vec{r}_j - \vec{r}_i) = \phi_j - \phi_i \quad (3.12)$$

Dividing by absolute value of $(|\vec{r}_j - \vec{r}_i|)$, the differential equation of the left hand side of Eq. (3.12) can be obtained.

$$\nabla \phi|_{ij} \cdot \frac{(\vec{r}_j - \vec{r}_i)}{|\vec{r}_j - \vec{r}_i|} = \frac{\phi_j - \phi_i}{|\vec{r}_j - \vec{r}_i|} \quad (3.13)$$

Multiplying unit vector to $(\vec{r}_j - \vec{r}_i)$ direction, and then Eq. (3.13) becomes the gradient model between particles i and j .

$$\langle \nabla \phi \rangle_{ij} = \left[\nabla \phi|_{ij} \cdot \frac{(\vec{r}_j - \vec{r}_i)}{|\vec{r}_j - \vec{r}_i|} \right] \frac{(\vec{r}_j - \vec{r}_i)}{|\vec{r}_j - \vec{r}_i|} = \frac{(\phi_j - \phi_i)(\vec{r}_j - \vec{r}_i)}{|\vec{r}_j - \vec{r}_i|^2} \quad (3.14)$$

The symbol $\langle \rangle$ represents the particle interaction model. The gradient is a vector operator with scalar variables. If the scalar value of two points are known, the gradient

vector can be obtained by Eq. (3.14). However, this gradient vector does not include vertical information since it shows only the vector direction of relative position. For example, it has an indistinct gradient to measure the slope with scalar values of two points. Even if there is a steep slope between two particles, the two particles, which are arranged vertically, have zero gradients. In order to resolve the error of the gradient equation, it is modified with the kernel function to be suitable to the MPS system as follows:

$$\langle \nabla \phi \rangle_i = \frac{d}{n^0} \sum_{j \neq i} \left[\frac{(\phi_j - \phi_i)}{|\vec{r}_j - \vec{r}_i|^2} (\vec{r}_j - \vec{r}_i) w(|\vec{r}_j - \vec{r}_i|) \right] \quad (3.15)$$

where d is the number of dimension. For 2-dimensional simulation, it is two and three for 3-dimensional simulation. The aforementioned gradient model does not include vertical position information, thus, by multiplying number of dimension, existence of neighboring particles can be uniform.

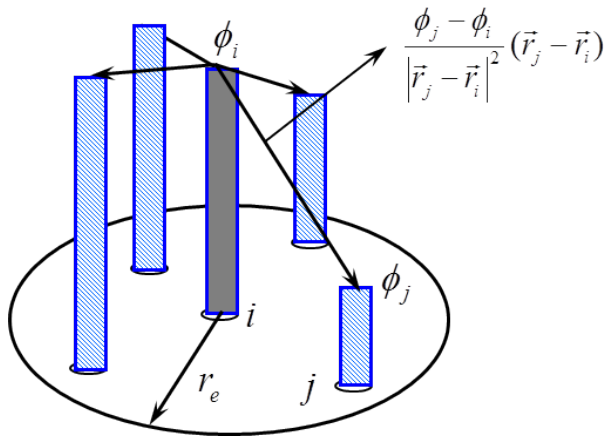


Figure 2 Schematic concept of gradient model

4. Divergence Model

By using divergence, scalar quantities can be obtained from vector components. It can maintain the position vectors and vector components of centered and neighboring particles. The 2-dimensional divergence equation can be expressed as follows:

$$\nabla \cdot \vec{u} = \frac{\partial u}{\partial x} + \frac{\partial v}{\partial y} \quad (3.16)$$

The respective position vector for axis x' , which is between particles i and j , can be differentiated as follows:

$$\frac{\partial \vec{u}}{\partial x'} = \frac{\vec{u}_j - \vec{u}_i}{|\vec{r}_j - \vec{r}_i|} \quad (3.17)$$

Only component x' is required for differentiation, so Eq.(3.17) can be modified as follows:

$$\frac{\partial u_{x'}}{\partial x'} = \frac{(\vec{u}_j - \vec{u}_i) \cdot (\vec{r}_j - \vec{r}_i)}{|\vec{r}_j - \vec{r}_i| |\vec{r}_j - \vec{r}_i|} \quad (3.18)$$

In the same manner as the gradient model, Eq. (3.18) can be transformed into the MPS model the including number of dimension and kernel function.

$$\langle \nabla \cdot \vec{u} \rangle_i = \frac{d}{n^0} \sum_{j \neq i} \frac{(\vec{u}_j - \vec{u}_i) \cdot (\vec{r}_j - \vec{r}_i)}{|\vec{r}_j - \vec{r}_i|^2} w(|\vec{r}_j - \vec{r}_i|) \quad (3.19)$$

5. Laplacian Model

In the MPS, the Laplacian model can be regarded as diffusion in physics. The schematic model of Laplacian is shown in Fig. 3. The diffusion can be modeled by

distribution of the physical quantities from a center particle to neighboring particles using the kernel function. Moreover, a parameter λ can be used to increase quantities to be equal to the analytical solution. The Laplacian model and the λ can be described as follows:

$$\langle \nabla^2 \cdot \phi \rangle_i = \frac{2d}{\lambda n^0} \sum_{j \neq i} [(\phi_j - \phi_i) w(|\vec{r}_j - \vec{r}_i|)] \quad (3.20)$$

$$\lambda = \frac{\sum_{j \neq i} |\vec{r}_j - \vec{r}_i|^2 w(|\vec{r}_j - \vec{r}_i|)}{\sum_{j \neq i} w(|\vec{r}_j - \vec{r}_i|)} \quad (3.21)$$

Since the quantities lost by particle i are only obtained by neighboring particle j , the conservation law can be satisfied.

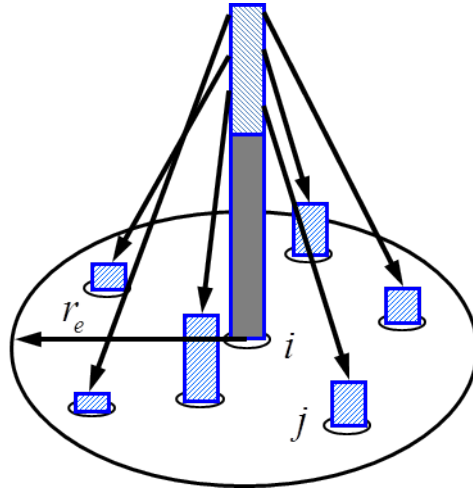


Figure 3 Example of Laplacian model

6. Incompressibility Model

In the MPS, the particle number density can be regarded as density of fluid. Therefore, the continuity equation should be fulfilled with the particle number density instead of density of fluid. As consequence, the particle number density at initial particle arrangement is regarded as constant and used through the entire cycle of simulation. Another restriction is that the particle number density at every end of the simulation cycle should be the same as the particle number density in the initial stage since particle number density is regarded as density of fluid.

The algorithm of the incompressibility model of MPS is similar to the SMAC (Simplified Marker-and-Cell) method in the grid-based CFD. The incompressibility model consists of two stages. The first stage is the explicit stage. In the explicit stage, diffusion and external forces are calculated explicitly with the quantities at time n to obtain the temporal components of velocity and position of particle i . The temporal velocity, thus, can be expressed as follows:

$$\vec{u}_i^* = \vec{u}_i^n + \Delta t \left[\nu \nabla^2 \vec{u}_i^n + g \right] \quad (3.22)$$

From the temporal velocity, the temporal position of particle i can be obtained as:

$$\vec{r}_i^* = \vec{r}_i^n + \Delta t \vec{u}_i^* \quad (3.23)$$

In Eq. (3.23), the convection term can be calculated directly by moving particles according to the temporal velocity component. After the explicit stage, the particle number density is also updated due to the particle movement.

Due to the mass conservation law, the density must be conserved in the entire simulation; however, the updated particle arrangement with temporal position can

change the particle number density since the particle number density can be different from the initial particle number density. In the implicit stage, the particle number density will be adjusted to be equal to n^0 .

$$n^0 = n^{n+1} = n^* + n' \quad (3.24)$$

$$\vec{u}^{n+1} = \vec{u}^* + \vec{u}' \quad (3.25)$$

$$\vec{r}^{n+1} = \vec{r}^* + \Delta t \vec{u}' \quad (3.26)$$

where n' is the particle number density corrector and \vec{u}' is the velocity corrector. The velocity corrector can be obtained by the implicit pressure gradient which follows:

$$\vec{u}' = -\frac{\Delta t}{\rho_0} \nabla p^{n+1} \quad (3.27)$$

The velocity corrector and the particle number density corrector can be expressed by the mass conservation law

$$\frac{D\rho}{Dt} + \rho \nabla \cdot \vec{u} = 0 \quad (3.28)$$

Substituting constant density, which is the density at the initial arrangement, into Eq. (3.28) and then

$$\frac{D\rho}{Dt} + \rho_0 \nabla \cdot \vec{u} = 0 \quad (3.29)$$

Since density of fluid is proportional to particle number density, Eq. (3.29) can be rewritten as

$$\frac{1}{n^0} \frac{Dn}{Dt} + \nabla \cdot \vec{u} = 0 \quad (3.30)$$

In this procedure, the particle number density corrector can be produced by the velocity corrector. Discretizing it in the same time Eq. (3.30) can be modified as follows:

$$\frac{n'}{n^0 \Delta t} + \nabla \cdot \vec{u} = 0 \quad (3.31)$$

By Taking the divergence to Eq. (3.27) and then substituting it into Eq. (3.31), the Poisson equation can be obtained.

$$\nabla^2 p^{n+1} = -\frac{\rho_0}{\Delta t^2} \frac{n^* - n^0}{n^0} \quad (3.32)$$

The right hand side of Eq. (3.32) is the source of the Poisson equation. However, this source term can produce exaggerated fluctuated behavior of the pressure in both space and time. Tanaka et al (2008) suggested a mixed source term for MPS; it then improved by Lee et al (2010). In the Grid-based CFD, the source of the Poisson equation is given by the divergence-free condition. If MPS uses the same source term as the grid-based CFD, the fluctuation of pressure can be suppressed; however, it may contain errors as time passes. Mixed source terms can reduce the fluctuation of pressure and also avoid errors. The most important part of this concept is the ratio of each term. The ratio γ can be obtained from numerical test. The pressure laplacian at time $n+1$ can be expressed as follows:

$$\nabla^2 p^{n+1} = -\gamma \frac{\rho_0}{\Delta t^2} \frac{n^* - n^0}{n^0} - (1-\gamma) \frac{\rho_0}{\Delta t} \nabla \vec{u}^* \quad (3.33)$$

7. Boundary Condition

MPS also needs several boundary conditions for simulation the same as for the grid-based CFD. The number of conditions and the type of conditions can be changed depending on what the case is considering. For example, for pipe flow analysis, inlet and outlet boundary conditions, which connect outlet and inlet, should exist for a long time simulation. Except for these case dependent conditions, there are two major boundary conditions for MPS. The following sections will discuss these boundary conditions.

7.1 Free-surface Boundary Condition

As free-surface boundary conditions, kinematic and dynamic boundary conditions are imposed. Since particles are moving on the free-surface, the kinematic boundary condition, which is the component of fluid velocity normal to the boundary and must be zero, can be satisfied directly. Tanaka et al (2008) suggested a method for tracking free-surface particles which is straightforward since it is to obtain the location of free-surface particles with a fully Lagrangian treatment.

In the vicinity of the free-surface, the particle number density should be decreased since the air region is empty without particles in the case of a single-phase problem. Thus, the particles satisfying the following conditions are regarded as free-surface particles:

$$\langle n \rangle_i^* < \beta_1 n^0 \quad (3.34)$$

$$N_i < \beta_2 N^0 \quad (3.35)$$

with

$$\langle n \rangle_i^* = \sum_{j \neq i} w(|\vec{r}_j - \vec{r}_i|) \quad (3.36)$$

$$N_i = \sum_{j \neq i} w_n(|\vec{r}_j - \vec{r}_i|) \quad (3.37)$$

$$w(r) = \begin{cases} \left(1 - \frac{r}{r_e}\right)^3 \left(1 + \frac{r}{r_e}\right)^3 & (0 \leq r < r_e) \\ 0 & (r_e < r) \end{cases} \quad (3.38)$$

$$w_n = \begin{cases} 1 & (0 \leq r \leq r_e) \\ 0 & (r > r_e) \end{cases} \quad (3.39)$$

where N is the number of particles within an effective range except center particle, N^0 is N at the initial arrangement, β_1 and β_2 are free-surface parameters which are below 1.0, and 0.97 and 0.85 is selected in this study, respectively. The free-surface boundary condition can enable the MPS system to simulate fragmentation and coalescence of fluid.

After selection of free-surface particles, the dynamic free-surface boundary condition should be considered. According to the dynamic free-surface boundary condition, the pressure of free-surface particles should be the same as the atmosphere pressure ($p_{free-surface} = p_{atmosphere} = 0$). The dynamic free-surface boundary condition is accomplished in the procedure for solving the Poisson equation for pressure.

7.2 Wall Boundary Condition

As aforementioned, the particle number density is regarded as the density of fluid, thus the continuity equation expressed by particle number density should be satisfied. In order to satisfy the continuity equation, wall particles are set along the solid boundary

and the dummy particles are located inside the solid wall since particle number density is calculated by neighboring particles.

In the particle method, physical quantities are calculated through interaction between center and neighboring particles, so it is important to obtain useful information from neighboring particles. However, if we consider the simple liquid tank, liquid particles are inside the wall particles. In this situation, wall particles directly contact fluid particles, but the outside region can be vacant. As a result, the particle number density of wall particles and fluid particles near the wall cannot satisfy the continuity equation. In order to solve this problem, the concept of a dummy cell is employed. A dummy particle does not contribute to the pressure calculation; it is used only to satisfy the particle number density. The wall particles are involved in the pressure calculation to avoid concentration of particles near the wall.

In this study, the no-slip wall boundary condition is implemented. Wall particles are involved in the pressure calculation; however, their velocity is set at zero to satisfy the no-slip condition. For the dummy particles, the same manner is used as grid method to treat the dummy cell. As a result, the dummy particle has exactly the opposite value of the fluid particle across the wall particle.

8. Collision Model

The repulsive force induced by local pressure can be calculated. However, since free-surface particles have fixed pressure from the atmosphere pressure, the repulsive force may not be generated properly when particles get close. In particular, when

particles accelerating from the outside collide with a free-surface such as a breaking wave, the particle number density can be suddenly increased. Due to increased particle number density, some free-surface particles lose their phenomenon. As a result, pressure can be increased suddenly, which must be zero according to the dynamics free-surface boundary condition. Faulty calculated pressure can reduce the spatial stability of the pressure. In order to avoid this, a collision model is employed to calculate the proper repulsive force especially near the free-surface region.

In the initial stage, the initial particle distance can be obtained. Since particles are arranged uniformly in the initial stage, the initial particle distance is the same for the entire particle domain. It is important to distinguish the initial particle distance is to activate the collision model to particle. When the distances between the arbitrary two particles are less than al_0 , the collision model can be applied. After distinction, from the conservation of momentum, the repulsive velocity can be calculated by using coefficient b related to repulsiveness. Here, a and b are arbitrary value and which can be selected by numerical test. In this study, a and b are set at 0.97 and 0.2, respectively. The collision model is applied not only free surface particle, but also fluid particle and wall particle.

9. Hydrostatic Correction Model

In science, the free-surface layer is a very thin layer which cannot be easily measured. According to dynamic free surface boundary condition, only this thin layer has atmosphere pressure ($p_{atm} = 0$). If MPS commits to generate this very thin layer, the

number of particles in use is astronomical and will exceed computer performance. As a result, MPS assumes that one particle can be regarded as a free surface. Although MPS cannot generate a very thin layer, the size of particle is acceptable in an engineering sense. However, in a strict way, the particle, which has atmosphere pressure, can underestimate hydrostatic pressure in the entire system. Another issue for free-surface is that it lays under one particle length than its design. For example, if water depth is selected as 0.3m and the initial particle distance is 0.005m, then the free-surface lays at 0.295m. The reason why water depth would be 0.3 plus 0.005m is that free-surface particle does not have pressure, but has gravitational velocity from the explicit stage. Therefore, applying particle weight to the free-surface can resolve this error.

In order to apply weight to a free-surface particle, it is necessary to determine how this free-surface can affect hydrostatic pressure. Moreover, according to Fig. 4, the free surface is located one particle size lower when compared to the real system. The abstruse problem is that if we do not have a free surface as the previous MPS system, it may violate the dynamic free surface boundary condition and the entire system can generate an error. In order to fix this problem, I suggest a correction to the hydrostatic pressure. After calculation of pressure from the Poisson Pressure Equation and before the pressure gradient calculation, which can obtain the particle velocity from the pressure gradient, we apply the weight of free surface particle to avoid underestimation and falsely indicating the free-surface layer.

In this model, it is important to select free surface particle when hydrostatic pressure correction is required. When a particle comes out from the fluid group such as

splash, it may not need the hydrostatic correction model. Thus, the concept of an interface searching model is employed to indicate the free surface particle which require hydrostatic pressure correction model.

$$\beta_3 n_0 < n_i < \beta_1 n_0 \text{ if only particle "i" is free surface particle} \quad (3.40)$$

$$N_i < \beta_2 N_0 \quad (3.41)$$

With this additional option with β_3 , the free surface particle which is needed to fix the hydrostatic pressure can be determined. Eq. (3.42) expresses the hydrostatic correction model, and is applied to the HSC required free surface particle which is shown in Fig. 5.

$$P_{i,HSC} = 0.5 \rho_i l_o g \quad (3.42)$$

where $P_{i,HSC}$ denotes the pressure of the HSC required free surface particle, V_i represents the volume of particle.

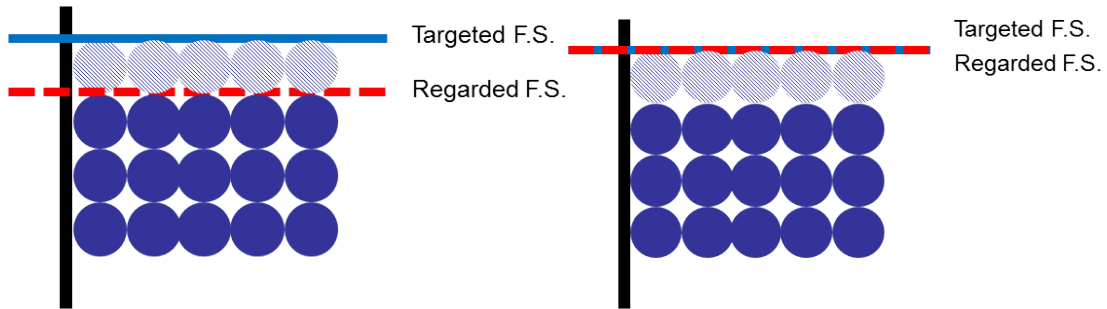


Figure 4 The free surface layer (a) without and (b) with hydrostatic correction

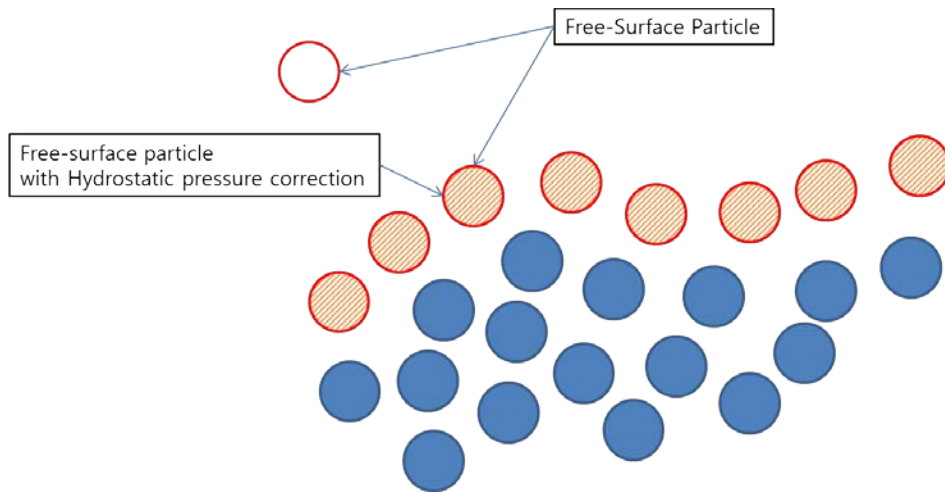


Figure 5 Example for identification of HSC particles

CHAPTER IV

MOVING PARTICLE SIMULATION FOR MULTI-LIQUID

The previous chapter discussed the MPS system. The aforementioned system can be suitable for violent behavior of fluid in severe conditions such as sloshing tank and broken dam. By comparison with the experiment results, the MPS system can be validated. Although it has a free-surface, it is not strictly two-phase flow due to empty space for air portion. In order to extend MPS system to multi-liquid, several points should be discussed such as boundary conditions at interface, self-buoyancy force due to surrounded fluid and surface tension. This chapter will discuss special treatments for multi-liquid system.

1. Interface Searching Model

Interface is a very thin layer within different fluids due to sudden changes in physical phenomenon. The free-surface, for example, is the interface between fluid and air. The free-surface searching model is already established in the original single-liquid MPS. However, in the present MPS system, air particles do not exist due to too great sudden density change which may blow out the program. Thus, the free-surface particle searching method uses only one fluid phenomenon when it judges which is or is not free-surface particle. Therefore, it cannot be implemented directly to the interface searching model.

In order to perform the interface interaction model, finding the interface particle with the proper method should be prerequisite. The interface searching model also uses particle number density the same as the free surface searching model. For free surface searching, the air part is assumed to be a vacuum, so there is no particle in the air portion. It might be problematic if the interface searching model follows the free surface searching model because near the interface particle is not a vacant area such as an air part. In order to avoid the above-mentioned problem, several new criteria for the interface searching model are required.

The new criterion for interface is minimum particle number density with the same particle definition as the center particle. According to the first free surface particle condition, $n_i < \beta_1 n^0$, the particle number density of i particle is less than β_1 times the particle number density at initial arrangement. With this criterion, the free surface particle is well searched. It is assumed that if only one fluid particle is in the middle of other particles, it can also be regarded as an interface particle although it is not the actual interface particle. According to the definition of interface, one single particle cannot generate a layer, thus it cannot generate an interface. Adding one more condition, minimum particle number density, can resolve this error. If the particle number density with the same fluid is not over $\beta_4 n^0$, it is not interface particle even though the center particle has less particle number density. The interface searching model with minimum particle number density can be expressed as follows:

$$\beta_4 n^0 < \langle n \rangle_{i,\xi} < \beta_5 n^0 \quad (4.1)$$

$$N_{i,\xi} < \beta_6 N_0 \quad (4.2)$$

where $\langle n \rangle_{i,\xi}$ is particle number density of the same fluid as the center particle, and $N_{i,\xi}$ is the number of particles of the same fluid as the center particle within an effective range. The second subscription indicates phase or kind of fluid. The particle number density and number of particles for interface searching can be obtained by the following equations:

$$\langle n \rangle_{i,\xi} = \sum_{j \neq i}^N w_n (|r_{j,\xi} - r_{i,\xi}|) \quad (4.3)$$

$$N_{i,\xi} = \sum_{j \neq i}^{N_\xi} w_n (|r_{j,\xi} - r_{i,\xi}|) \quad (4.4)$$

The difference between the free-surface searching model and the interface searching model is the existence of minimum condition with β_4 . Since the interface is a very thin layer between different phases, a small group or just one particle cannot generate an interface. According to Eq. (4.1), the sign of inequality states that particle number density should be over the particle number density at initial arrangement multiply by the parameter β_4 . In the present study, β_4 , β_5 , and β_6 are set to 0.4, 0.97, and 0.85, respectively. These numbers are obtained through numerical tests.

2. Boundary Conditions at Interface

As interface boundary conditions, the kinematic and the dynamic boundary conditions are imposed the same as the free-surface boundary conditions. The kinematic boundary condition is directly satisfied by the tracing particle on the interface.

Since the Lagrangian approach can easily obtain the location of interface particles, the tracking interface particle is quite straightforward, which has already been discussed in a previous chapter. On the other hand, the dynamic boundary condition is satisfied by taking the same pressure opposite the interface. In this study, we assume that there is an imaginary interface particle, which has an averaged position and pressure of interface particles with the same density. The physical phenomenon can be defined by the following equations:

$$P_{IMG} = \frac{\sum_{j \neq i}^{N_{\eta, interface}} P_{j, \eta, interface}}{N_{\eta, interface}} \quad (4.5)$$

$$x_{IMG} = \frac{\sum_{j \neq i}^{N_{\eta, interface}} x_{j, \eta, interface}}{N_{\eta, interface}} \quad (4.6)$$

$$z_{IMG} = \frac{\sum_{j \neq i}^{N_{\eta, interface}} z_{j, \eta, interface}}{N_{\eta, interface}} \quad (4.7)$$

where p is pressure acts on particle, x and z are positions of particle, N denotes number of neighboring particles, the subscription IMG represents imaginary particle, η denotes the phase of particle, and *interface* indicates interface particle. The neighboring particles should interface within the effective range when center particle i is the only interface particle and different fluid to neighboring particles. This imaginary interface particle can be reference particle for heavier interface particles as shown in Fig. 6. Therefore the dynamic boundary condition at the interface can be expressed as follows:

$$P_{i,interface} = P_{IMG} \quad (4.8)$$

However, MPS used the concept of particle, so the pressure acts on the center of particle. Moreover, pressure on the entire particle is the same. Therefore, hydrostatic pressure correction should be added cross the interface layer.

$$P_{i,interface} = P_{IMG} + g\rho_i v_i + g\rho_{IMG} v_j \quad (4.9)$$

With consideration of surface tension, the Eq. (4.9) can be rewritten as follows:

$$P_{i,interface} - P_{IMG} - g\rho_i v_i - g\rho_{IMG} v_j = \sigma\kappa \quad (4.10)$$

where σ is surface tension and κ is curvature of interface. The σ can be defined from various open literature, and κ can be calculated in the surface tension model.

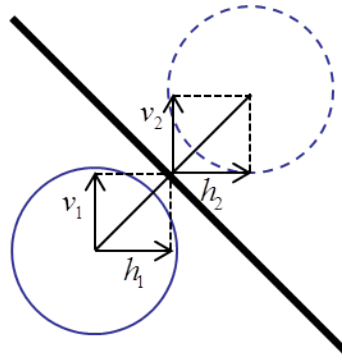


Figure 6 Interface particle and imaginary reference particle

3. Buoyancy-Correction Model

When an object is immersed or submerged, a difference of density between object and surrounding fluids can cause a buoyancy force which is related to displacement. MPS uses particle number density instead of density of fluid; the buoyancy force can be

calculated by the particle interaction method. In the MPS, the pressure includes both dynamic and hydrostatic pressure. However, the self-buoyancy of the center particle due to the surrounding fluid of different density is not included because the kernel function is omni-spread from the center value with axial symmetry. Therefore, consideration of self-buoyancy can be necessary to simulate multi-liquid problems.

In order to find the self-buoyancy of the center particle, let us consider the following two cases shown in Fig. 7. In both cases, two particles of different density are arranged vertically and the particle with the lighter density is center particle. In the first case, the lower particle is regarded as the center particle, and in the second case, the upper particle is regarded as the center particle. The self-buoyancy of the center particle can, for example, be obtained by subtracting the pressure of the upper particle from the lower particle. Therefore, self-buoyancy can be expressed as follows:

$$(P_i + \rho_i gr) - (P_j + \rho_j gr) = (P_i - P_j) + (\rho_i - \rho_j) gr \quad \text{for case I} \quad (4.11)$$

$$(P_j - \rho_j gr) - (P_i + \rho_i gr) = (P_i - P_j) + (\rho_i - \rho_j) gr \quad \text{for case II} \quad (4.12)$$

In these equations, the particle radius r can be generalized to half of the only vertical distance between two particles i.e. $r = (z_j - z_i) / 2$. The pressure P_i and P_j in the first term on the right-hand-sides of Eqs. (4.11) and (4.12) are already calculated in the Poisson pressure equation solver of the MPS method, while the second term on the right-hand-sides of Eqs. (4.11) and (4.12) can be implemented into the pressure gradient model as the buoyancy correction model. Therefore, the pressure gradient for multi-liquid MPS with buoyancy-correction can be expressed as follows:

$$\langle u \rangle_i' = -\frac{\Delta t d}{\rho_i n^0} \left[\sum_{j \neq i} \frac{(P_j - P_i)}{|\vec{r}_j - \vec{r}_i|^2} (\vec{r}_j - \vec{r}_i) w(|\vec{r}_j - \vec{r}_i|) \right. \\ \left. - \sum_{j \neq i} \frac{g(\rho_j - \rho_i)(z_j - z_i)}{(|\vec{r}_j - \vec{r}_i|)^2} (\vec{r}_j - \vec{r}_i) c_B w_B(|\vec{r}_j - \vec{r}_i|) \right] \quad (4.13)$$

where w_B is the kernel function for the buoyancy-correction model, which is the same as Eq. (3.3) but the effective range, r_e , is 1.5. The symbols z_j and z_i are vertical positions of particles j and i , and c_B is the velocity-adjustment parameter similar to that used in Shirakawa et al. (2001). Its default value is 0.5. The wall and dummy particles are not included in this correction. The present buoyancy-correction model is more straightforward and theoretically clear compared to that of Shirakawa et al. (2001) that includes several arbitrary empirical parameters. In the case of the single-phase fluid, the buoyancy-correction term vanishes.

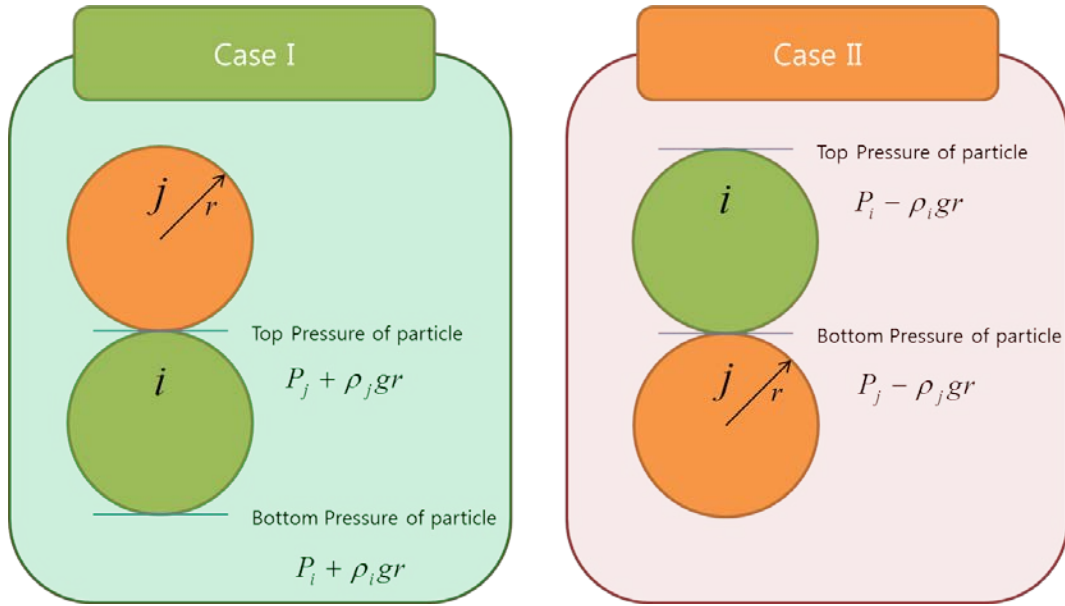


Figure 7 Self-buoyancy calculations

4. Surface Tension Model

The surface tension is a well-known resistance forces between two immiscible fluids contacting with discontinued density, for example water and air, which is called a free surface. The origin of surface tension is due to the intermolecular attractive force or cohesive force that acts on the interface. This surface tension can be regarded as the external force of Bernoulli's equation which can be expressed as follows:

$$\rho \frac{Du}{Dt} = -\nabla P + \mu \nabla^2 u + \rho g + \sigma \kappa \delta \vec{n} \quad (4.14)$$

where σ is the surface tension coefficient, κ is curvature of the interface, δ is the delta function which indicates particles are interface particle or not, and \vec{n} is the unit vector vertical to the interface

The last term on the left-hand-side of Eq. (4.14) represents surface tension. In order to calculate surface tension, four unknown variables need to be revealed. The surface tension coefficients are found in many tables which are already outlined. δ is the delta function which is zero for a particle not interface, and one for an interface particle. By considering the concept of MPS, the delta function of last term on the right-hand-side of Eq. (4.14) can vanish if the surface tension is applied only to the interface particle. In order to measure the curvature or interface, two additional particle number densities are newly introduced for surface tension.

$$\begin{aligned} n_i^{ST1} &= \sum_{j \neq i} w^{ST1} (|r_j - r_i|) \\ n_i^{ST2} &= \sum_{j \neq i} w^{ST2} (|r_j - r_i|) \end{aligned} \quad (4.15)$$

where,

$$w^{ST1}(r) = \begin{cases} 1 & (0 < r \leq r_e^{ST}) \\ 0 & (r_e^{ST} \leq r) \end{cases} \quad (4.16)$$

$$w^{ST2}(r) = \begin{cases} 1 & (0 < r \leq r_e^{ST} \text{ and } n_j^{ST1} > n_i^{ST1}) \\ 0 & \text{Otherwise} \end{cases}$$

With two additional particle number densities, the curvature of the interface is calculated as:

$$2\theta = \frac{n_i^{ST2}}{n_0^{ST1}} \pi \quad (4.17)$$

$$\kappa = \frac{1}{R} = \frac{2 \cos \theta}{r_e^{ST}} \quad (4.18)$$

where n_0^{ST1} is the first additional particle number density for the surface tension model at the initial arrangement. This equation satisfies the assumption that if the interface is plane, the curvature should be zero. This method can calculate the curvature of the interface without drawing the interface and large deformation treatment is not necessary.

The unit normal vector is an important component to calculate surface tension because it can determine the direction of surface tension. Moreover, decomposed unit normal vector can determine the ratio of surface tension to horizontal and vertical. In order to calculate unit normal vector, all involved particles are interface particles and the neighboring particles have the same density as the center particle. The unit normal vector can be calculated by the following equations:

$$\mathbf{a}_i = \bar{n}_x \sum_{j \neq i}^{N_\xi} x_n + \bar{n}_y \sum_{j \neq i}^{N_\xi} z_n \quad (4.19)$$

$$\mathbf{n}_i^{normal} = \frac{\mathbf{a}_i}{|\mathbf{a}_i|} \quad (4.20)$$

where \mathbf{a}_i is the normal vector, and \mathbf{n}_i is its unit vector. The schematic model of normal vector of interface particle and curvature are shown in Fig. 8.

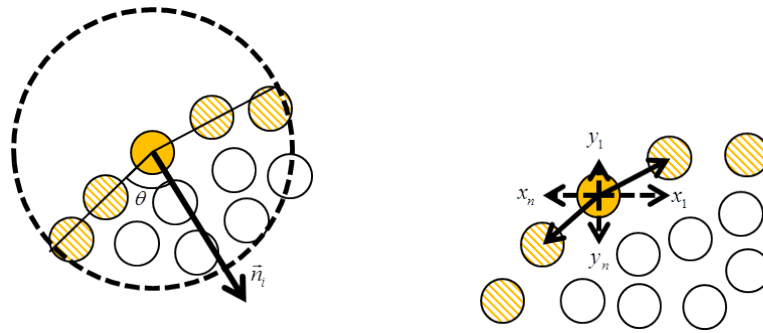


Figure 8 (a) Measurement of curvatures and (b) calculation of normal unit vector for surface tension

CHAPTER V
APPLICATIONS

1. Applications for Single-Liquid MPS

1.1 Broken Dam

To demonstrate the performance of the single-liquid MPS system, the broken-dam problem, which is a classic example for validation of the Lagrangian formulation, is simulated and compared with the experiment. The schematic model is shown in Fig. 9. The width and height of the water column are 0.15m and 0.3m, respectively. This water column is located in a rectangular tank which has dimensions of 0.6m width and 0.6m height. The reference point on the right wall with the distance of 0.01m from the bottom is selected for measuring the pressure. The water column is collapsed spontaneously with gravity. In this simulation, the initial particle distance is set to 0.0025m and 7,692 fluid particles and 3,936 wall and dummy particles are used. The water density is $1,000\text{kg/m}^3$, the gravitational acceleration is 9.81m/s^2 , and the kinematic viscosity is $10^{-6}\text{m}^2/\text{s}$.

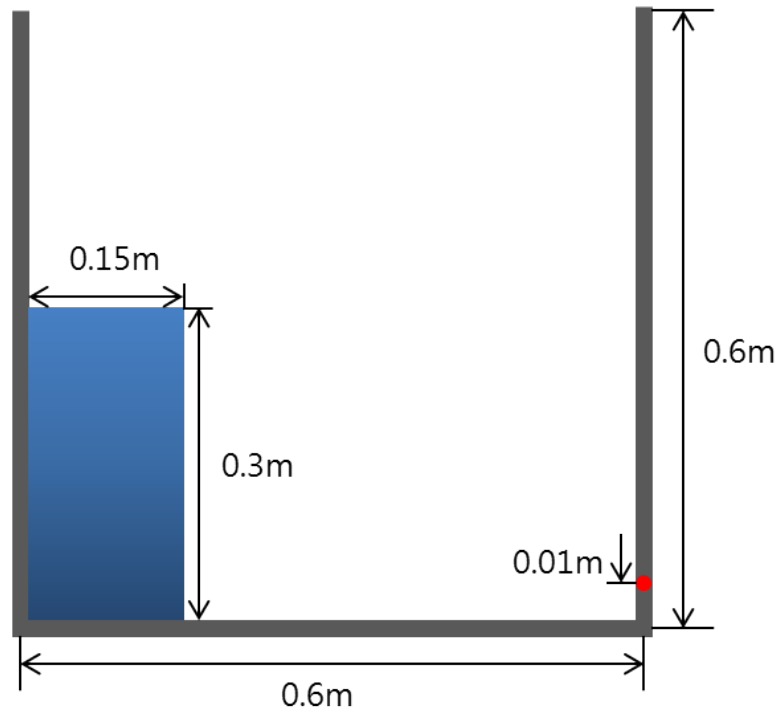


Figure 9 Schematic model for broken dam

Fig. 10 shows the snapshots of simulation and compared to experiment by Koshizuka et al (1995). Both captured images are well matched at each time. According to snapshot, the collapsed water column run to the wall and collided the right wall near 0.3 sec. The wave went up along the wall due to its velocity; then it falls by gravitational force near 0.8 sec. Fig. 11 shows the pressure history from simulation by MPS at every time step. The reference point is on the right wall and 0.01m away from the bottom. According to pressure history, the first peak is induced by the collision of the broken water column at time 0.3 sec. The interesting point is the second peak which is caused by the fall of the water column along the right wall. The third peak is caused by a rebounded wave from the left wall.


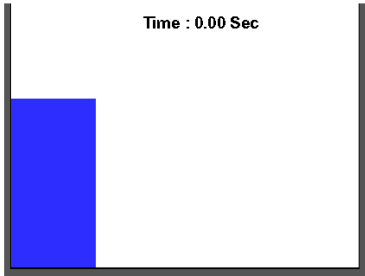
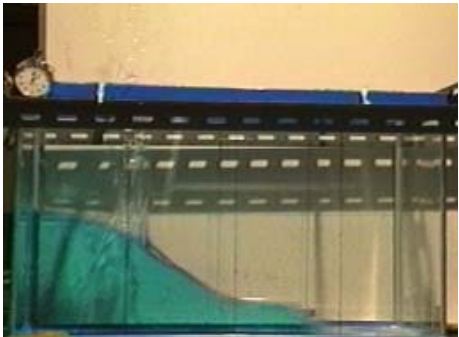
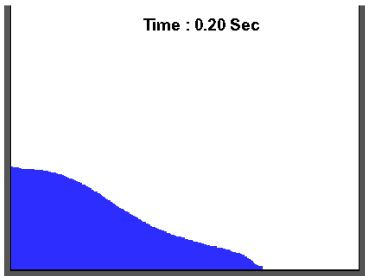
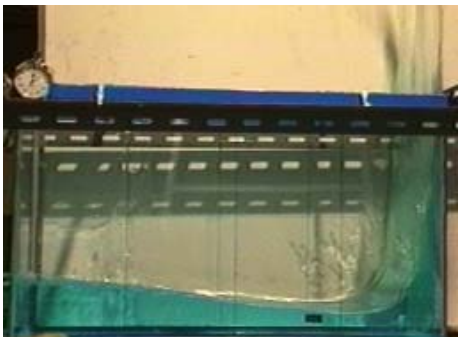
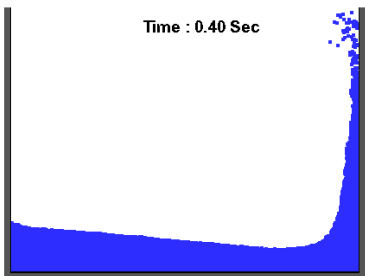

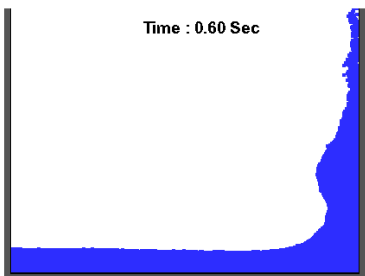
Time	Experiment	Simulation
0.0 Sec		
0.2 Sec		
0.4 Sec		
0.6 Sec		

Figure 10 Comparison of snapshots of broken dam

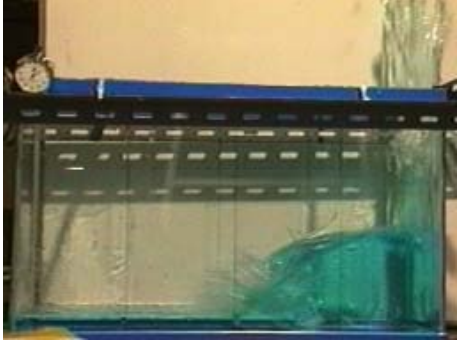
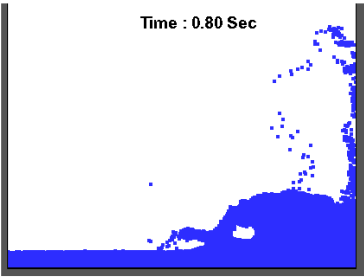
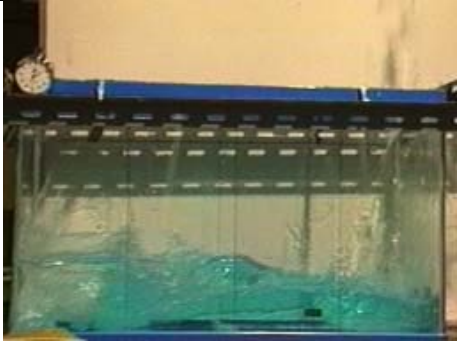
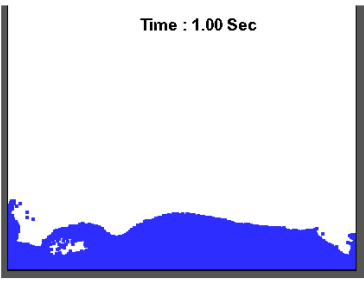
Time	Experiment	Simulation
		
		

Figure 10 continued

In order to check the correlation of initial particle distance, the convergence test was performed. The initial distance of 0.01m, 0.005m and 0.0025m are selected. Fig. 11 (b) shows the comparison of pressure with various initial particle distances. Three cases had similar pressure history for first and second peaks, however, third peak, which is occurred by reflected wave from left wall, was not observed in case of 0.01m. Third peak was observed in both cases of 0.005m and 0.0025m. Therefore, the initial particle distance should be less or equal to 0.005m for proper prediction.

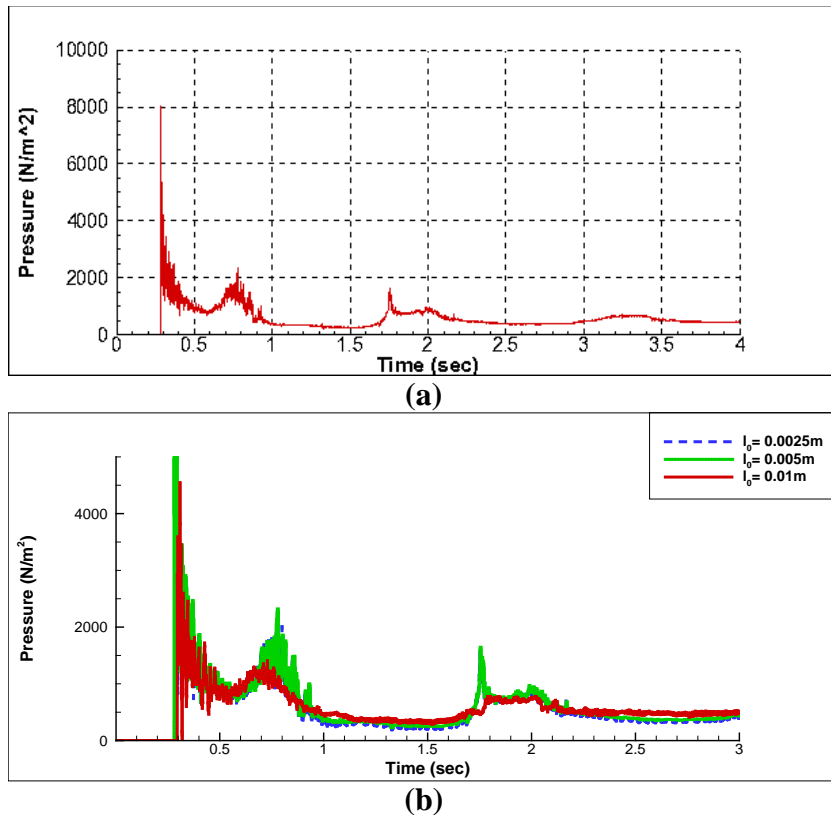


Figure 11 Pressure history at reference point (a) $l_0 = 0.005\text{ m}$ (b) $l_0 = 0.01\text{ m}$, 0.005 m , and 0.0025 m

1.2 Sloshing Tank for Single-Liquid

The water sloshing problem inside the two-dimensional rectangular tank with forced harmonic oscillation motion is evaluated and obtained results are compared against experimental results of Kishev et al. (2006). The schematic simulation model is shown in Fig. 12. The width and height of the tank are 0.6m and 0.3m, respectively. The water depth is 0.12m. The reference point for measuring pressure is 0.1m away from the bottom. The tank is forced to move sinusoidally in a horizontal direction which is expressed as follow:

$$X_H = A \sin\left(\frac{2\pi}{Tt}\right) \quad (5.1)$$

where X_H is horizontal position, A is amplitude, T is period, and t is time. In this study, A is set to 0.05m and two periods close to natural period, 1.3sec and 1.5sec, are selected. In this simulation, 4,000 particles are used. Among them, 3,000 particles are used for fluid and the rest are used for wall and dummy particles. The gravitational acceleration is 9.81m/s^2 , density of fluid is $1,000\text{kg/m}^3$, and the kinematic viscosity is $10^{-6}\text{m}^2/\text{s}$. The surface tension is not applied to this problem. The simulation runs until 16.0 seconds and the pressure history is compared against experiment by Kishev et al (2006). Fig. 13 is snapshots of the numerical simulation at $T = 1.3\text{s}$, and they are compared to experiments. Figs. 14a and 14b show the comparison of impact loads between the experiment and simulation at $T = 1.3\text{s}$ and $T = 1.5\text{s}$. The primary peaks are caused by slamming onto the vertical wall and the secondary peaks are caused by the fall of the water column along the wall. The trend of the pressure signal between the experiment and MPS shows good agreement.

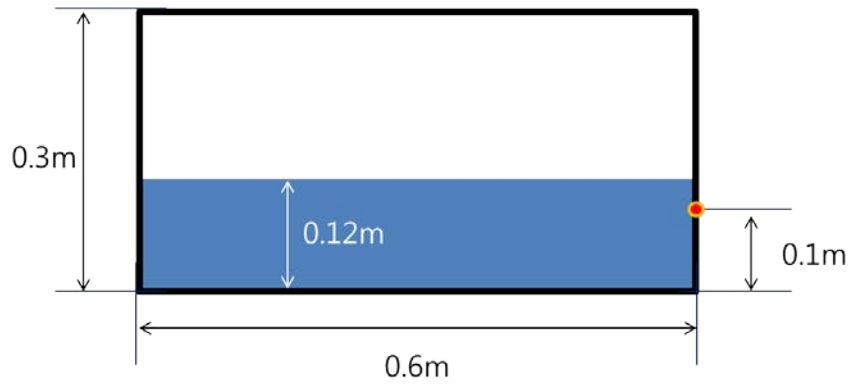


Figure 12 Schematic model for the sloshing problem

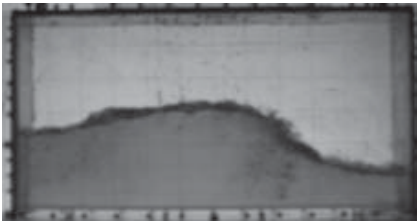
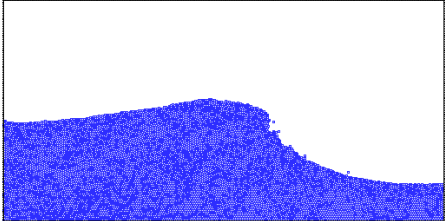
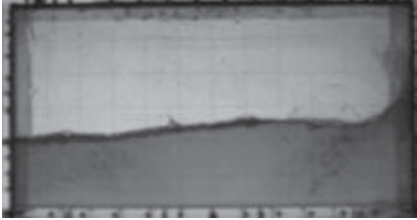
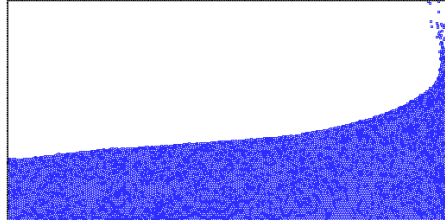
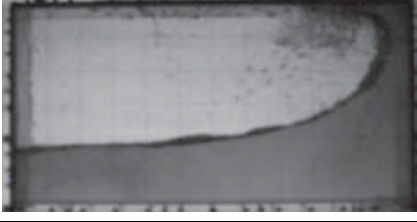
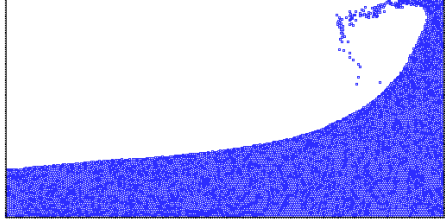
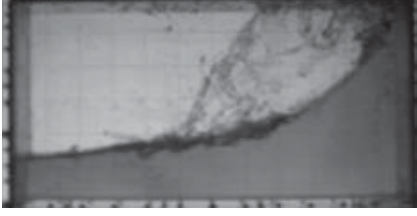
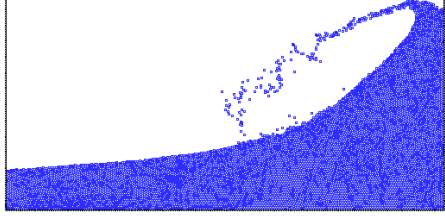
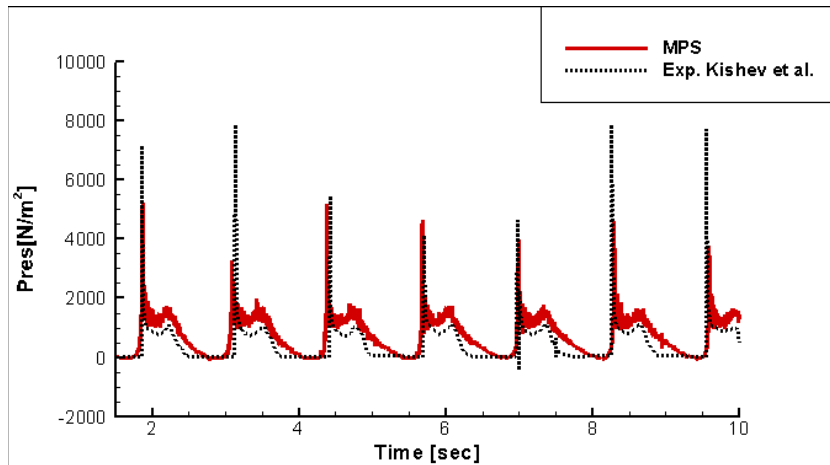
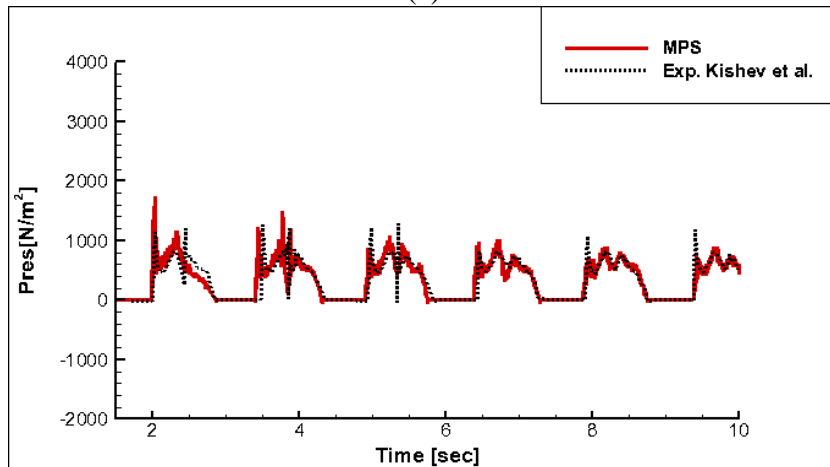
Time	Experiment	Simulation
0.1		
0.2		
0.3		
0.4		

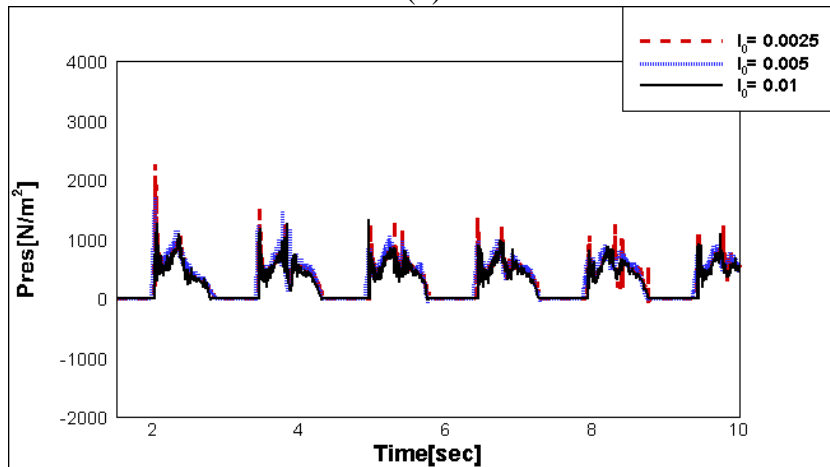
Figure 13 Snapshots of sloshing under harmonic oscillation



(a)



(b)



(c)

Figure 14 Pressure history comparison between experiment and numerical simulation at (a) $T=1.3$ sec and (b) $T=1.5$ sec

The sensitivity of initial particle distance is also investigated in case of sloshing at period $T = 1.5\text{sec}$. Fig 14 (c) shows the pressure comparison among various initial particle distance and all cases have the similar peak period and magnitude.

2. Advancement of MPS to Multi-Liquid Problems

2.1 Interface Particle Tracking

A proper method for identifying both free surface and interface is most important for multi-liquid problems because of applying the multi-liquid model to the free surface and interface particle. In this regard, a proper interface tracing method was suggested previously which was a modified free surface particle tracing method by adding additional conditions. In this section, proper parameters can be selected through numerical tests with arbitrary numbers through comparison of several cases. Revisiting Section 1 of Chapter IV, the equations of interface particle searching method can be found.

$$\beta_4 n^0 < \langle n \rangle_{i,\xi} < \beta_5 n^0 \quad (5.2)$$

$$N_{i,\xi} < \beta_6 N_0 \quad (5.3)$$

In order to obtain appropriate parameters, several cases with different parameters which are given in Table 1 are performed and compared through snapshots.

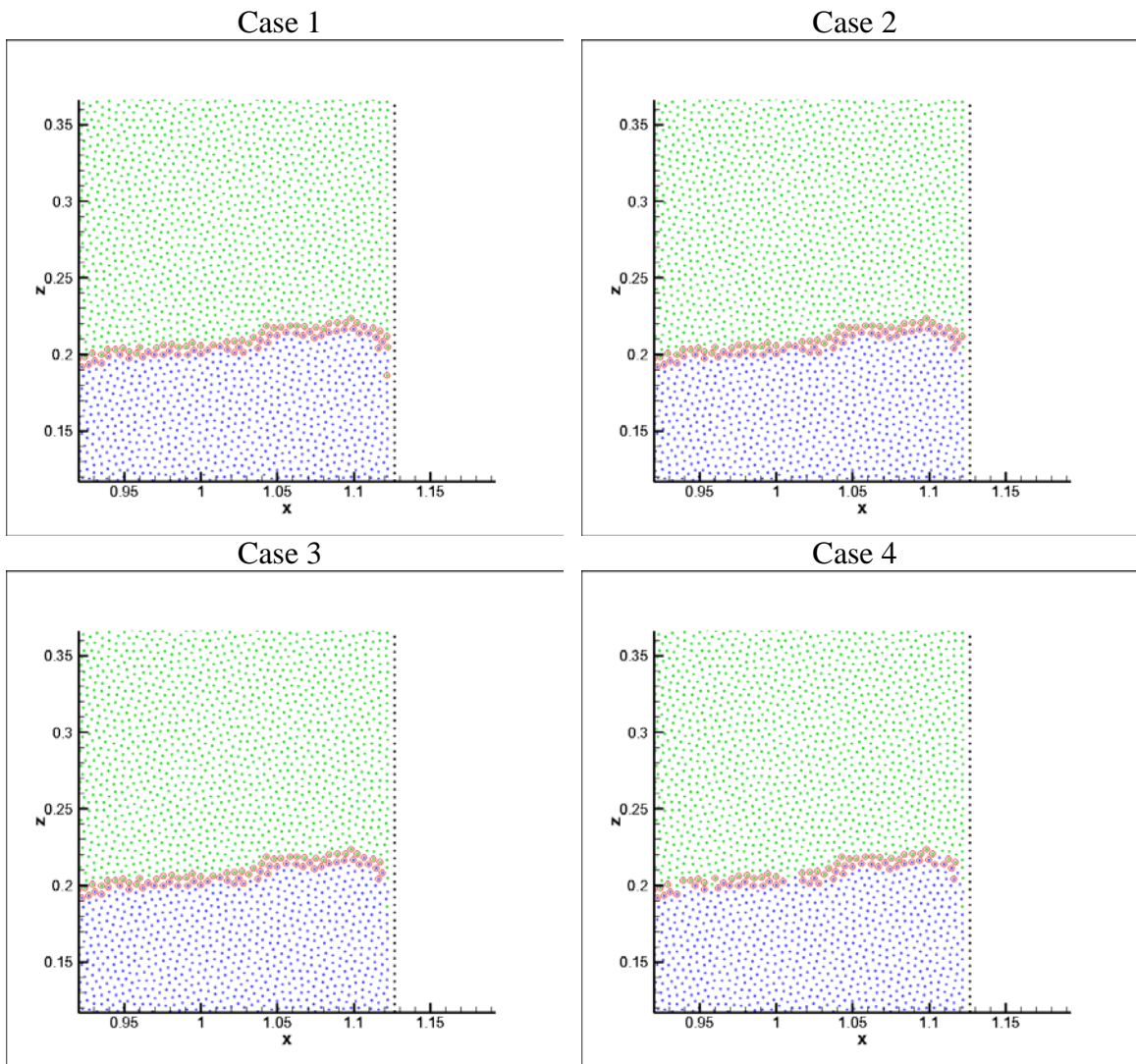


Figure 15 Tracing of interface particles

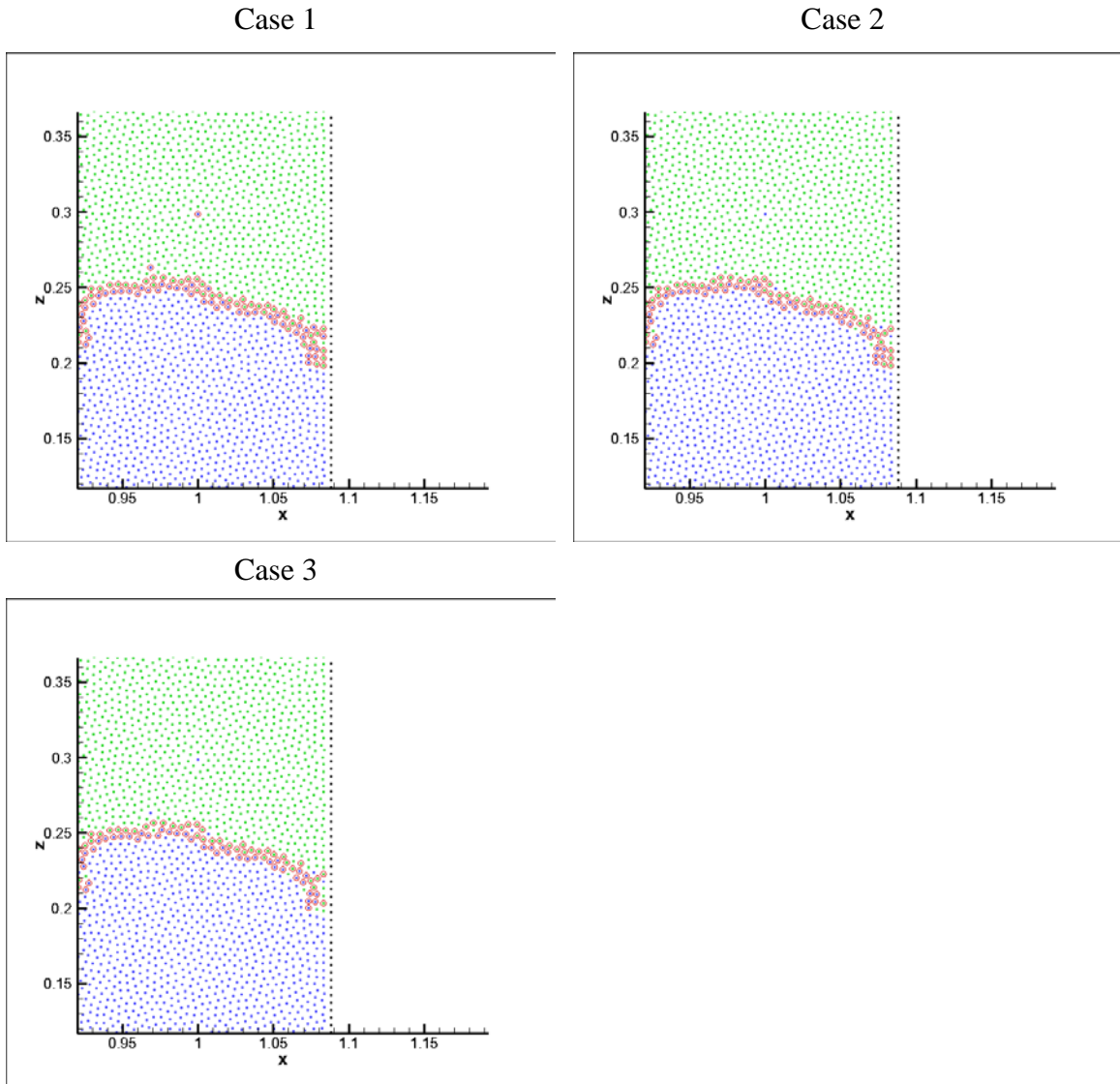


Figure 16 Tracing of interface particle under violent motion

Table 1 Table of Parameters Used

Case	β_4	β_5	β_6
1	0.2	0.97	0.85
2	0.3	0.97	0.85
3	0.4	0.97	0.85
4	0.5	0.97	0.85

The snapshots of each case are shown in Fig. 15. The circled particle in red denotes interface particles. According to the comparison of snapshots, Case 4 revealed that it is not a good method to find the interface particle due to the discontinued interface layer. The Cases 1,2 and 3 show a continued interface layer; however, Case 1 shows some detached particles from this group are indicated as interface particles. In order to make a more precise examination, violent motion is applied to the tank for Cases 1, 2, and 3, and then snapshots are compared as shown in Fig. 16. Through comparison of snapshots, Case 1 shows that faulty indicated interface particles exist. Therefore, the range of β_4 would be larger than 0.2 and less than 0.5. In this study, β_4 is set to 0.4.

2.2 Buoyancy Force Correction

A. Rising Velocity

The buoyancy force acts vertically only. In this regard, particle rising simulation can be a good example to validate buoyancy force. If one particle is lighter than the surrounding particles, then the lighter particle can rise spontaneously due to the buoyancy force. The rising velocity of the lighter particle is compared with theoretical velocity which is called terminal velocity. The terminal velocity can be expressed as follows:

$$v_t = \sqrt{\frac{4g(\rho_o - \rho_f)D_o}{3C_D\rho_f}} \quad (5.4)$$

where v_t is the terminal velocity including the buoyancy force, ρ_o and ρ_f are density of object and surrounding fluid, respectively, D_o is diameter of object, and C_D is drag coefficient which can be found in open literature.

The schematic simulation model for single particle rising is shown in Fig. 17. In this case, a total of 17,020 particles are used including 12,959 particles for water and 1 particle for oil. The initial particle distance is 0.005m. The densities of the surrounding fluid and oil are 1000kg/m^3 and 950kg/m^3 , respectively. The viscosity of the surrounding particle is $1 \times 10^{-6} \text{m}^2/\text{s}$ and $1.4 \times 10^{-6} \text{m}^2/\text{s}$ is used for the viscosity of oil. The vertical position of the oil particle is measured at each time step to obtain the vertical rising velocity shown in Fig. 18 (b); that velocity is compared with the theoretical terminal velocity. If the particle shape is assumed circular, the drag coefficient can be 0.9 ~ 1.4, then the terminal velocity can be $0.0483\text{m/s} \sim 0.0602\text{m/s}$. With a default value of velocity-adjustment parameter, ($C_B = 0.5$), the rising velocity is similar to the terminal velocity with $C_D = 1.2$. In order to clarify the velocity-adjustment parameter, a case with $l_0 = 0.01\text{m}$ is simulated. According to the terminal velocity, it can be $0.0683\text{m/s} \sim 0.0852\text{m/s}$. With drag coefficient as 1.2, the measured rising velocity well agrees with the terminal velocity as shown in Fig. 18 (a). The reason why both cases have a different starting point is that to avoid the bottom effect. Several particles should be located under the oil particle. The difference is caused by consideration with different initial particle distances.

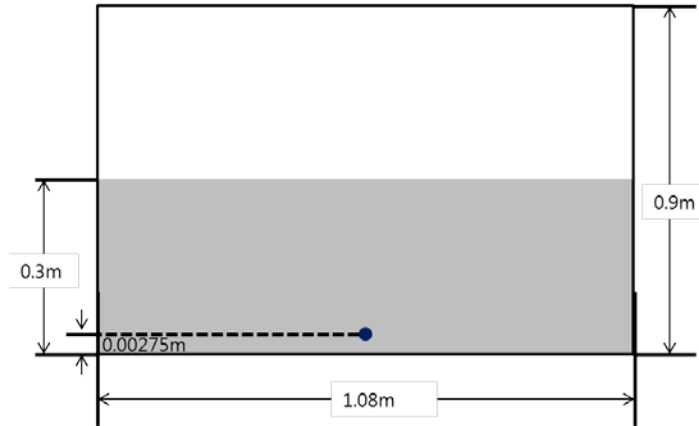


Figure 17 Schematic model for oil particle rising

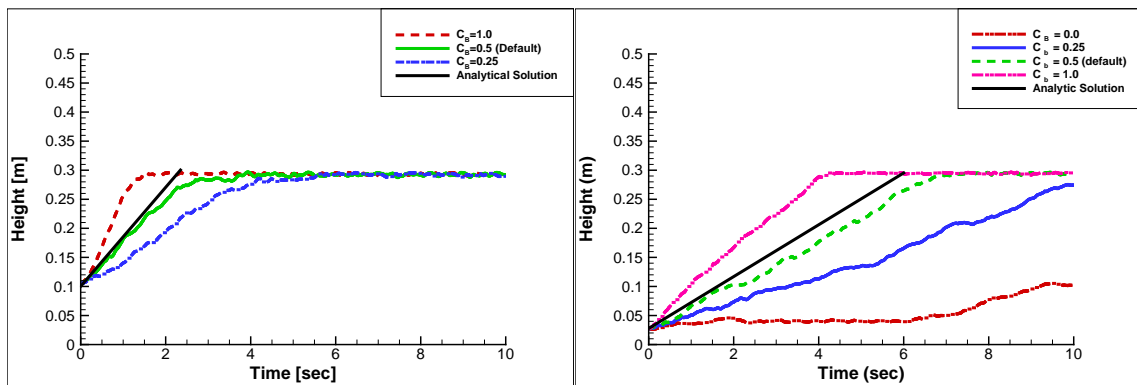


Figure 18 Vertical position of oil particle (a) $l_0 = 0.01$ and (b) $l_0 = 0.005$

B. Lateral Oil-Leaking

For quantitative comparison, a lateral oil leak problem is simulated as shown in Fig. 19. The oil spills out through the hole 0.5m away from the bottom of the inner tank due to hydrostatic pressure. The dimensions of outer and inner tanks, position and diameter of hole and properties of fluid are given in Table 2. A total 28,625 particles are used for the present simulation; the number of outer water particle is 20,520 that of the inner oil

particle is 4,975. 3,130 particles are used as wall and dummy particles. The initial particle distance is 0.005m. By measuring the oil level of the inner tank, the total leakage of oil can be estimated and is compared with an analytical solution based on Torricelli's Equilibrium Equation. Torricelli's Equilibrium Equation, Eq. (5.5), is derived from the quasi-static treatment of Bernoulli's equation which is convenient and useful (Simecek-Beatty et al., 2001). The oil height loss can be estimated by Eq. (5.5). The Torricelli's equilibrium equation and the oil height loss can be expressed as follows:

$$h(t) = \frac{1}{1 + \left(\frac{A_i}{A_o}\right)} \times \left[\frac{g \left(\frac{A_h}{A_i}\right)^2 \left(1 + \frac{A_i}{A_o}\right)^2}{2 \left(1 - \left(\frac{A_h}{A_i}\right)^2\right)} (TF \times t - t_{\max})^2 + \frac{\rho_o}{\rho_i} H_o + \frac{A_i}{A_o} H_i \right] \quad (5.5)$$

with

$$t_{\max} = \frac{\left(\frac{A_i}{A_o}\right)}{1 + \left(\frac{A_i}{A_o}\right)} \times \sqrt{\frac{2}{g} \left[1 - \left(\frac{A_h}{A_i}\right)^2\right] \left[H_i - \frac{\rho_o}{\rho_i} H_o \right]} \quad (5.6)$$

where t_{\max} is end time of leaking, A is surface area, H is vertical distance away from the bottom of each tank, TF is Torricelli's factor, which indicates the ratio of actual leaking speed to that predicted by Bernoulli's equation, and subscripts i, o , and h indicate inner and outer tanks and hole, respectively. The estimated oil height loss is compared with that measured by simulation. The Torricelli's factor for the present case, 0.558, is obtained by an experiment by Kim et al. (2001), while it is 1.0 when only hydrostatic pressure balance is considered. In comparison to the theoretical analytic

solution, it is shown that MPS has good agreement with the analytic solution. Moreover, the present MPS with multi-liquid models such as buoyancy and boundary conditions at interface has better agreement than the MPS without the multi-liquid model as shown in Fig. 21. For this simulation, the surface tension is not included. The snapshots of simulation from currently improved MPS for multi liquid system are shown in Fig. 20.

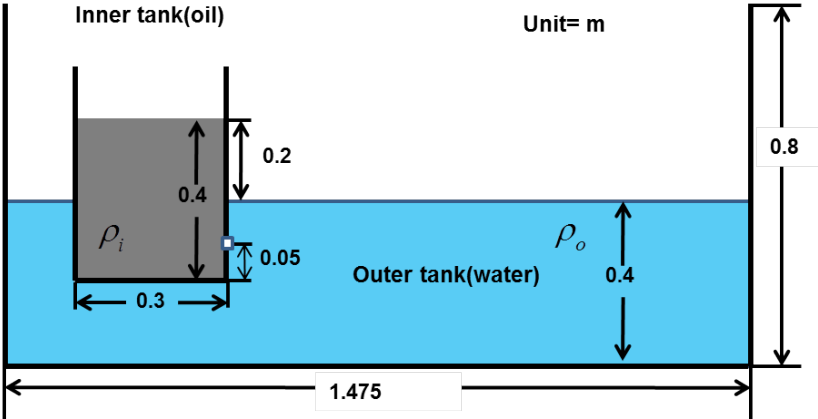


Figure 19 Schematic model of lateral oil leaking

Table 2 Properties of Fluids for Oil Leaking Simulation

Fluid	Density	Kinematic Viscosity
Water (Outer Tank)	$997\text{kg} / \text{m}^3$	$0.546 \times 10^{-4} \text{m}^2 / \text{s}$
Oil (Inner Tank)	$917.55\text{kg} / \text{m}^3$	$0.890 \times 10^{-6} \text{m}^2 / \text{s}$

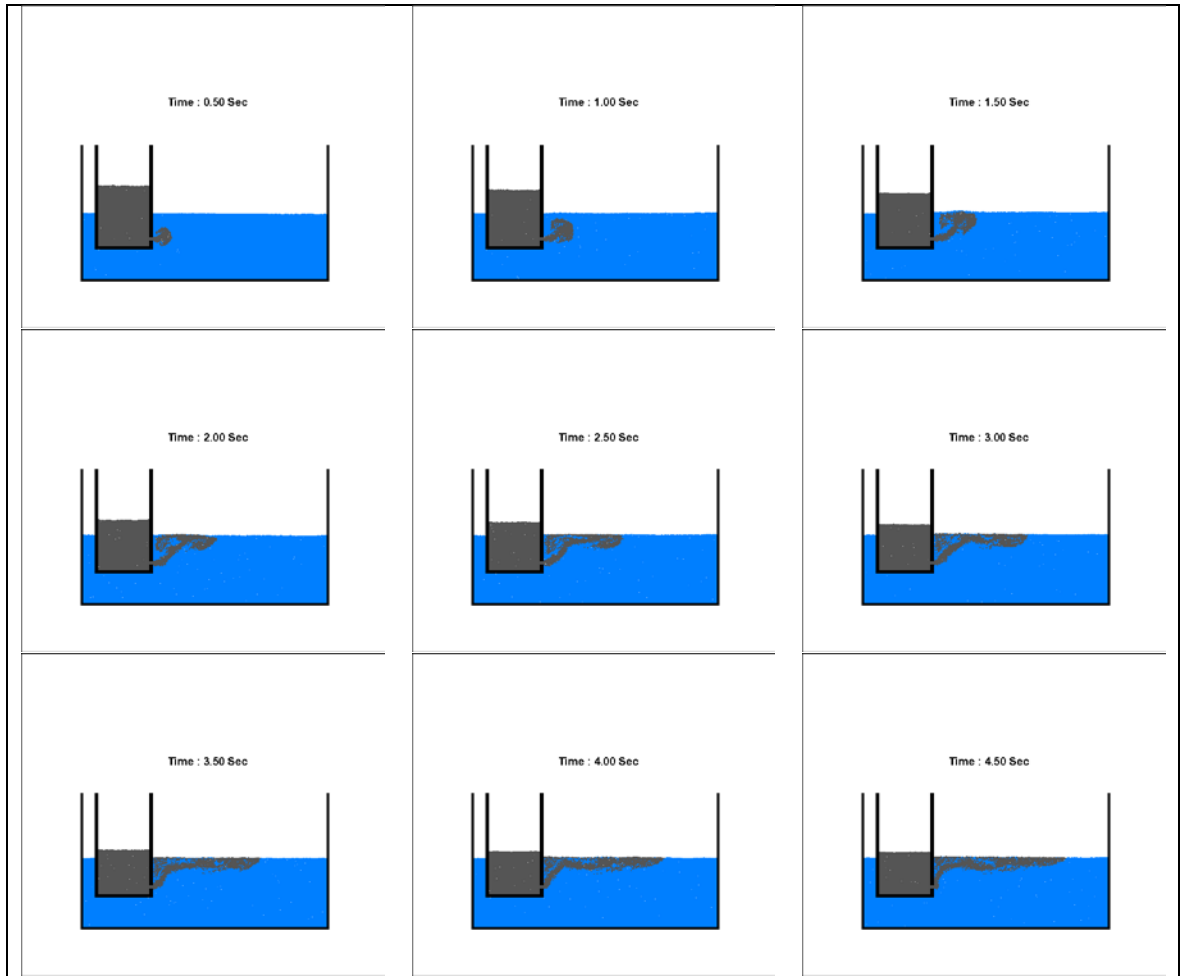


Figure 20 Snapshots of lateral oil spill

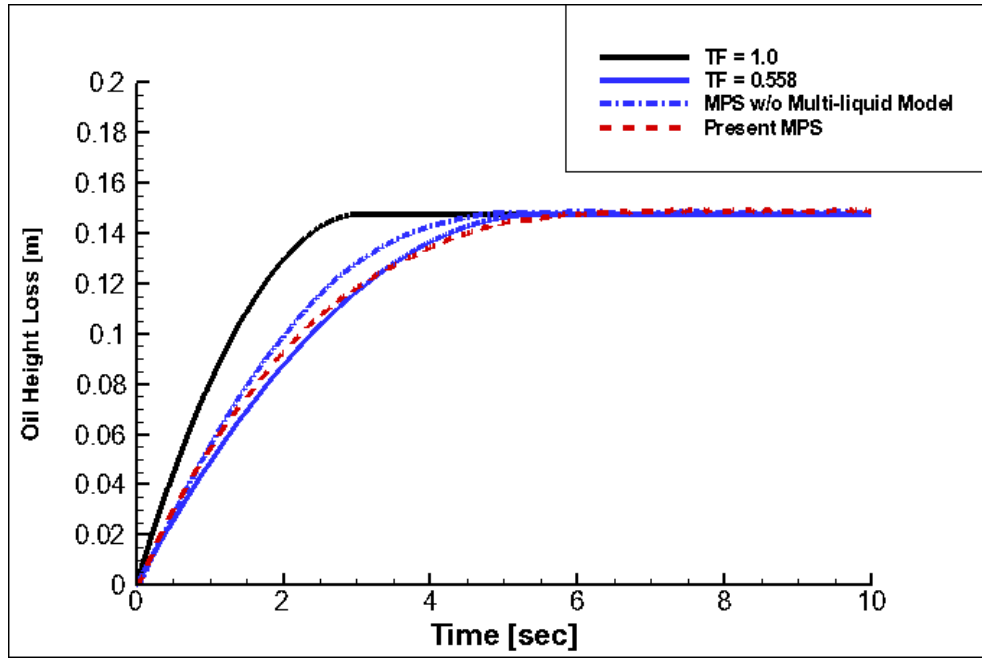


Figure 21 Oil height loss

2.3 Surface Tension

The simulation of a square droplet is simulated by MPS with a surface tension model. The initial fluid configuration is a square of length 75mm subjected to no gravitational forces. The simulated fluid is Ethanol which has $7.98 \times 10^2 \text{ kg/m}^3$ density, $1.4 \times 10^{-6} \text{ m}^2/\text{s}$ viscosity, and $2.361 \times 10^{-2} \text{ N/m}$ surface tension. Since no gravitational force is applied to the square droplet, the final form of droplet should be circular due to surface tension. Lamb (1945) investigated vibration for the cross-section area of the water column; the cross-section has deformation with period $\omega_{oscillation}$ theoretically. The oscillation of a square liquid droplet is a very popular test for the surface tension model

in the numerical method. As shown in Fig. 22, the initial particle arrangement is 30×30 and the initial particle distance is 0.25mm.

The analytical solution for the oscillation frequency of two-dimensional droplet without gravitational force can be written as follows:

$$\omega_{oscillation} = \frac{s(s^2 - 1)\sigma}{\rho R_0^3} \quad (5.7)$$

where $\omega_{oscillation}$ is frequency of oscillation, σ is surface tension, R_0^3 is radius of droplet, and s is the mode number of oscillation. In this study, the particles are located on the Cartesian coordinate, thus the radius can be transferred by the equivalent radius of droplet which can be expressed as $R_0 = L\sqrt{1/\pi}$, where L is length of square droplet. The mode number of oscillation can be found in Lamb (1945) as 1 for circle, 2 for ellipse, 3 for triangle, and 4 for square. The analytical oscillation period of the square Ethanol droplet should be 1.3 sec in the present case.

The transient shapes of the oscillation liquid droplet are shown in Fig 23 at several time steps. Fig 23 shows that the oscillation period is 1.3s which is well-agreed with the analytical solution. The square droplet was rotated by 45° at 0.65s and 1.95s, while it turned to the initial shape at 1.3s and 2.6s. After several oscillations, the square droplet approached the equilibrium spherical shape due to damping which was induced by numerical dissipation and the viscous effect. Figs. 24 and 25 show the unit normal vector of the surface tension and direction of the force. The direction of the force can be defined by $\kappa\vec{n}$. Since the unit normal vector toward inside of fluid, the curvature can determine the force acting direction.

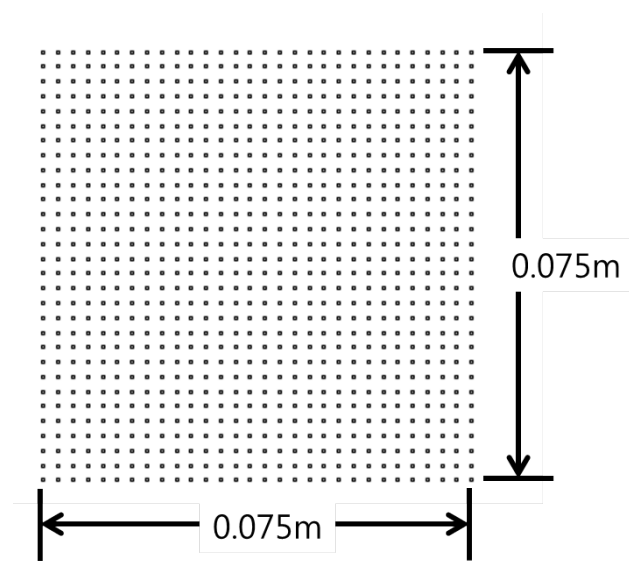


Figure 22 Schematic model for surface tension test on X-Y plane

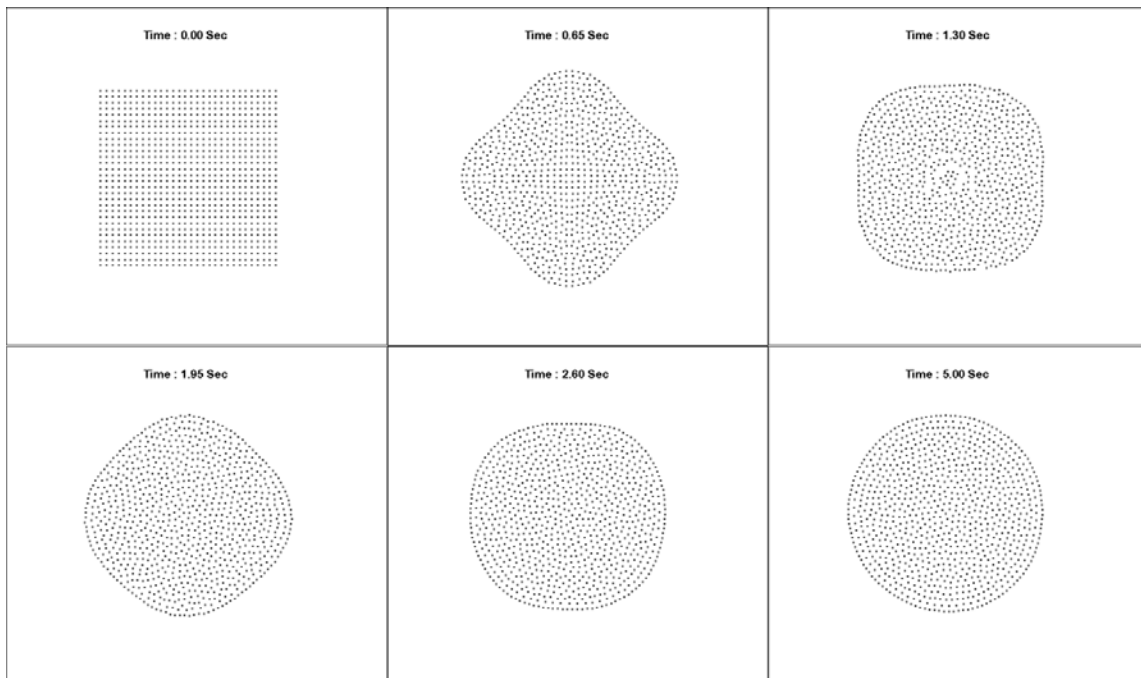


Figure 23 Examples of droplet vibration

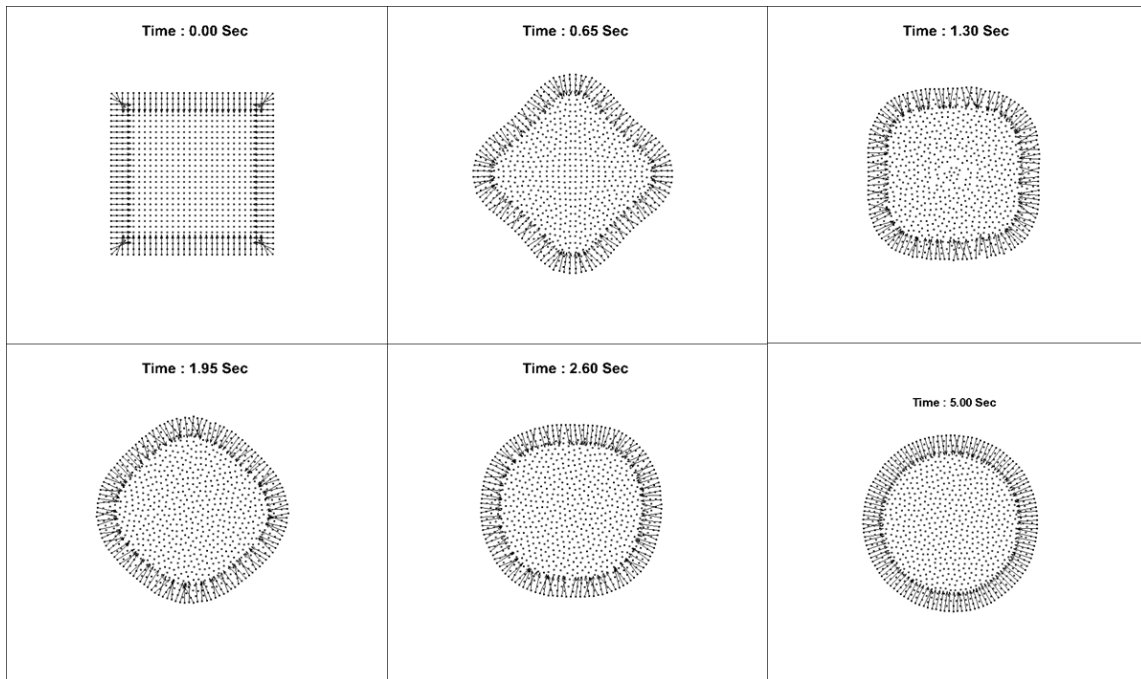


Figure 24 Normal vectors of droplet

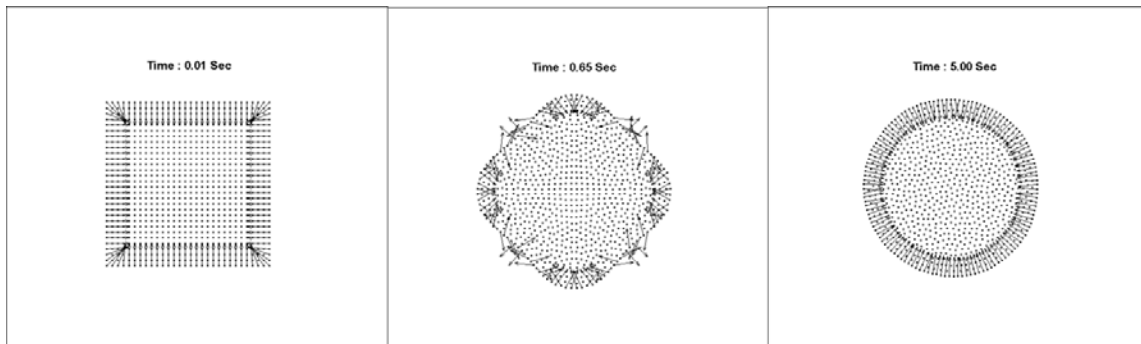


Figure 25 Direction of force

2.4 Sloshing Tank for Multi-Liquid

The multi-liquid simulation for stationary motion performed by the grid method can be found in some open literature, however, dynamic motion such as multi-liquid

sloshing has rarely been researched. In this section, the three-liquid-layer-sloshing is simulated by newly developed multi-liquid MPS and the results were compared against the experiment by Molin et al. (2012). All the simulation conditions were set equal to the experiment where the rectangular sloshing tank was partially filled by three different liquids; their properties are given in Table 3. The heaviest but less viscous liquid, Dichloromethane, was 15cm from the bottom of tank. Water was located in the middle layer with a height of 15cm from the Dichloromethane. At the top layer, Cyclohexane is located 38cm above the water. The tank was 1.08m long and 0.9m high as shown in Fig. 26. The air region above the Cyclohexane is regarded as a vacuum without particles. This present simulation used a total of 33,436 particles with 6,510 particles for the bottom layer, 6,510 for the middle layer, and 16,356 for the top layer. 4,060 particles were also used to represent the solid tank wall. For this arrangement, the initial particle distance was 0.005m.

Table 3 Properties of Liquids

	Density	Kinematic viscosity	Surface Tension Coefficient
Dichloromethane(D)	$1,300\text{kg} / \text{m}^3$	$3.0 \times 10^{-7} \text{m}^2 / \text{s}$	$0.0278 \text{ N} / \text{m}$
Water(W)	$1,000\text{kg} / \text{m}^3$	$1.0 \times 10^{-6} \text{m}^2 / \text{s}$	$0.0727 \text{ N} / \text{m}$
Cyclohexane(C)	$780\text{kg} / \text{m}^3$	$1.3 \times 10^{-6} \text{m}^2 / \text{s}$	$0.00247 \text{ N} / \text{m}$

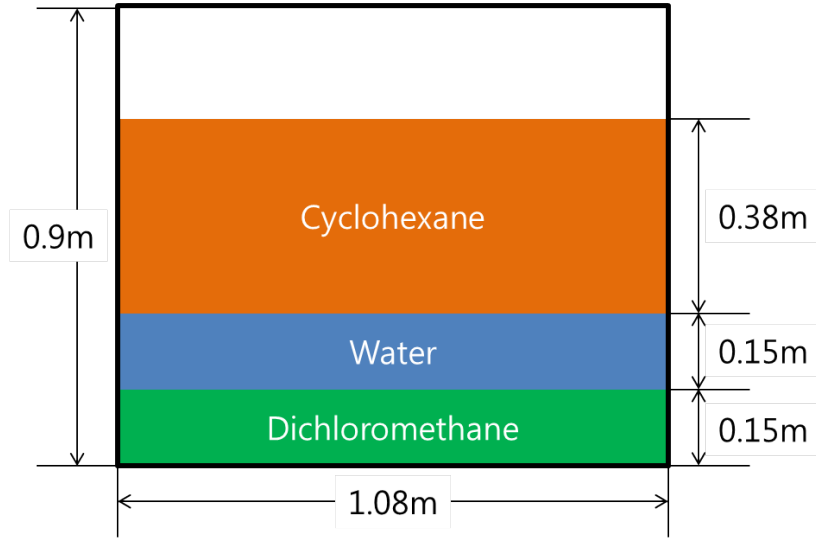


Figure 26 Schematic model for three liquid sloshing problem

A. Free Decay Test

The resonant sloshing frequencies at the three interfaces were obtained by the linear potential theory. Considering the multi-liquid-sloshing tank as shown in Fig. 26, the resonant frequencies can be calculated by providing null as the determinant of the undamped matrix of the linear system. The determinant has the form of a sixth-order polynomial in natural frequencies, ω , as follow:

$$A_6\omega^6 + A_4\omega^4 + A_2\omega^2 + A_0 = 0 \quad (5.8)$$

with

$$\begin{aligned} A_6 &= -r_2 - r_2^2 t_1 t_2 - r_3 t_2 t_3 - r_2 r_3 t_1 t_3 \\ A_4 &= g \lambda_n \left[t_1 t_2 t_3 (r_2^2 - r_2 r_3 + r_3) + r_2 (t_1 + t_2 + t_3) \right] \\ A_2 &= g^2 \lambda_n^2 \left[-r_2 (t_1 t_2 + t_1 t_3 + t_2 t_3) + r_3 t_2 t_3 + r_2^2 t_1 t_2 + r_2 r_3 t_1 t_3 \right] \\ A_0 &= g^3 \lambda_n^3 t_1 t_2 t_3 (1 - r_2)(r_2 - r_3) \end{aligned} \quad (5.9)$$

where

$$\begin{aligned}\lambda_n &= \frac{n\pi}{B} \\ t_i &= \tanh(\lambda_n h_i) \\ r_i &= \frac{\rho_i}{\rho_1}\end{aligned}\tag{5.10}$$

where subscription n denotes sloshing mode, and i represents the kind of fluid. The calculated resonant frequencies are given in Table.

In order to obtain the natural frequencies of interfaces numerically, the free-decay test was performed and obtained frequencies were compared with the theoretical resonant frequencies. The three interfaces were initially tilted by 5-degrees and 10-degrees and released to have subsequent free oscillations. The system is to oscillate spontaneously with the series of natural frequencies. The oscillations of each interface were measured at the left wall of the tank and mid of the tank, and the obtained time-domain data was converted to the corresponding frequency-domain spectra by Fourier-Transform as shown in Figs. 27 (a), (b), and (c). The peaks of spectra represent the locations of natural frequencies which well match the values obtained by the linear-potential theory. Additionally, since the fluids are immiscible, the coupling effects between interfaces were also observed. In Table 4, the theoretically calculated natural frequencies and the measured frequencies by the numerical simulation are represented. Since the theoretical natural frequencies were obtained by linear potential theory which does not consider viscosity of fluid, the free decay test was performed for inviscid fluid.

Fig. 27 (d), (e), and (f) shows the comparison of spectra. The results were similar since the interface motions are to be little influenced by viscosity.

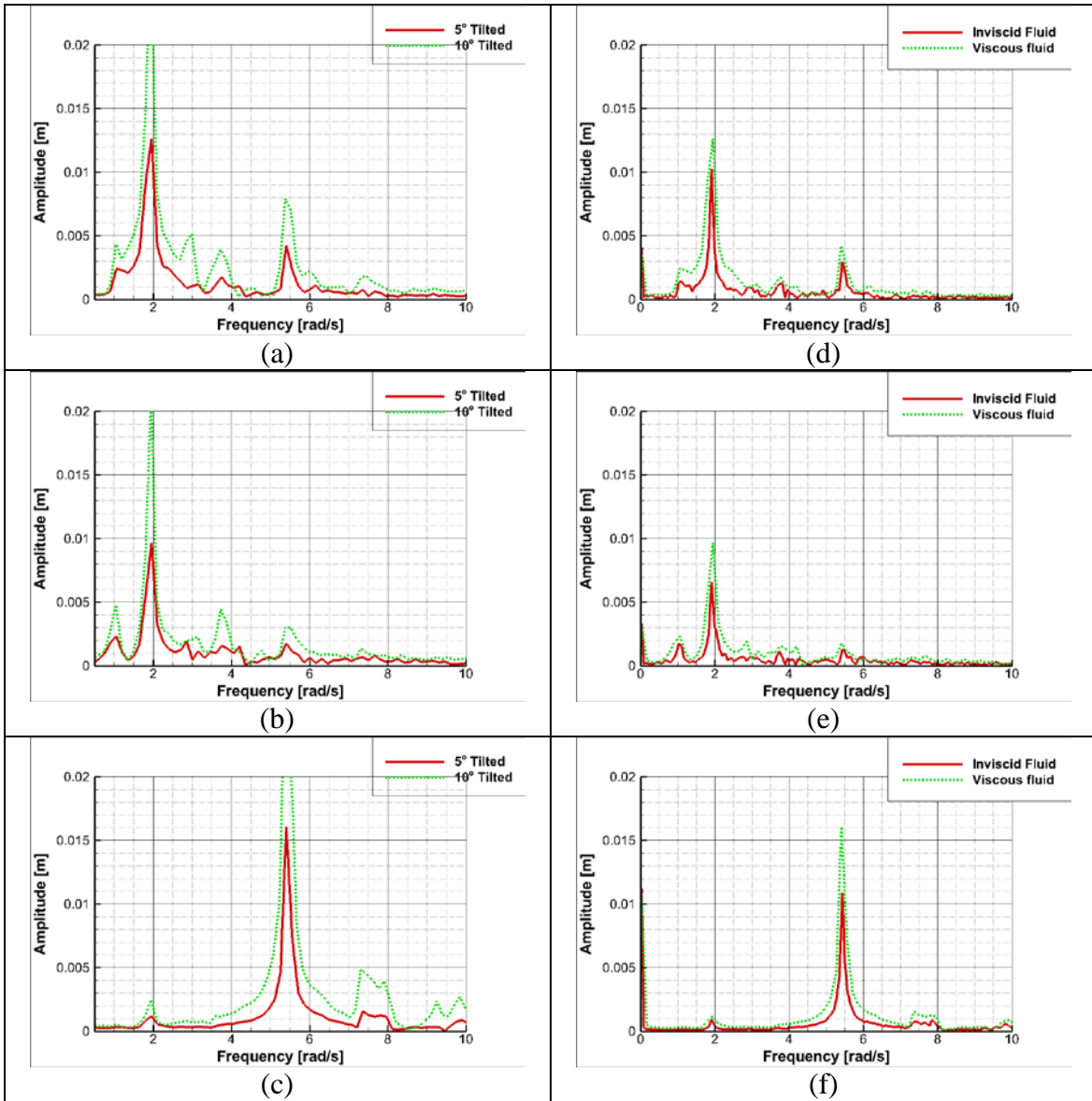


Figure 27 Result of free decay test: comparison by tilting angle at (a) CW- (b) WD-interfaces and (c) free-surface; comparison between viscous and inviscid fluid at (d) CW- (e) WD-interfaces and (f) free surface

Table 4 Angular Frequencies of Natural Modes

Angular Frequencies of the natural modes (<i>rad / s</i>)						
	Theoretical (Linear potential)			Numerical (Free Decay)		
	ω_c	ω_w	ω_D	ω_c	ω_w	ω_D
1	5.204	1.838	1.050	5.3	1.93	0.94
2	7.550	2.949	1.986	7.5	2.98	1.86
3	9.252	3.608	2.775	9.2	3.73	2.83
4	10.68	4.080	3.436	9.9	4.20	3.45

B. Three-Liquid-Sloshing under Harmonic Oscillation (Mild)

The aforementioned system is simulated under forced harmonic oscillations. In this case, the tank is forced to roll with 1-degree amplitude at 1.83-rad/s. The oscillation frequency is close to the lowest natural frequency of the middle interface. The interface oscillations are measured at left wall and center of tank at every time step. The left wall oscillations are compared with the corresponding experimental data from Molin et al. (2102) as shown in Fig. 28. Since the frequency is close to the lowest natural frequency of the middle layer, the lowest modal shape is generated for the middle layer (see Fig. 30) and subsequently influences the other interfaces. As expected, the interface elevation amplitude of the middle layer is the largest among interface oscillations. The oscillation of the bottom interface has the same frequency as the middle interface, but the amplitude is smaller than that of the middle interface. The interesting point of this case is the free-

surface oscillation which is interface of top layer has much less amplitude than others; it looks more wiggly, having both high and given frequencies, and its phase is slightly shifted compared to others, which is also observed in the experiment. Figs. 29 (a) and (b) plots 3-interfaces time history at the left tank wall and the mid tank. As shown in Figs. 29 (a) and (b), the WD interface at the left tank wall has an appreciably larger trough than crest and the WD interface at mid-tank has a secondary hump near the trough. Another interesting point is shown in Figs. 29 (a) and (b). Although the frequency of oscillation is close to lowest natural frequency of middle layer, it is close to the second natural frequency of the bottom layer. Thus the second modal shape is generated for the bottom layer and it affects the middle layer at the center of the tank as shown Figs. 29 (a) and (b). This phenomenon shows that in the case of multi-liquid-layer-sloshing, the relevant physics can be more complicated compared to the single-liquid-tank.

Figs. 31 (a) and (b) show the corresponding spectra of oscillations of interface which are converted by the Fourier Transform at the left tank wall and mid tank, respectively. The input frequency of tank oscillation can be shown in the spectra. The second peak shows the slowly varying motion which is doubled as input frequency.

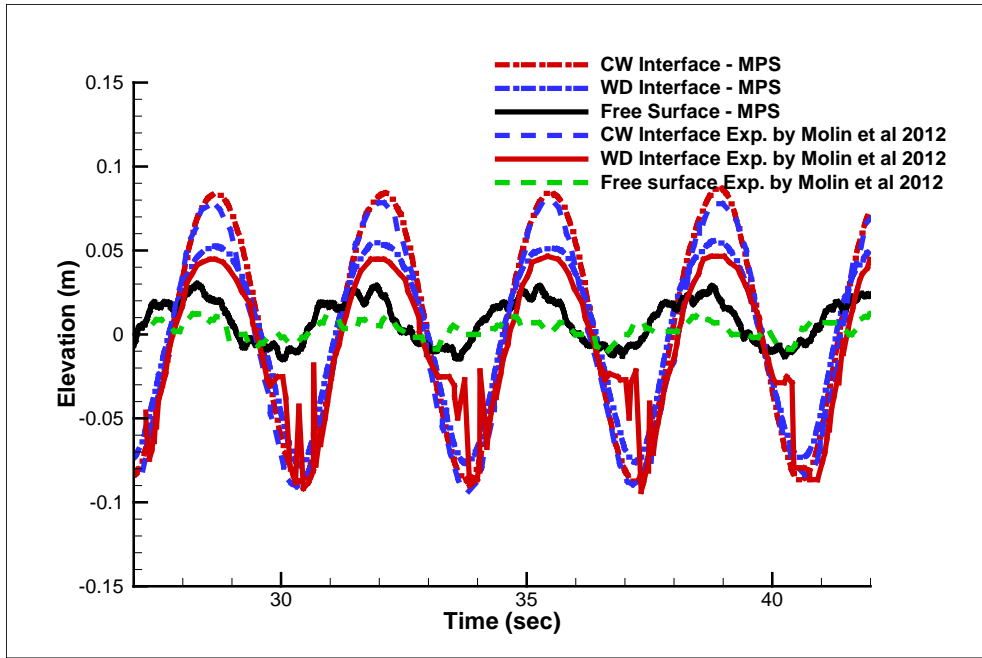


Figure 28 Elevation of interfaces with experiment

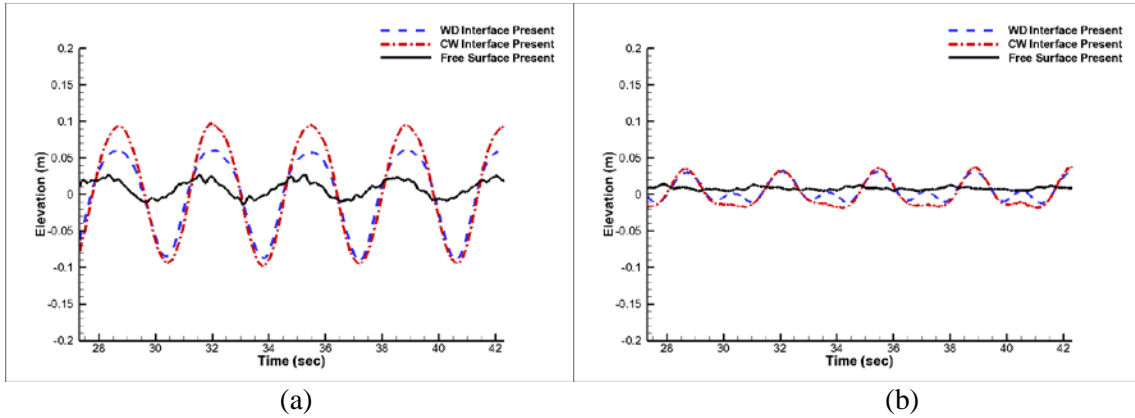


Figure 29 Interface oscillation for 1-degree roll at 1.83-rad/s at (a) left wall of tank and (b) mid tank

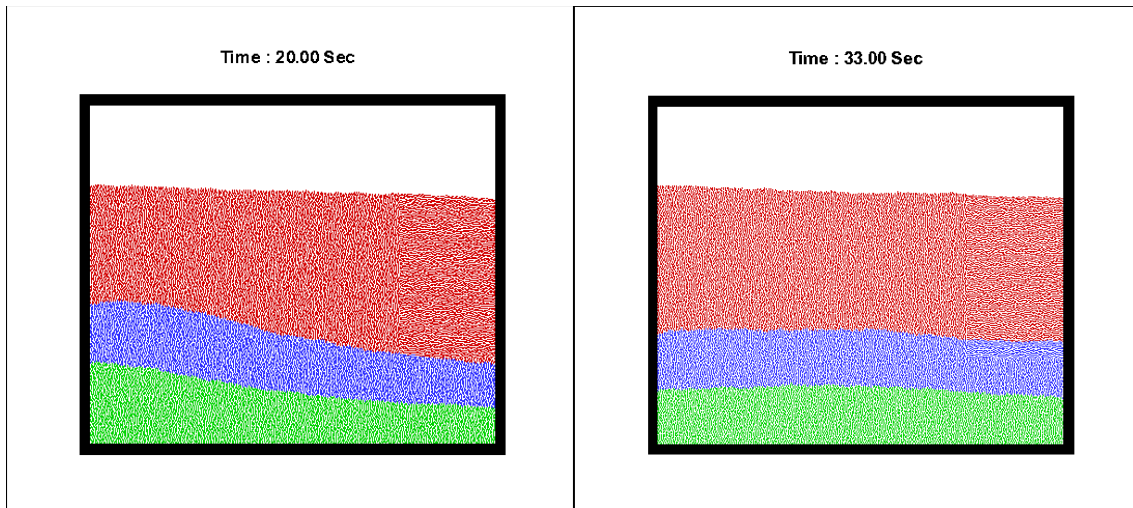


Figure 30 Snapshots of multi-liquid sloshing tank at time (a) 20 sec and (b) 33 sec

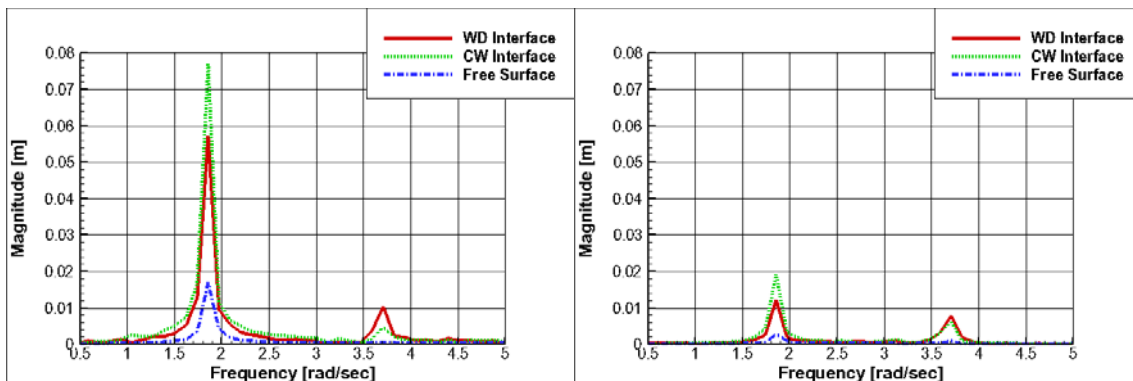


Figure 31 Spectra of interface at (a) left wall and (b) center

C. Convergence Test

Since MPS is based on the Lagrangian approach, particles have the same meaning as the grid. In the grid system, the number of grids affects the accuracy, thus finding a reasonable number of grids for efficient calculation time with reasonable accuracy is one of the most important factor for entire simulation. In this regard, several

cases with different number of particles are simulated and compared in the present simulations. Comparing the elevation of interfaces and their corresponding spectra are similar as shown in Figs. 32 and 33. The high number of particle produces more narrow spectra, but others are also applicable. In this regard, the smallest initial particle distance is set to 0.005m considering both accuracy and efficiency.

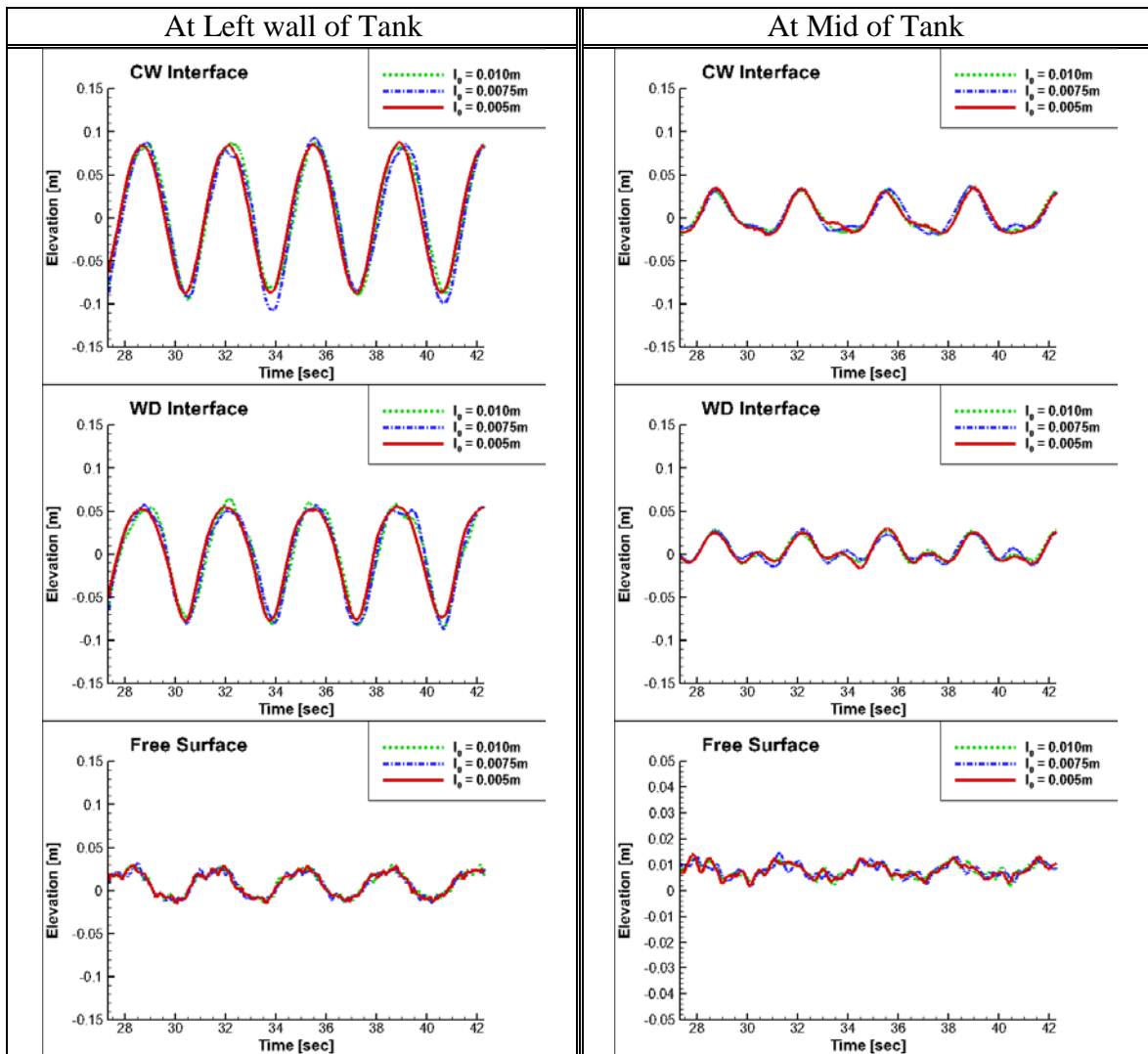


Figure 32 Comparisons of interface oscillations for convergence test with different particle size

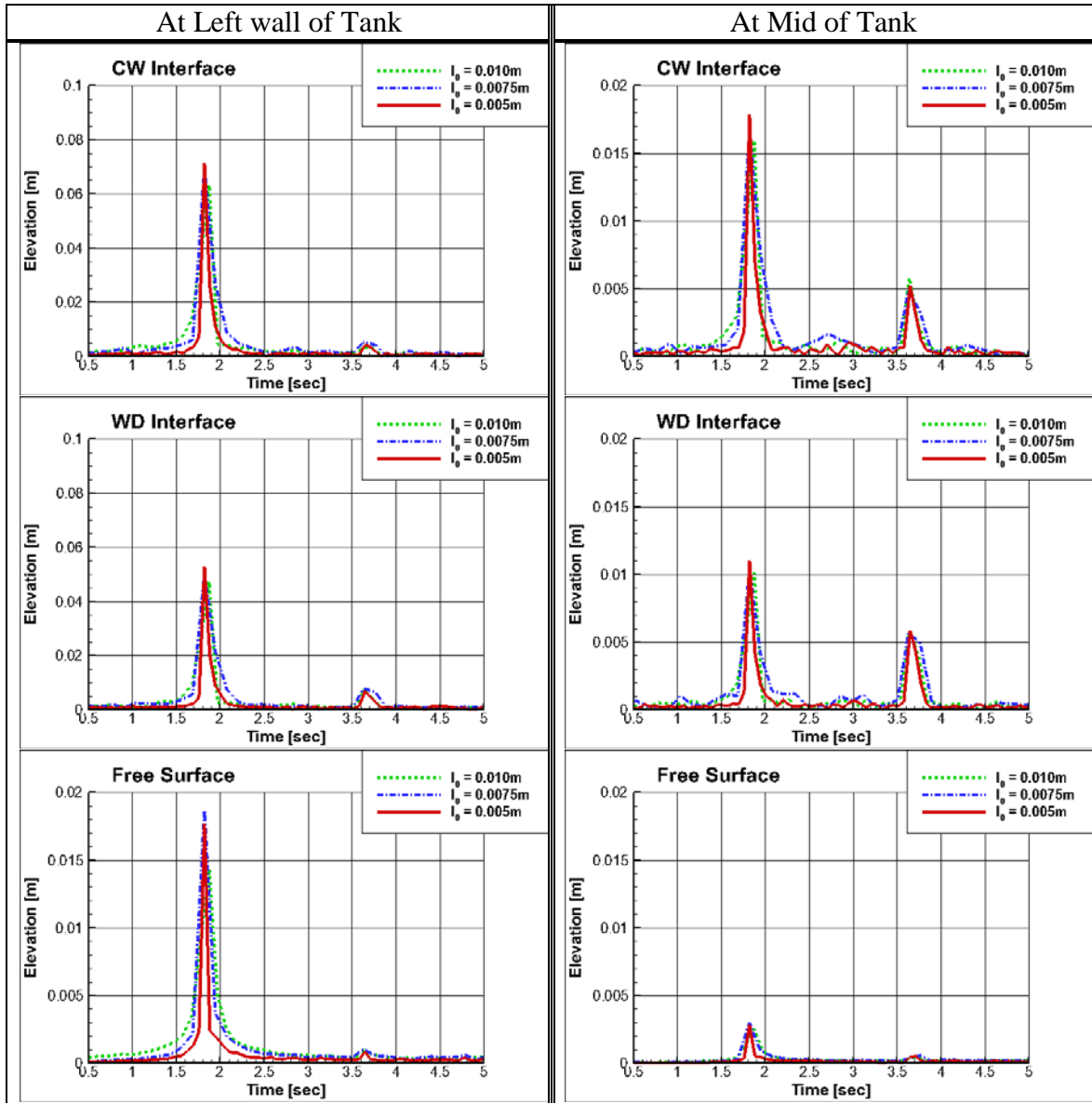


Figure 33 Comparisons of spectra for convergence test

D. Three-Liquid-Sloshing under Harmonic Oscillation (Violent)

Generally, floating production vessels such as FPSO, FSRU, etc. have limited rotational motion under operation. The values of restrictions are not equal to every vessel; however, the roll motion limitation is generally over 5-degrees. In this regard, a

more violent case is conducted numerically with a combination of translational and rotational motion. In the example case, the tank is forced harmonically by a roll amplitude of 3-degrees at 1.83-rad/s and sway amplitude of 4-cm at 3.62-rad/s. As inner liquid motions become violent due to resonant bi-chromatic internal interfacial motions, the non-linearity can be clearly shown in Fig. 34. The notable point is that wave breakings occurred at mid-layer with no wave breaking at the free surface. As mentioned, 3-degrees of roll angle are not considered severe; however, violent internal motions including wave breaking are observed and it can significantly hamper the effectiveness of separators or wash tanks. In this example, the surface tension effects are also studied. Fig. 34 is snapshots of the inner fluid motion without surface tension. Although the fluids are immiscible, both wave breaking and splash are observed. Fig. 35 shows snapshots of the inner fluid motion with surface tension. Because the surface tension reduces fluctuation of interfaces, splash was rarely observed while the over-turning exists.

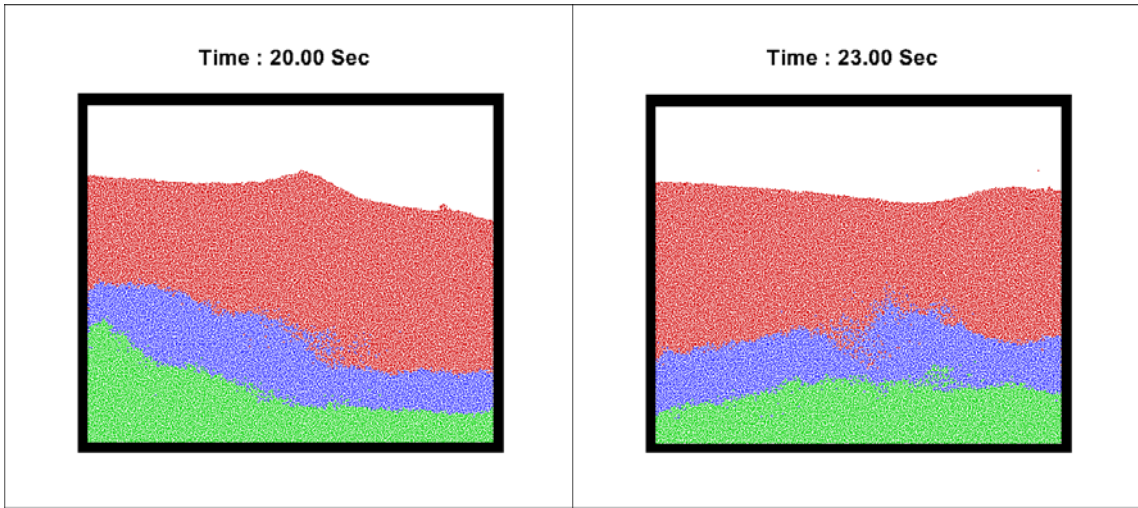


Figure 34 Snapshots of violent motion without surface tension model

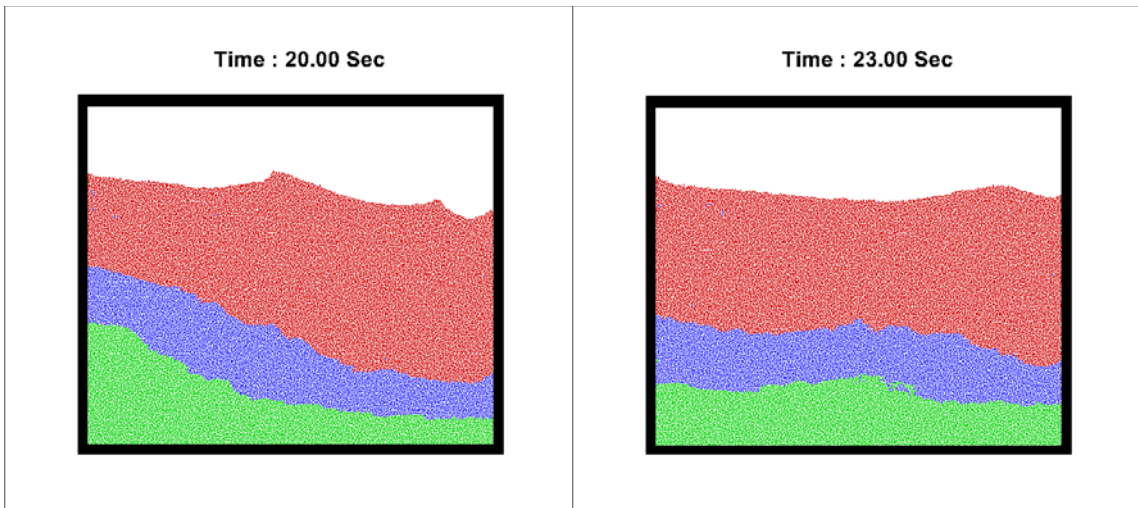


Figure 35 Snapshots of violent motion with surface tension model

2.5 Kelvin-Helmholtz Instability at Interface

Generally, the Navier-Stoke's equation without viscosity is satisfied by the potential flow; although the viscous term is identically zero when the vorticity is zero,

the viscous stresses are not zero (Joshep and Liao, 1994). Barnea and Taitel (1993) theoretically studied the criteria of Kelvin-Helmholtz instability. This instability causes short waves at interface due to shear stresses; when the surface tension and viscosity are neglected, the instability is catastrophic. The importance of surface tension at interface is expiscated by Funada and Joshep (2001) who claimed the growth of short wave, which is induced by Kelvin-Helmholtz instability, is limited by the growth rate. They showed that viscosity will not cause the small waves to decay, unlike surface tension. The general criteria of instability can be expressed as follows:

$$V^2 = (-V)^2 > V_c^2 \quad (5.11)$$

where V is relative velocity between two different fluids at interface, V_c is neutral curve. In this case, the neutral curve, V_c can be obtained by

$$V_c^2 = \min_{k \geq 0} (V^2(k)) \equiv V^2(k_c) \quad (5.12)$$

where k is wave number and k_c is wave number when $V^2(k)$ has minimum value. As already mentioned V^2 is relative velocity and it can be calculated theoretically with function of k as below in case of two-liquids sloshing (Funada and Joseph, 2001):

$$V^2(k) = \frac{[\mu_a \coth(kh_a) + \mu_b \coth(kh_b)]^2}{\rho_a \mu_b^2 \coth(kh_a) \coth^2(kh_b) + \rho_b \mu_a^2 \coth(kh_b) \coth^2(kh_a)} \times \frac{1}{k} [(\rho_a - \rho_b)g + \sigma k^2] \quad (5.13)$$

where μ is viscosity of fluid, h is fluid depth, σ is surface tension. The schematic model for the above equation is shown in Fig. 36.

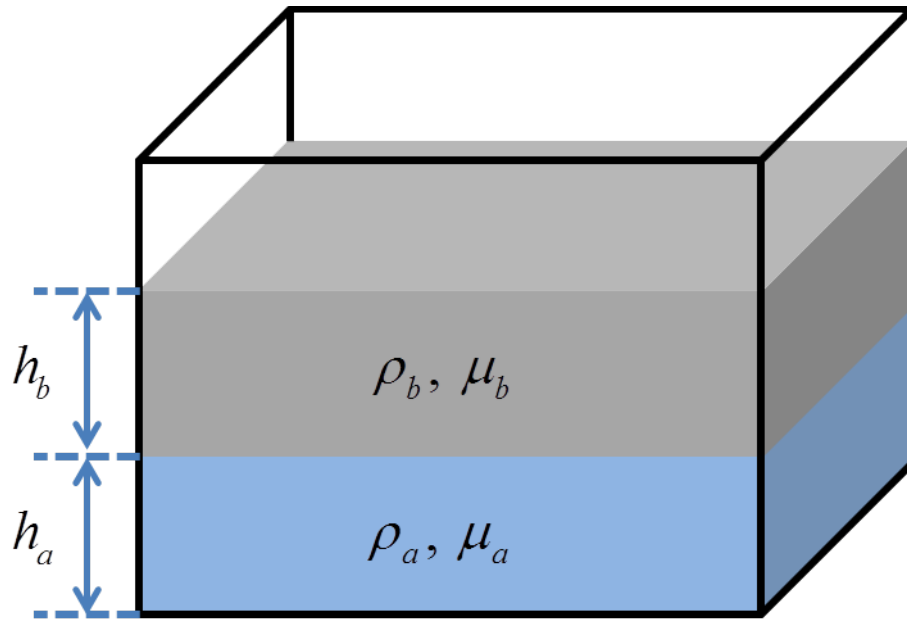


Figure 36 Schematic model for Kelvin-Helmholtz Instability

By using Eq. (5.13), the relative velocities at CW and WD interfaces can be theoretically calculated at each mode of sloshing shown in Tables 5 and 6. According to the definition of the neutral curve, it should be less than relative velocity at the second mode because the sloshing tank is forced to roll with 1-degree amplitude at 1.83-rad/s. This is frequency close to the first mode of the WC interface and the second mode of Cyclohexane. Since the sloshing tank is forced at 1.83-rad/s which is lower than both first mode of the Cyclohexane and Dichloromethane, the relative velocity of the CW and WD interface is larger than assumed neutral curve. As the result, Kelvin-Helmholtz instability should be observed at the CW and WD interface. Fig. 38 is the snapshot of simulation by MPS for the multi-liquid system; the expected short waves are generated as well as those in experiments shown in Fig. 37. In the real sea state, the sloshing

modes induced by irregular waves are higher than the present simulation, the Kelvin-Helmholtz instability should be considered.

Table 5 Table of Wavenumbers and Relative Velocities for CW Interface

Mode No.	Wavenumber	Relative Velocity
1	2.908881481	9.38E-08
2	5.817762963	2.74269E-08
3	11.63552593	1.02777E-08
4	23.27105185	4.90982E-09

Table 6 Table of Wavenumbers and Relative Velocities for WD Interface

Mode No.	Wavenumber	Relative Velocity
1	2.908881481	1.4389E-07
2	5.817762963	5.43219E-08
3	11.63552593	2.58606E-08
4	23.27105185	1.30385E-08



Figure 37 Example of Kelvin-Helmholtz Instability

(Source: "Experimental and Numerical Study of Liquid Sloshing in a Rectangular Tank with Three Fluid," Proc. Of 22nd Int. Offshore and Polar Eng. Conf., Rhodes, Greece, ISOPE, 2012)

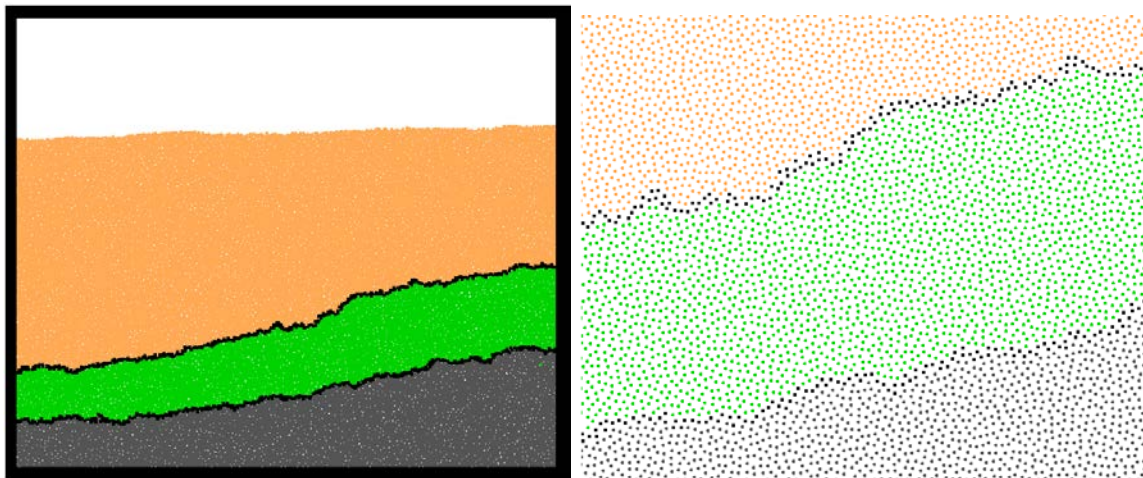


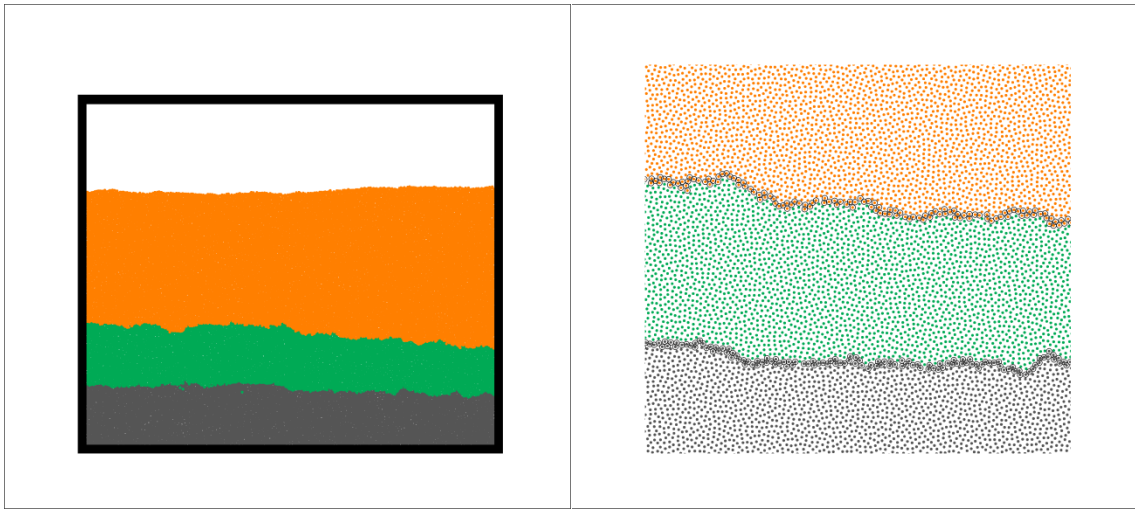
Figure 38 Example of Kelvin-Helmholtz Instability (a) full view (b) enlarged view

According to the description of Kelvin-Helmholtz instability, the surface tension reduces growth of short wave. In order to see the effects of multi-liquid models, the cases given in Table 7 are simulated and their snapshots at the same time were compared. Through this comparison, it can be seen which factor is the most important and the multi-liquid MPS follows the physics. Figs. 39 ~ 45 represent the snapshots of each case. Case I, II, and IV have relatively smoothed interface layer than others which do not have surface tension. In the comparison between Case III and case IV, it shows that surface tension can reduce fluctuation of interface while viscosity does not. Through comparison of snapshots, both viscosity and surface tension are important and the importance of surface tension in limiting the growth of Kelvin-Helmholtz instability is confirmed.

Table 7 Test Cases for Kelvin-Helmholtz Instability

O: Applied / X: Not Applied

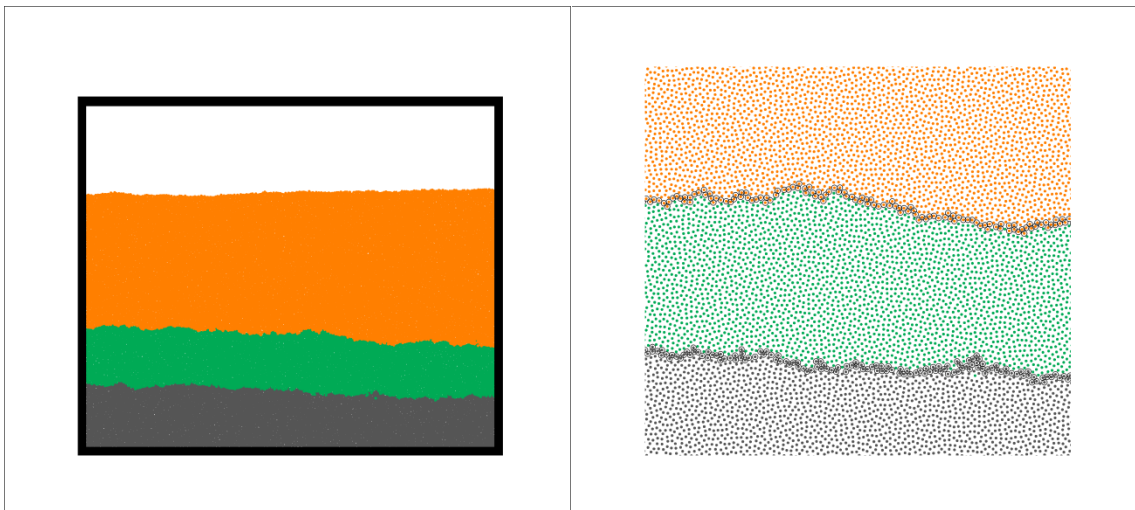
Case	Buoyancy	Surface Tension	Viscosity	Boundary condition
I	O	O	O	O
II	X	O	O	O
III	O	X	O	O
IV	O	O	X	O
V	X	X	O	O
VI	X	X	X	O
VII	X	X	X	X



(a)

(b)

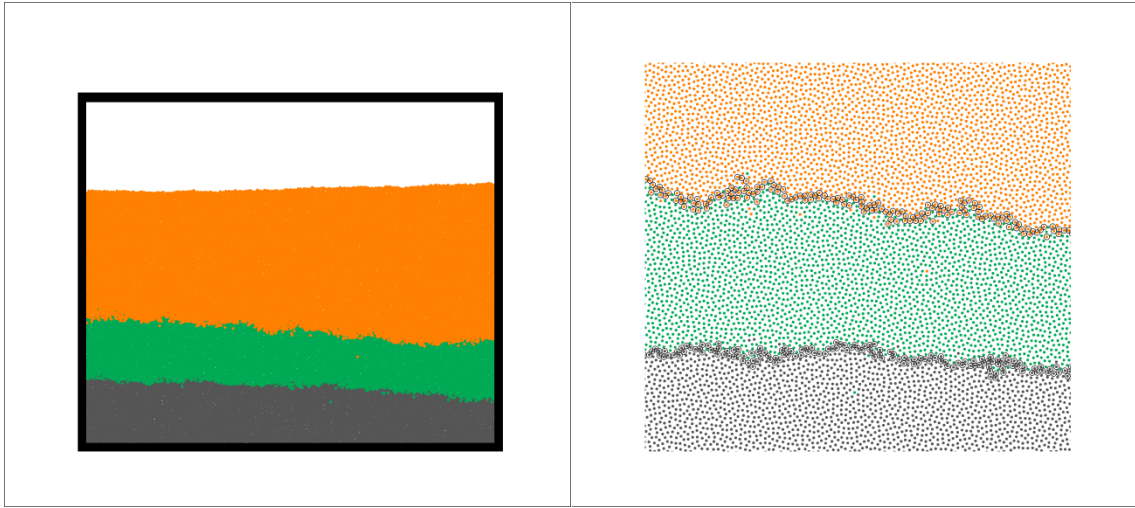
Figure 39 Snapshots of Case I at time 17.5 sec (a) entire and (b) magnified



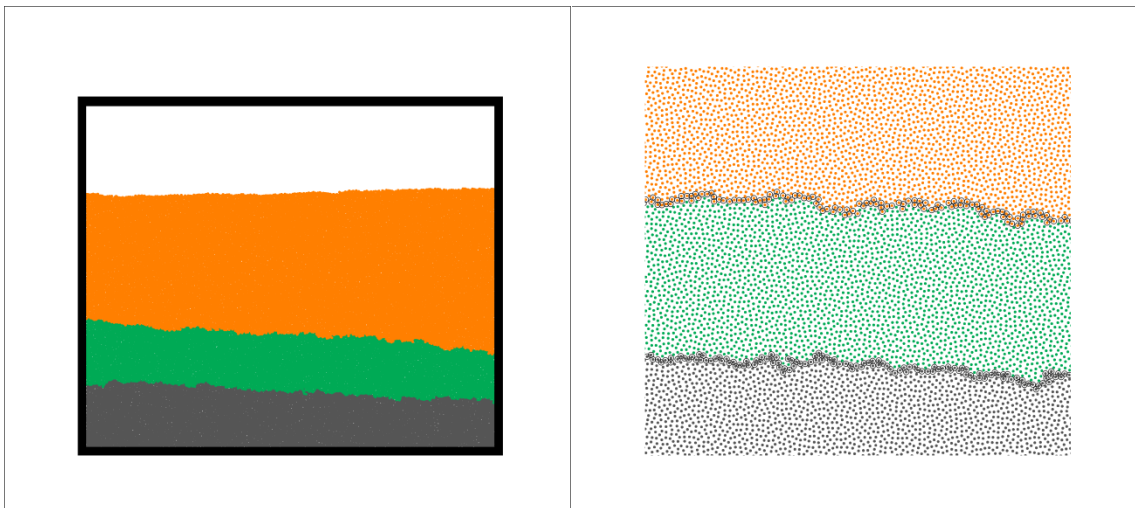
(a)

(b)

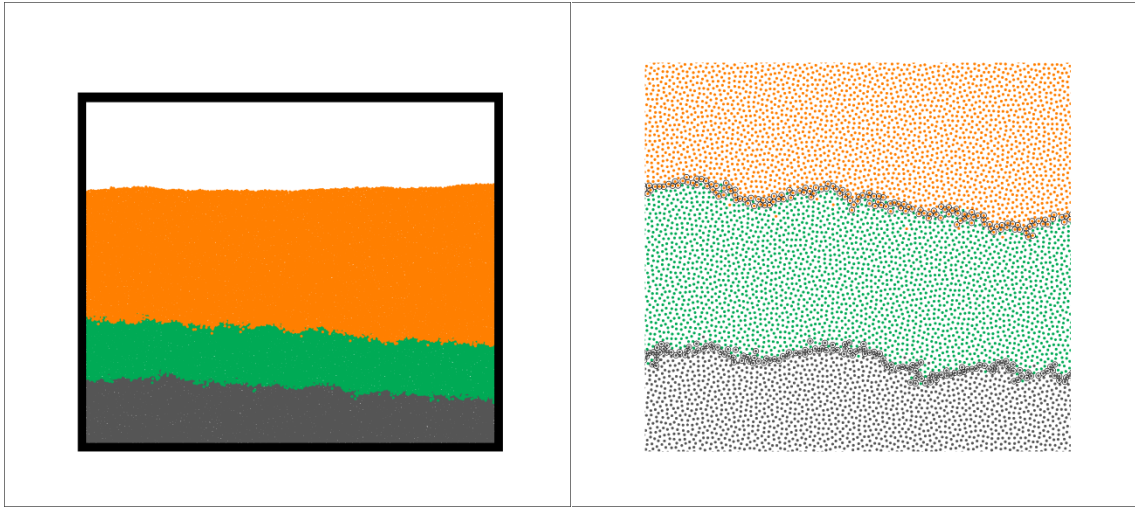
Figure 40 Snapshots of Case II at time 17.5 sec (a) entire and (b) magnified



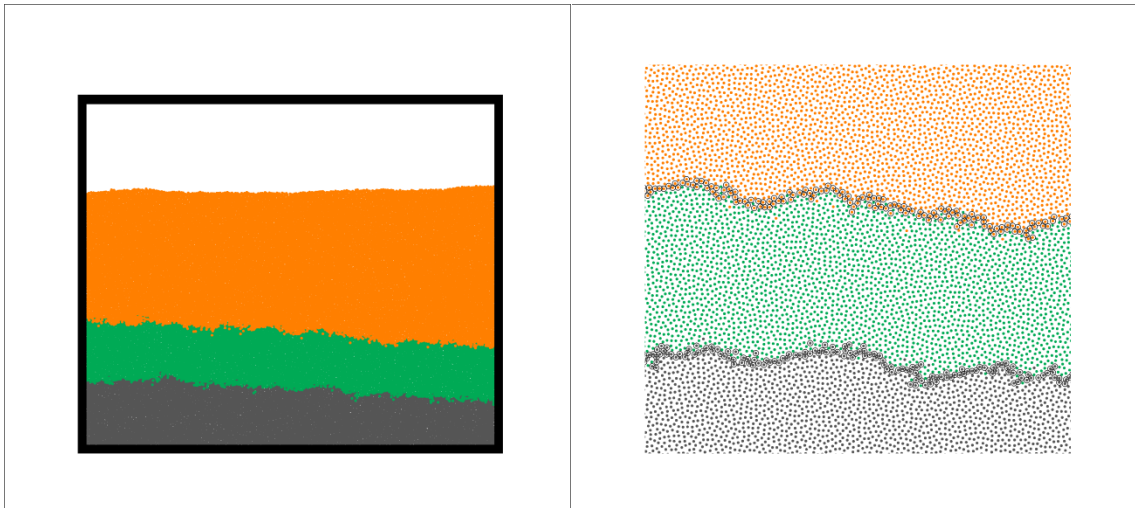
(a) (b)
Figure 41 Snapshots of Case III at time 17.5 sec (a) entire and (b) magnified



(a) (b)
Figure 42 Snapshots of Case IV at time 17.5 sec (a) entire and (b) magnified



(a) (b)
Figure 43 Snapshots of Case V at time 17.5 sec (a) entire and (b) magnified



(a) (b)
Figure 44 Snapshots of Case VI at time 17.5 sec (a) entire and (b) magnified

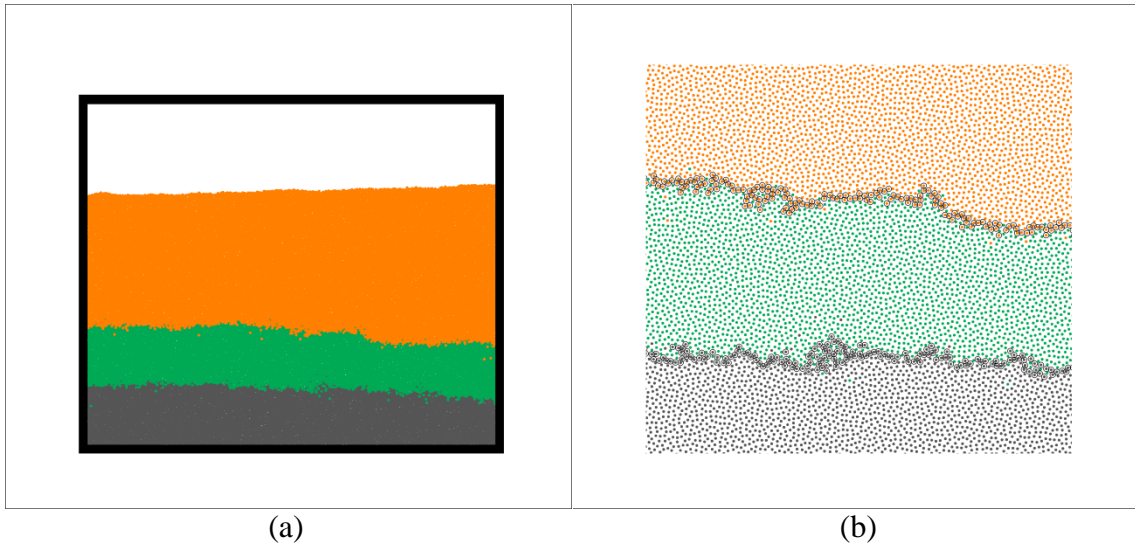


Figure 45 Snapshots of Case VII at time 17.5 sec (a) entire and (b) magnified

2.6 Interface of High Density Contrast

Lee et al (2011) has investigated the sloshing with floaters which can reduce the impact loads induced by the sloshing. In this paper, PNU-MPS, which is improved by Lee et al (2011), claimed that the simulation cannot be executed when the density contrast is less than 0.1 due to sudden change of physical quantities. The present improved MPS includes the Hydrostatic Correction model which applies weight of the free surface particle to correct the hydrostatic pressure. Its collateral advantage is that the sudden change of the physical quantities also can be reduced. The case of sloshing with floaters as shown in Fig. 46 can be reproduced by present MPS and the measured pressure are compared with variety density contrast. A total 4,116 particles are used including 2,880 for water and 364 for wall particles. Figs. 47~49 show the pressure comparison between PNU-MPS and present MPS. In case of the ratio is 0.3 shows good agreement between two programs. In case of the ratio is 0.1, PNU-MPS has irregular

pressure peak at 5 sec which cannot be shown in present MPS. Furthermore, when the density contrast becomes less than 0.1, the PNU-MPS blow out simulation due to infinite pressure, while present MPS can simulate the case of density contrast as 0.05 as shown in Fig. 49.

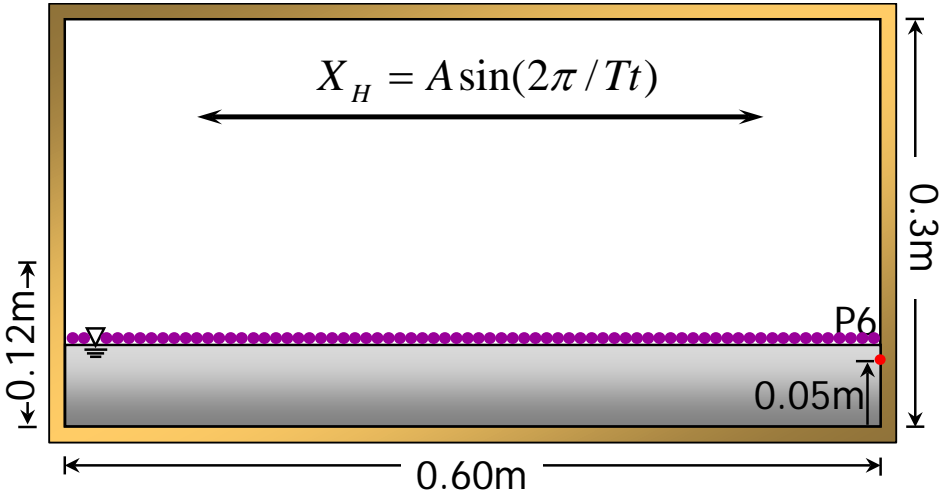


Figure 46 Schematic model for sloshing with floater

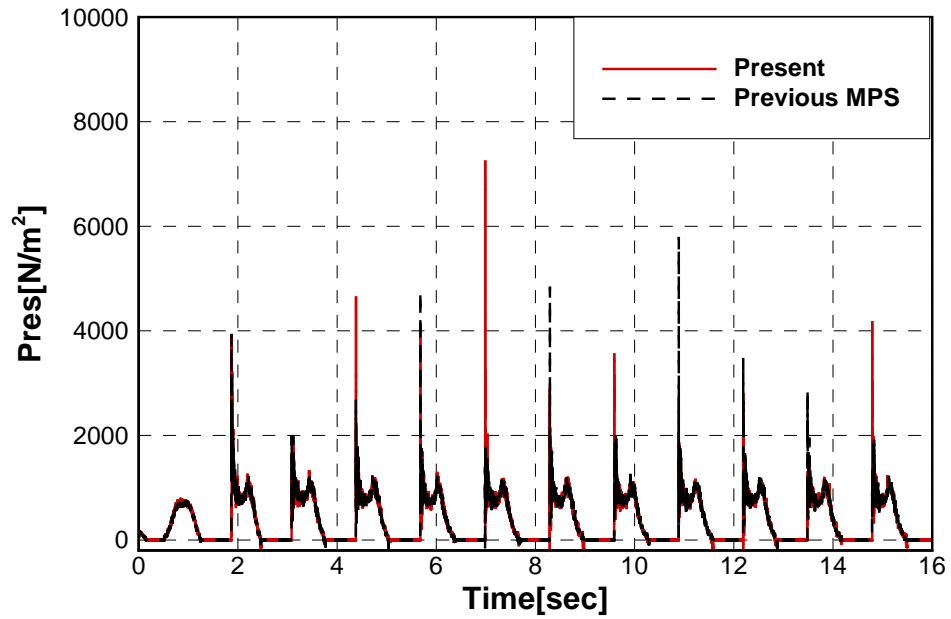


Figure 47 Pressure history at density contrast (1000:300)

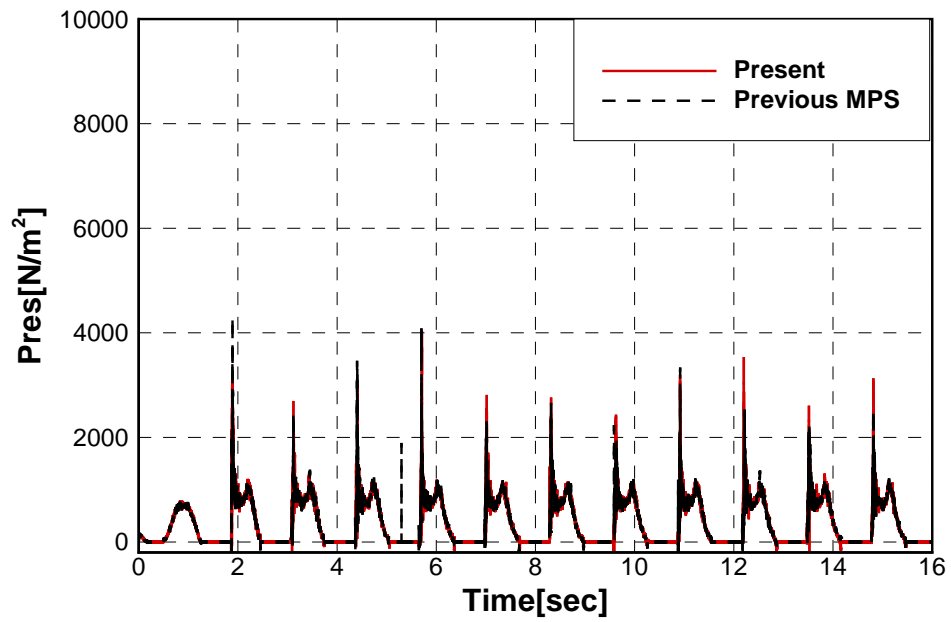


Figure 48 Pressure history at density contrast (1000:100)

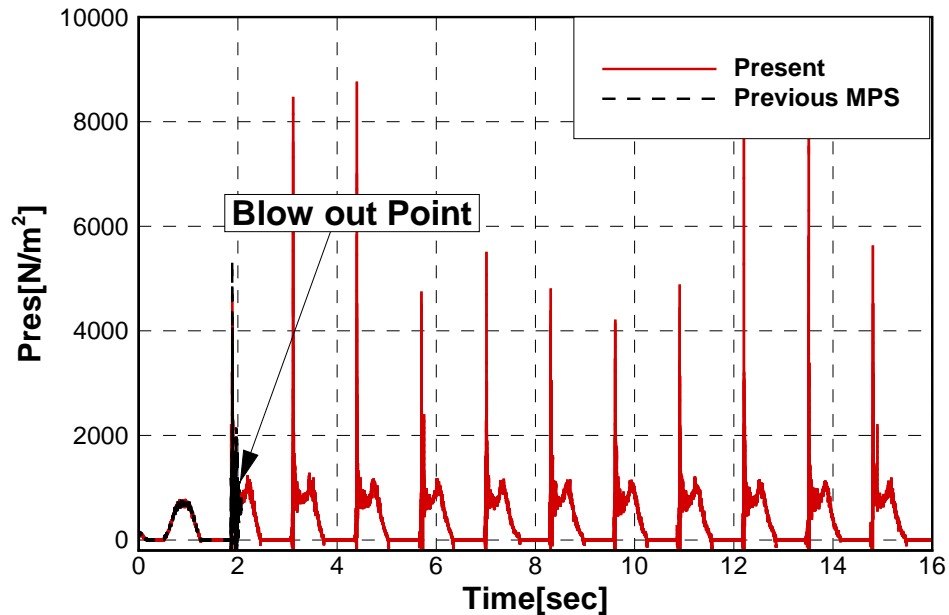


Figure 49 Pressure history at density contrast (1000:50)

3. Vessel-Sloshing Interaction Simulation

3.1 Single-Liquid Vessel-Sloshing Interaction

A. Coupling with Vessel Motion and Sloshing Effect

This section will discuss the coupling between vessel motion and single-liquid sloshing tanks. The simulation conditions are given in Table 8. In order to investigate the dynamic coupling effects between vessel and sloshing motions due to waves at different filling levels of the sloshing tank and winds and currents are not considered in the present simulations. The considered wave heading is the beam-sea condition because under this condition it can be assumed that the liquid sloshing motion is uniform in the longitudinal direction, and that the 2-dimensional sloshing program can be used for a more time-effective simulation. Significant wave height, peak period, and enhancement

parameter of γ of a JONSWAP spectrum were selected as shown in 8. The model for simulation is adopted from experiments by MARIN as a part of SALT-JIP. In this experiment, a barge-type FPSO has two rectangular tanks filled with fresh water with a variety filling level. The filling levels used in the experiments are 18%, 37% and 56% of tank height. In the numerical simulation, all conditions are the same as the experiments.

Table 8 Circumstance Conditions

Wind	N/A	
Current	N/A	
Wave	Heading	90 Degree (beam)
	Significant Height	5.0 m
	Peak period	12 sec
	γ of JONSWAP spectrum	3.3
Filling Level	18%, 37%, 56%	

Table 9 Characteristics of Sloshing Tanks.

Designation	Magnitude	
	AFT TANK	FORWARD TANK
Tank aft from aft perpendicular	61.08 m	209.54 m
Tank bottom from keel line	3.3 m	3.3 m
Tank length	49.68 m	56.616 m
Tank breadth	46.92 m	46.92 m
Tank height	32.23 m	32.23 m

Table 10 Principal Particulars of FPSO (bare hull) and Mooring System.

Description		Magnitude
Length Between Perpendicular		285.0 m
Breadth		63.0 m
Draught		13.0 m
VCG (From the Keel)		16.71 m
Mass radius of gyration around X-axis		19.49 m
Mass radius of gyration around Y-axis		78.42 m
Mass radius of gyration around Z-axis		71.25 m
Mooring Stiffness		
	Surge	$6.50 \times 10^5 N / m$
	Sway	$2.43 \times 10^6 N / m$
	Yaw	$1.76 \times 10^8 Nm / rad$

In the numerical simulation, the hydrodynamic coefficients and linear/drift wave forces can be obtained by using a 3-dimensional panel-based diffraction/radiation program, WMAIT (Lee, 1995). The panels are generated as shown in Fig. 50 (b). The total number of panels for this barge-type FPSO hull is 2,375. The schematic model of the vessel with two tanks is shown in Fig. 50 (a) and the specifications for the liquid tanks are summarized in Table 9. The principal particulars of the vessel and mooring system are given in Table 10. In both the experiment and the numerical simulation, the barge type FPSO with external mooring stiffness is modeled by linear springs for surge, sway and yaw modes.

First, the case of ship motions without liquid tanks is considered. This simpler case has to be validated against experiments before considering the more complicated interaction between ship-motion and liquid-sloshing-effect problems. The infinite water depth condition, which is wave length less than double its amplitude, is used. By the numerical simulation, the obtained vessel motions are converted to the RAOs (Response Amplitude Operator); they are then compared with RAOs from experiments shown in Fig. 51. Both the RAOs predicted in both frequency- and time-domains have good agreements compared with the experiment except for roll. Because the frequency of roll motion is close to the natural frequency, the RAO of roll is over-predicted in the frequency-domain calculation. In the time-domain simulations, the hull viscous drag forces provided additional roll damping for better correlation against the experimental results near the roll natural frequency. Morrison's equation with equivalent viscous plates was used to estimate hull viscous drag forces. Since both the sloshing dynamics and vessel motions with dry tanks are independently verified against the respective experimental results, their coupled dynamics combined in the time-domain simulations can be considered.

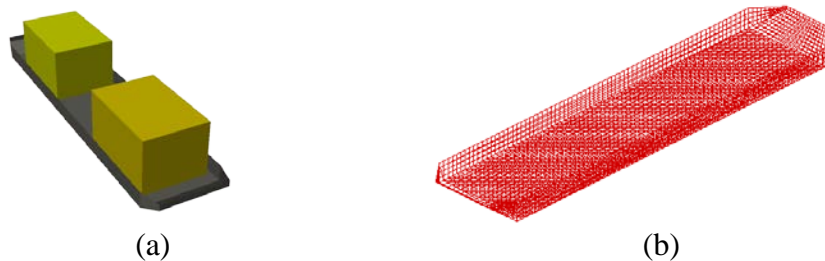


Figure 50 : (a) Model of MARIN-FPSO with sloshing tanks (b) model for panel method

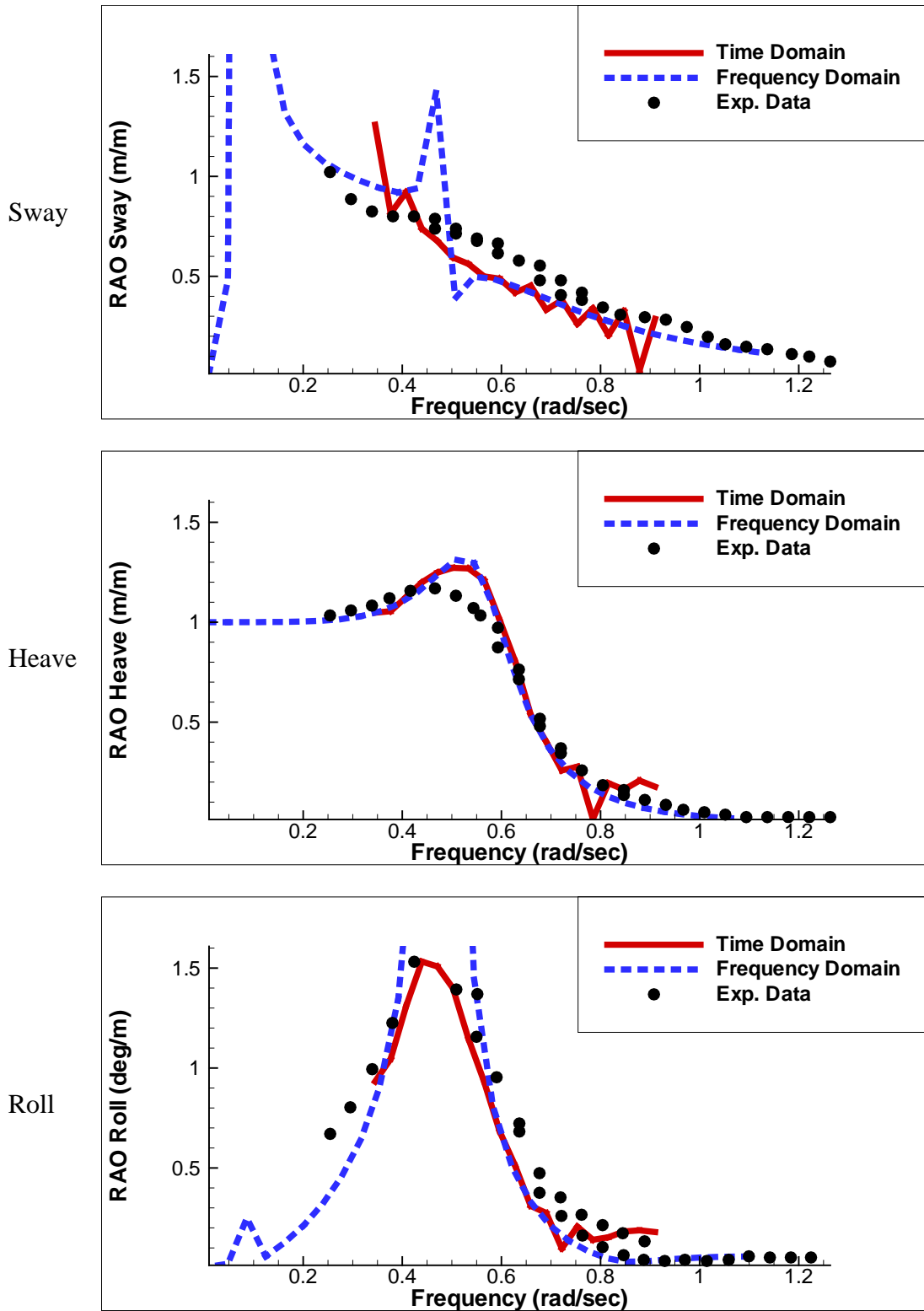


Figure 51 Comparisons of simulated and measured RAOs without inner liquids

After validation of the ship motion program and sloshing program, the two programs are ready to be coupled. Before coupling, however, the numerical sensitivity and reliability for each program should be achieved. Typically, the CFD program, the MPS in the present study, has a much smaller time step than that used for the ship-motion simulation. It is important to find the appropriate time interval of simulation to save calculation time. In this regard, the ship-motion time interval may be larger than the MPS time step. Nevertheless the ship motion program may have a large calculation time step; the coupling time interval also should be considered because when the sloshing motion is violent, the impact loads on the tank wall can occur in a very short time and can cause non-trivial transient effects. If the coupling time step is too large, it cannot capture the sloshing impact loading. In this regard, through convergence test with varying coupling time steps, the time interval for coupling is set as 0.02sec. Since the time interval for coupling is 0.02sec, whatever the time step of MPS (here time step for MPS is 0.005sec), the sloshing effects are fed to the ship motion program at every time step. Accordingly, the ship motion program should wait until the sloshing simulation program reaches feedback time. In the case of the liquid sloshing motions, nonlinearity and breaking are involved and the sloshing induced by impact loads and the resulting vessel responses may depend on the simulation time length. Correspondingly, the sensitivity was checked by varying the simulation time from 1000s to 2500s. It is seen that the differences between them are within 4% after 1500s. For the ensuing results, the simulation-time length is 1800s, which is about the same as that of the experiment for fair comparison. In the beginning of the ship-motion simulation, the environmental

loading is gradually applied from zero to the actual value within the ramping period (200s) to suppress the transient responses as much as possible in subsequent times. The response data during the ramping period is not used for the RAO calculations. Fig. 52 represents snapshots of 18% filled inner sloshing tank at arbitrary moments. Fig. 53 shows RAOs of vessel in sway and roll motions with various filled inner liquid tank.

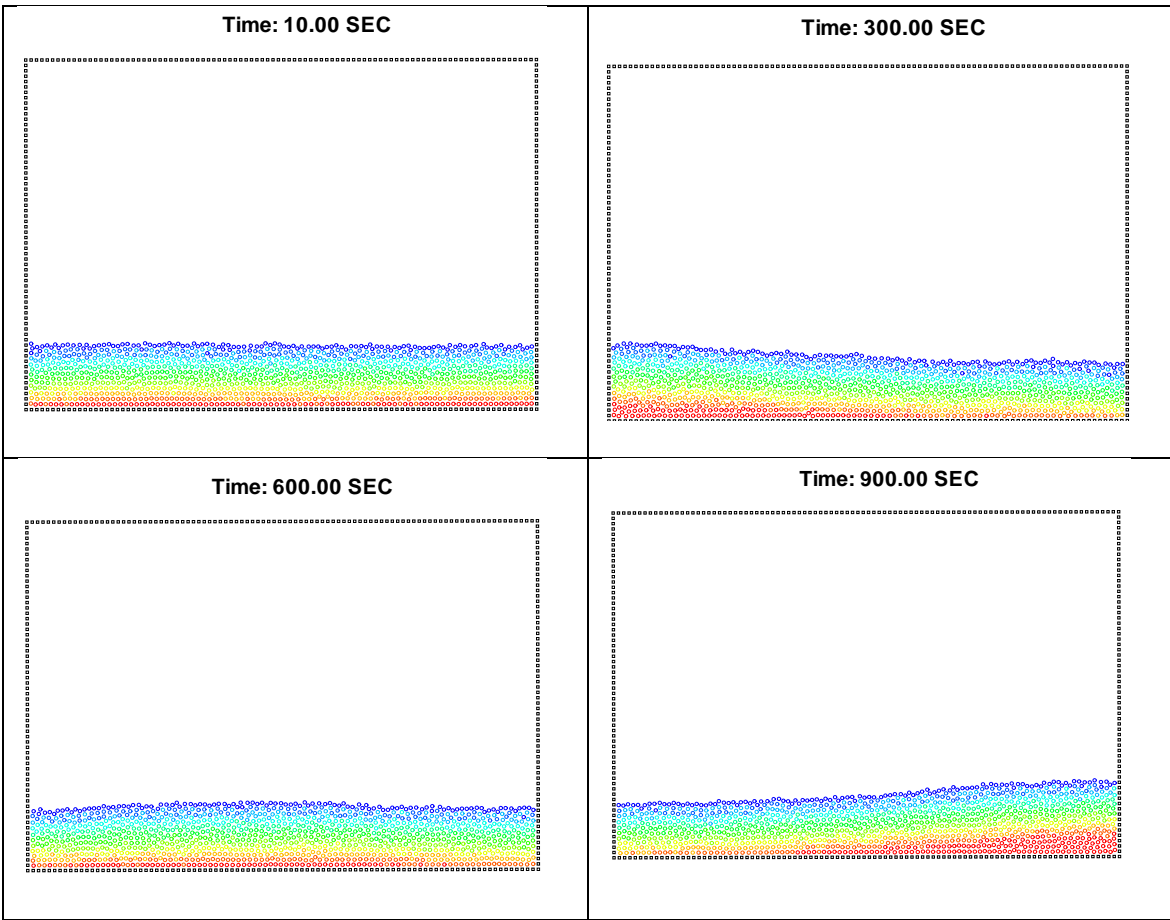


Figure 52 Snapshots of liquid motions and pressure field inside an 18% filled tank

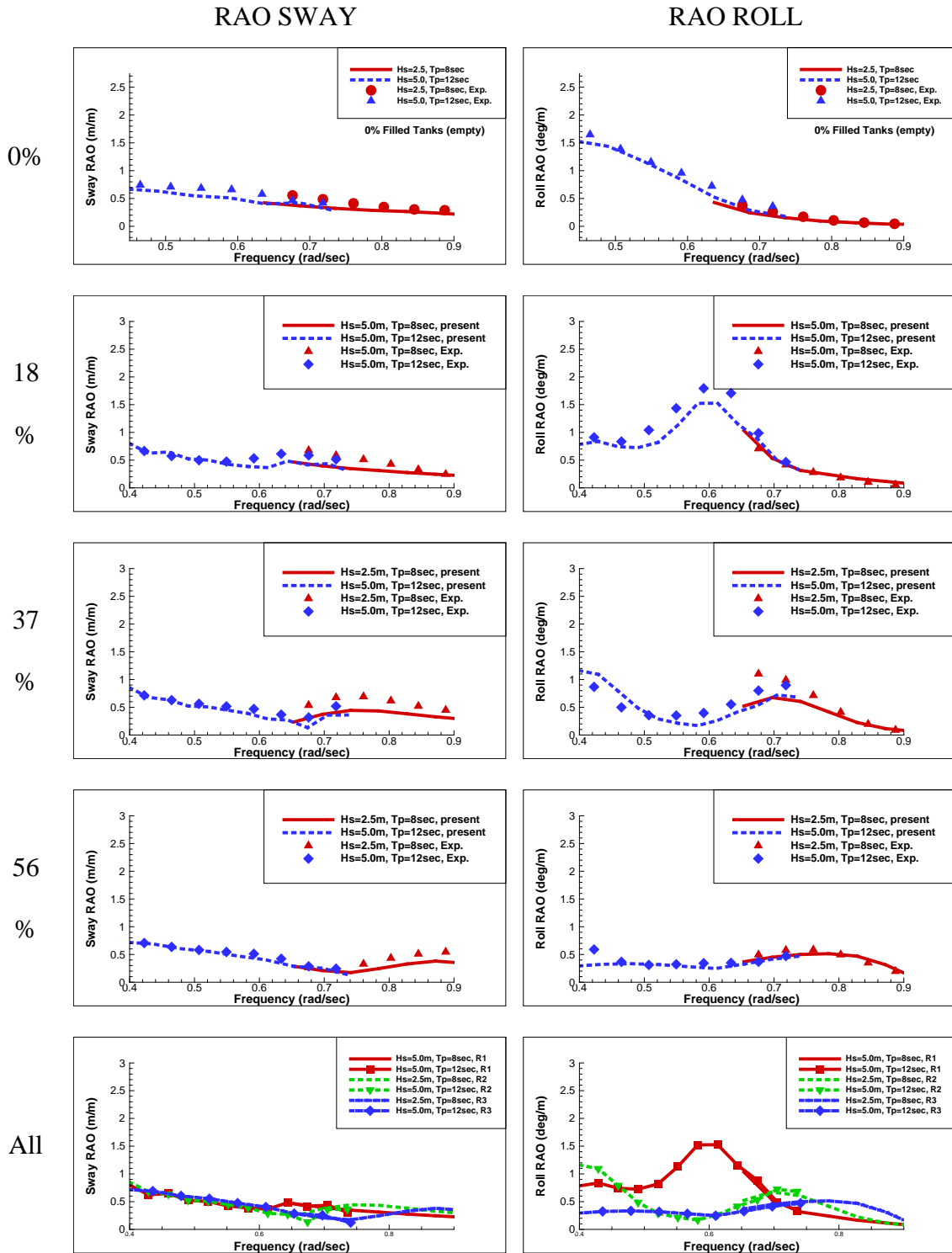


Figure 53 comparisons of simulated and measured RAOs of MARIN-FPSO with various filling ratios

The roll motions are very sensitive to the total weight of the liquid cargo and motions of inner liquid. Through comparisons among different filling ratios of the inner liquid tanks, it is seen that amplitudes of RAOs can be increased by a factor of 2 or 3 in the same wave frequency range under the same circumstances compared with the case of the bare-hull. It shows that the motion-sloshing coupling effects are significantly important. The existence of the liquid cargo can affect not only the magnitude of the amplitude, but also its resonant frequencies. For example, the bare-hull roll natural frequency is 0.49rad/s, while the hull with a 37% fill ratio has two natural frequencies, 0.4rad/s and 0.72rad/s. This effect is clearly illustrated in the given simulation results. As a reference, the two lowest natural frequencies of liquid sloshing motions for various fill ratios are given in Table 11. The analytic results can be obtained using the linear potential theory.

Table 11 Natural frequencies of FPSO and Sloshing Tanks.

		Transverse Mode	
		Roll: 0.50	
Bare Hull		1 st	2 nd
Sloshing Tanks	FL: 18%	0.49	1.31
	FL: 37%	0.66	1.55
	FL: 56%	0.74	1.61

Next, the steepness of incident waves on the vessel was investigated since steeper waves can enlarge the ship motions; subsequently, the sloshing motions can be more violent and have non-linearity. For this purpose, the cases of 18% and 56% filled inner liquid tanks were selected. The RAOs obtained from these cases are shown in Figs. 54 and 55. As the significant wave height increases, the roll RAOs for the 56% fill ratio are less variant with increasing the significant wave height compared to those of the 18% fill ratio; this is due to the less violent liquid sloshing motions or smaller nonlinearities in the case.

Another factor is the peak period. The lowest sloshing natural frequency (0.49 rad/s) of the 18% case given in Table 11 is closer to the peak frequency (0.52 rad/s) of the input spectrum than that (0.74 rad/s) of the 56% case. Figs. 56 and 57 show representative nonlinear free-surface snapshots for both cases. It is apparent that the liquid sloshing motions become more nonlinear (wave breaking) in the 18% case. Due to the nonlinear free-surface effects, more changes in RAOs are expected with much higher waves.

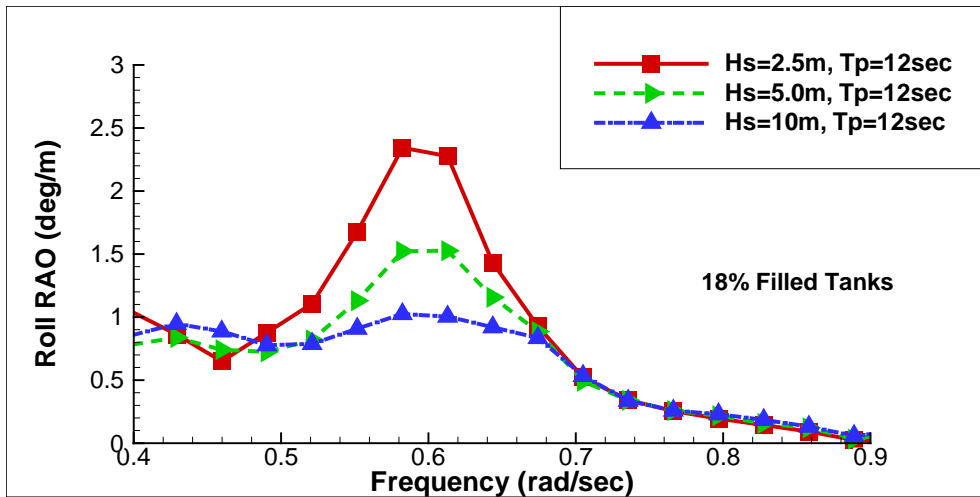


Figure 54 Comparisons of roll RAOs for Hs=2.5m, 5.0m, and 10m (Tp=12s; 0.52 rad/s) for 18% filled tanks

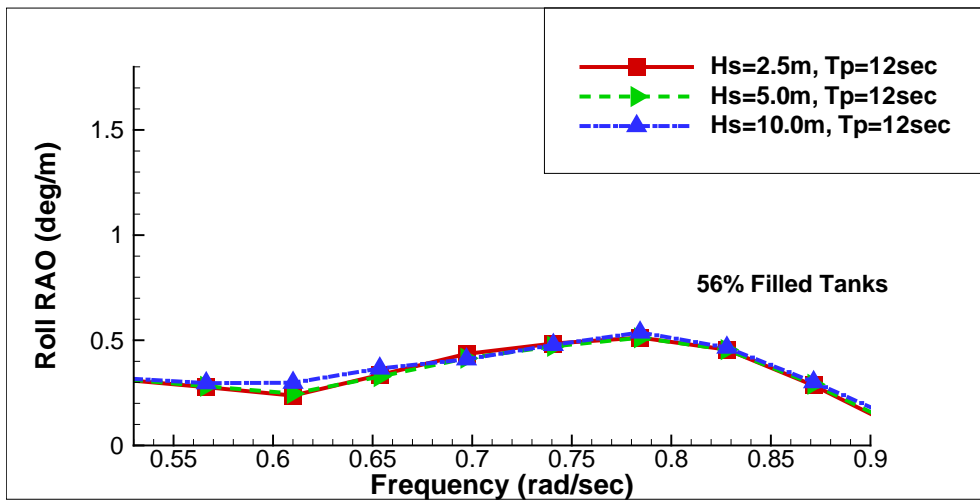


Figure 55 Comparisons of roll RAOs for Hs=2.5m, 5.0m, and 10m (Tp=12s; 0.52 rad/s) for 56% filled tanks

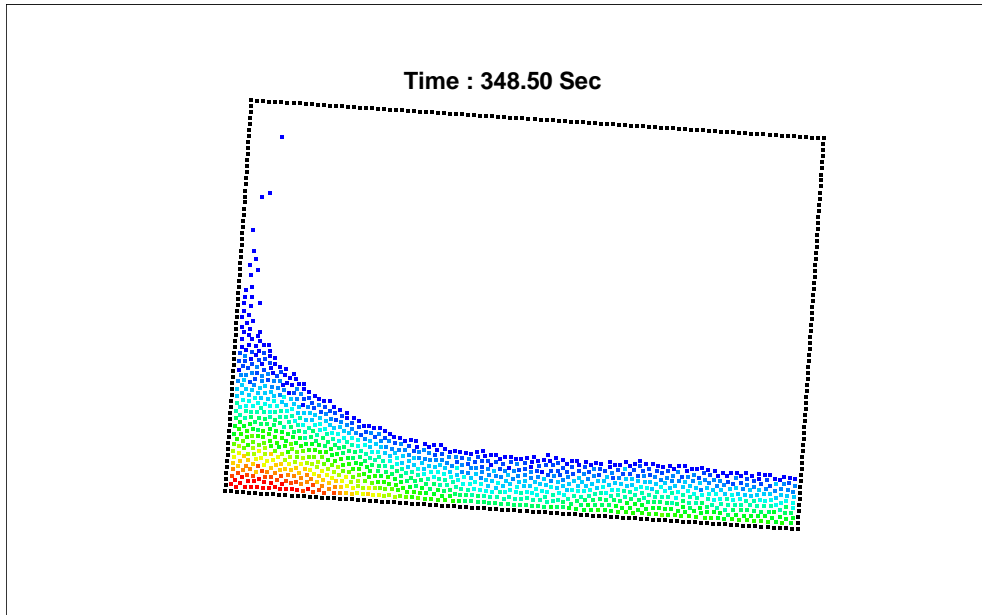


Figure 56 Representative nonlinear snapshots for inner liquid of 18% filled tank with $H_s=5\text{m}$ and $T_p=12\text{s}$.

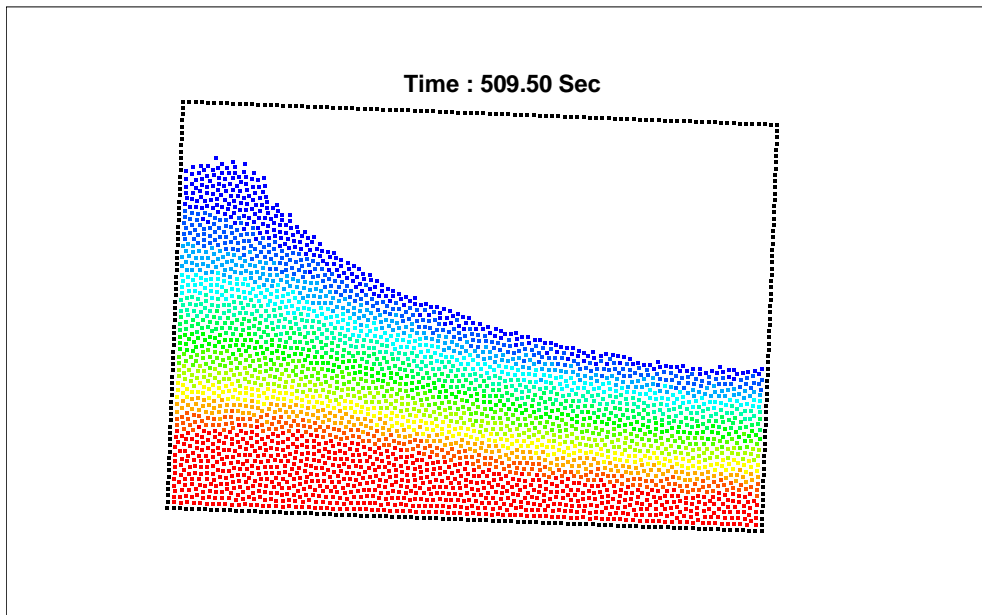


Figure 57 Representative nonlinear snapshots for inner liquid of 56% filled tank with $H_s=5\text{m}$ and $T_p=12\text{s}$.

For the case of the 56% filled liquid tanks, simulation with 8s of the peak period of the input spectrum is performed. This peak period is closer to the lowest natural at 56% filled sloshing tank (0.78-rad/s) which is given in Table 11. Consequently, there is more incident wave energy that can excite resonant sloshing motions inside the liquid tanks. As a result, larger sloshing motions are generated and we can see more nonlinear effects compared to Fig. 58.

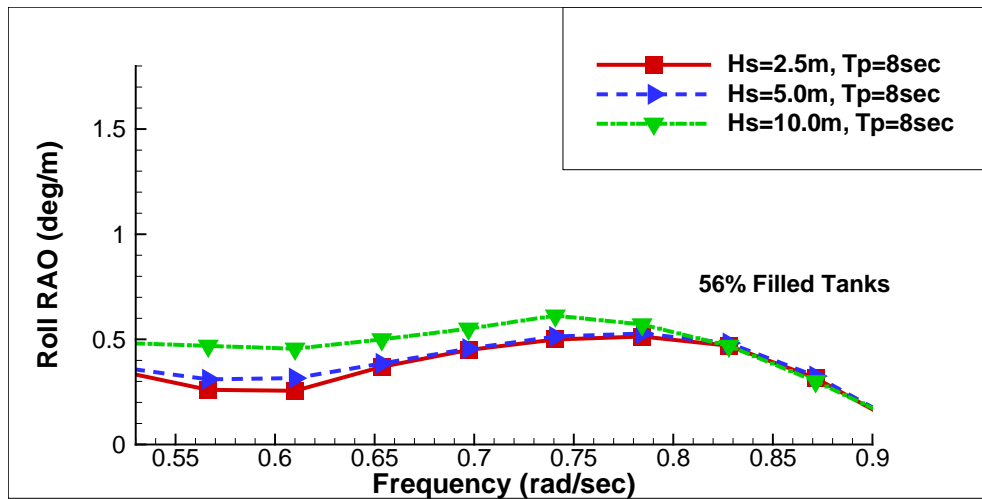


Figure 58 Comparisons of roll RAOs for Hs=2.5m, 5.0m, and 10m (Tp=8s; 0.78 rad/s) for 56% filled tanks

B. Ship Motions with Rigid Cargo in Tanks

The case of rigid cargo, which is the simplest method to couple between ship motion and sloshing, was considered. In this case, the inner liquid is regarded as one rigid block which is connected with the tank wall. This block has the same density as fluid and its surface cannot fluctuate along tank motion due to its solidity. Consequently,

the sloshing effects are neglected and only the total mass is increased by the amount of liquid in the vessel motion analysis. This means that only the inertia forces and moments are fed to the ship motion program while the impact loading induced sloshing is ignored. This is the simplest approximation one can use without more sophisticated coupling programs. Through this simulation and comparison with the case of liquid cargo, the effect of sloshing can be clearly understood. For clearer confirmation of sloshing effects, the cases of 18%, 37% and 56% filled tanks with rigid cargo were conducted. Figs. 59~61 show the comparisons of roll displacement and RAOs for each filling ratio. The interesting point of these comparisons is that all cases of rigid cargo have shifted peak to lower frequency compared to cases of liquid cargo. However, RAOs of other modes had relatively small changes compared to roll. Another interesting point is the magnitude of the RAOs. With rigid cargo, the roll motion was much higher than the liquid one with factor of 2 or 3. It means these rigid cargo sloshing tanks are not passive anti-rolling tanks, while liquid cargo tanks can reduce roll motion. From the above comparisons, it can be concluded that a proper vessel-motion/liquid-sloshing coupled dynamics program needs to be used to accurately predict vessel motions with sloshing effects. In this case, the draft of vessel was kept the same for all fill ratios by ballast/deballast system. Therefore, it is assumed that the center of gravity of vessel remains the same after considering the ballast effect.

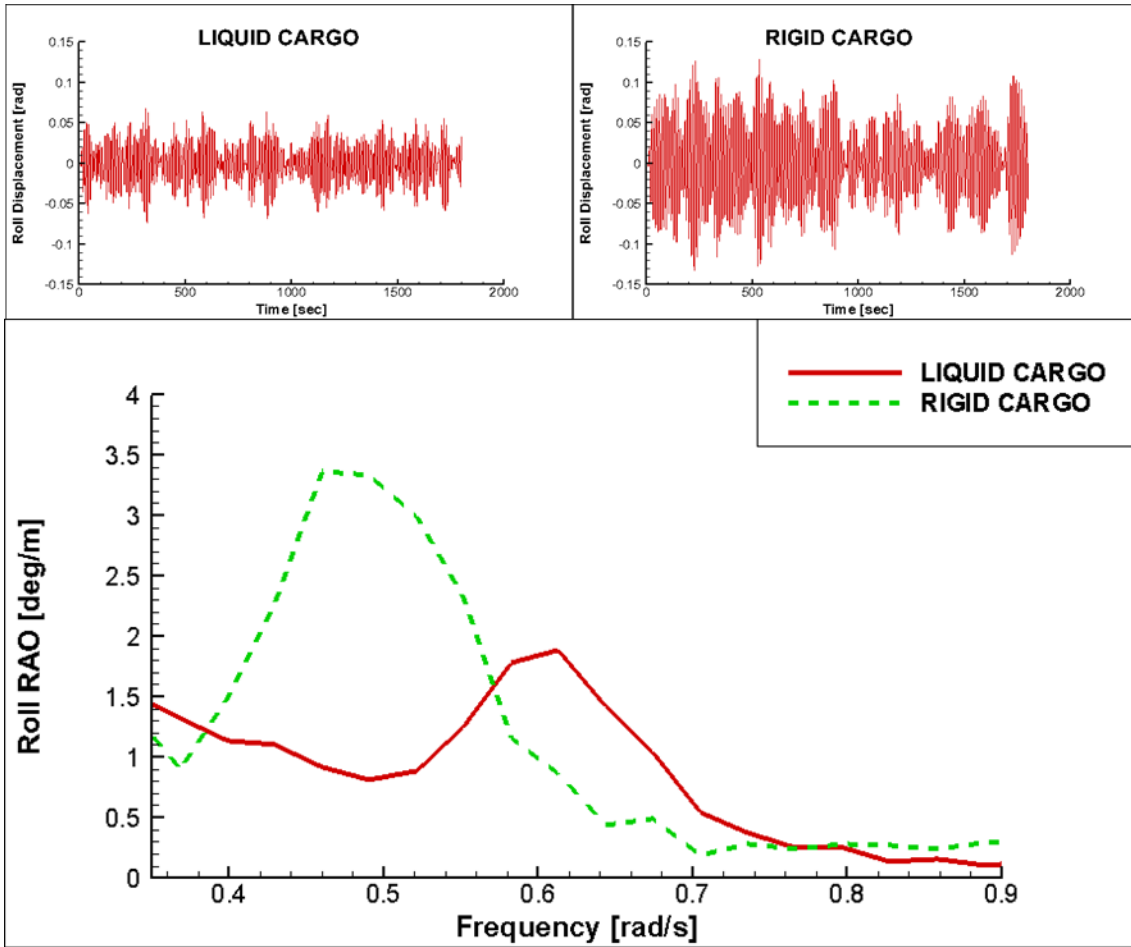


Figure 59 Comparison of displacement and RAO between liquid- and rigid-cargo with 18% filled tanks

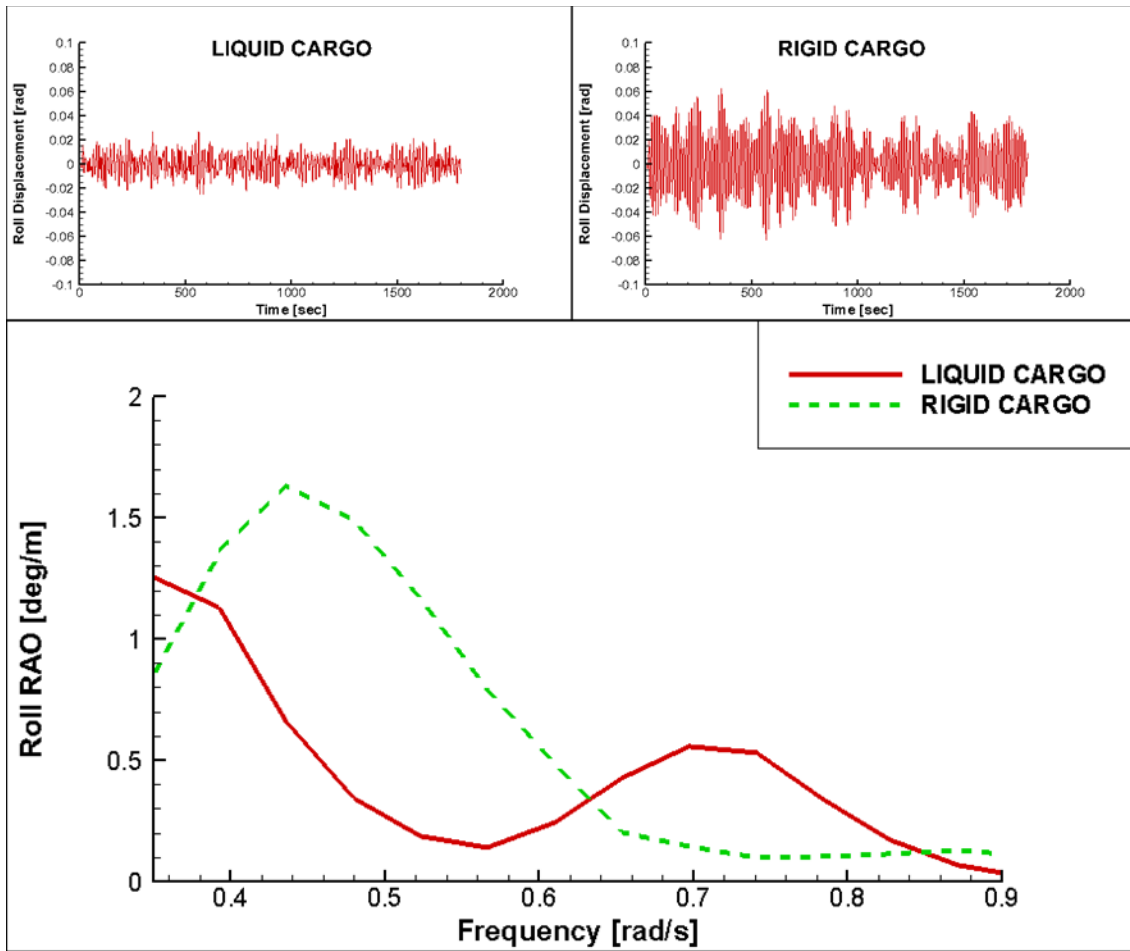


Figure 60 Comparison of displacement and RAO between liquid- and rigid-cargo with 37% filled tanks

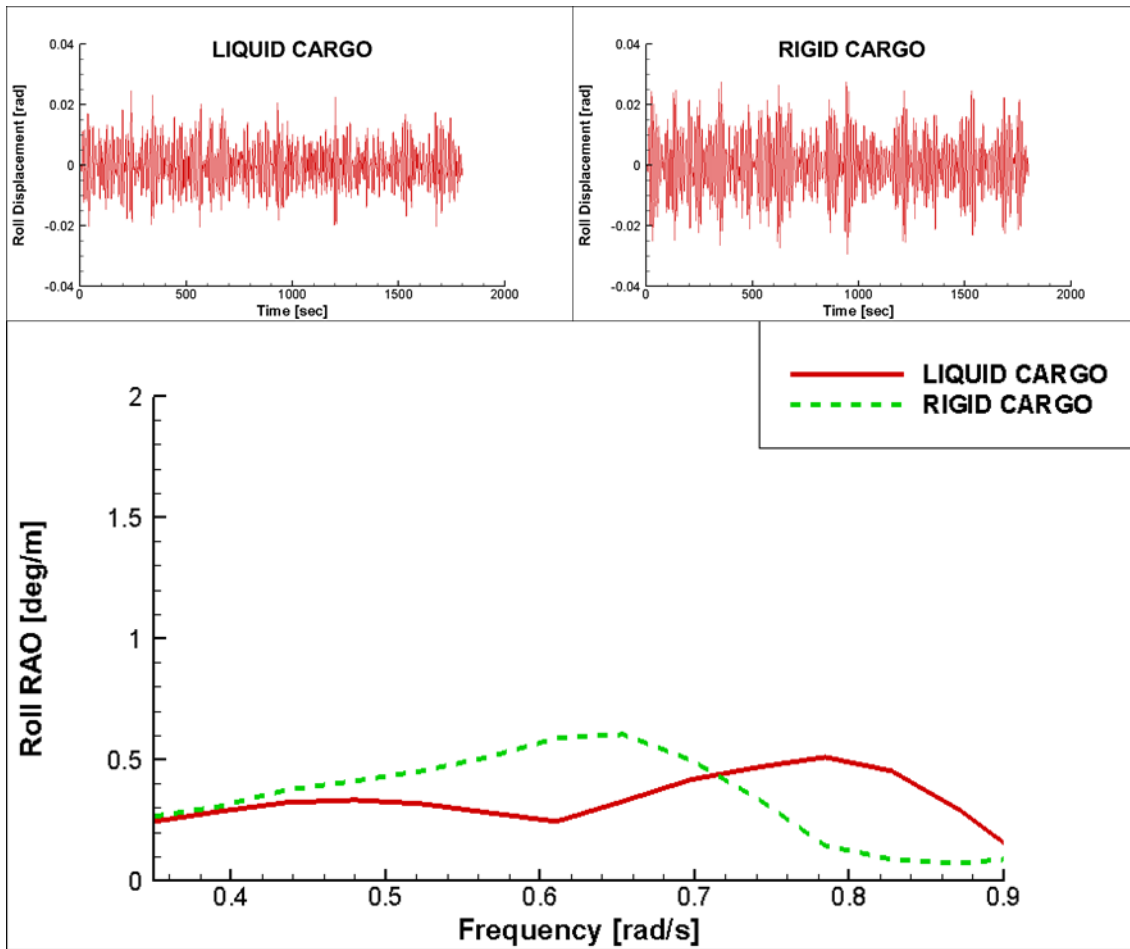


Figure 61 Comparison of displacement and RAO between liquid- and rigid-cargo with 56% filled tanks

3.2 Multi-Liquid Vessel-Sloshing Interaction

Since demand for oil/gas has increased rapidly, offshore oil/gas production has continuously extended to deeper waters. Consequentially, more floating offshore structures having the capability of production and storage are to be manufactured and installed, these include multi-well systems. In this regard, many new ideas have been suggested to increase the efficiency of production/processing for floating platforms. The

wash-tank is one suggestion. The wash-tank is located inside the hull for initial separation of mixed fluids consisting of oil and sea water produced through production risers. In this regard, previously coupled program between ship motions and sloshing effects is revisited to predict vessel motions influenced by the sloshing effect; moreover to anticipate fluid motions inside wash-tank will account for multi-liquid-system.

Before simulation of fully coupled problems, the free-decay test was performed to obtain natural frequencies of the wash tank. Schematic model of wash tank is shown in Fig. 62. For the present MPS simulation, a total of 67,396 particles are used; 19,200 particles for the bottom layer, 4800 for the middle layer, and 40,000 for the top layer. 3,396 particles are used to represent the solid tank wall. The interfaces are tilted by 5-degrees and released to have ensuing free oscillations. All oscillations of each interface were measured at each time step and then the obtained data was converted to the corresponding spectra in the frequency-domain by the Fourier Transform. The reference points are at the left wall of the tank and mid tank. The peaks represent natural frequency of the system as shown in Fig. 63; they are then compared with the theoretical value based on linear potential theory (see Table 12). In this point, although the thickness of each interface is quite different, but some peaks are coincide with other layer's peak due to coupling effects. Especially, the layer of the emulsion has relatively thin thickness compared to others; it has coupled spectra with other layers which are different to own natural frequencies.

The coupling method is used in the same manner as the single-liquid-sloshing/ship-motion coupled program. In order to simulate multi-liquid sloshing

coupled with vessel motions, the sloshing program was replaced with a newly developed MPS for multi-liquid. In the present example, the hull is the same as that used in the single-liquid coupling simulation (see Table 13); all simulation conditions are also the same including the wave profile, and mooring system. The properties of fluids inside the wash tank and specifications of the wash tank are given in Tables 14 and 15. The wash-tank was located mid-section of a barge-type FPSO. Two cases of different wave headings were considered, Beam-sea and Head-sea. Generally, a ship-type FPSO operates under a head sea condition, however, the beam sea condition is also considered for more violent cases.

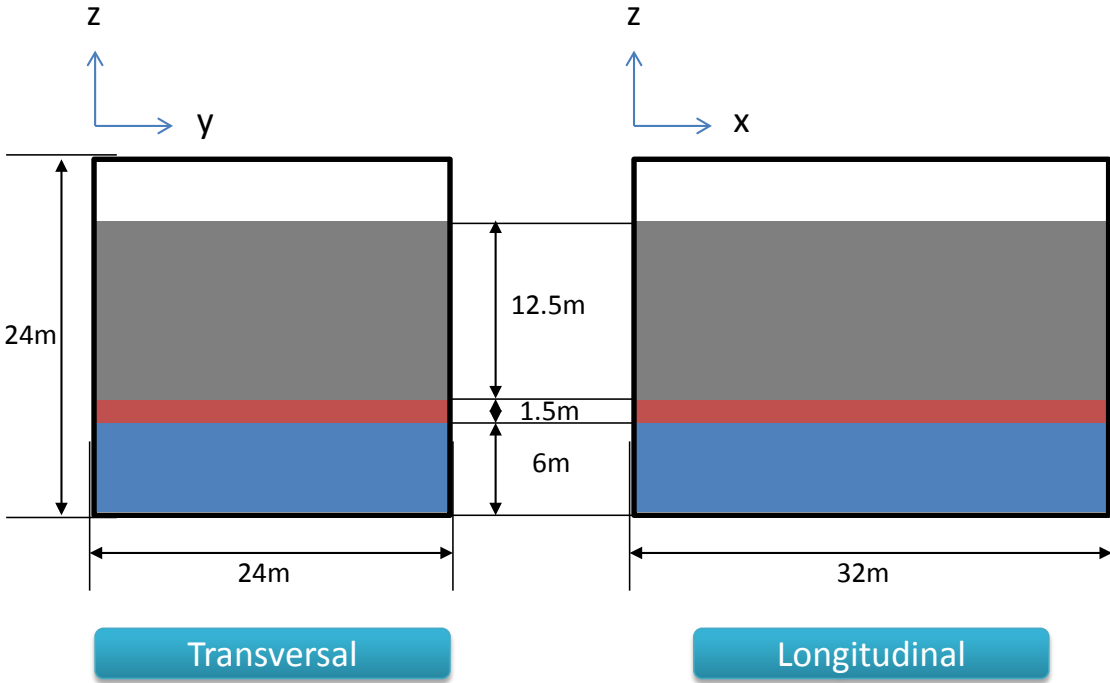


Figure 62 Schematic model for wash-tank

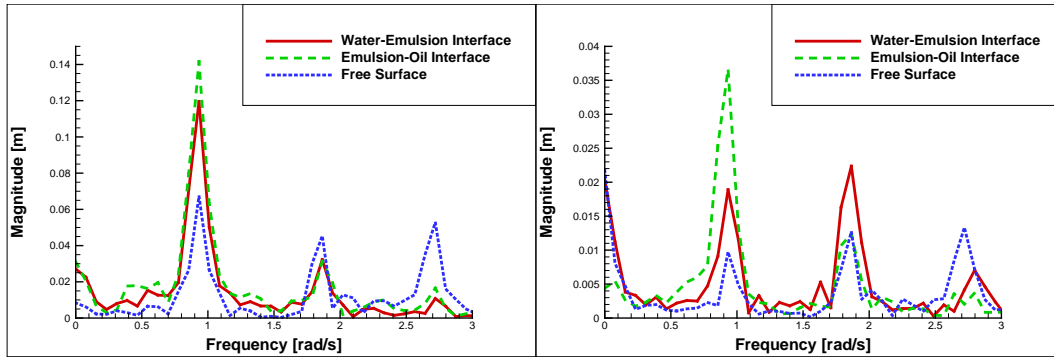


Figure 63 Spectra of wash-tank from free decay test at (a) left-wall and (b) center

Table 12 Angular Frequencies of Natural Modes of Wash Tank

Mode No.	Theoretical			Numerical (Free Decay Test)		
	ω_{oil}	$\omega_{emulsion}$	ω_{water}	ω_{oil}	$\omega_{emulsion}$	ω_{water}
1	0.9608	0.1767	0.0578	0.9307	-	0.0786
2	1.3878	0.2836	0.1128	1.2601	-	-
3	1.6998	0.3491	0.1643	-	0.3718	-
4	1.9627	0.3957	0.2122	1.866	0.3943	0.2287
5	2.1944	0.4326	0.2568	2.266	-	-

Table 13 Simulation Conditions of Vessel motion

Wave	Heading	180 degree (head) 90 Degree (Beam)
	Significant Height	5.0 m
	Peak Period	12 sec
	JONSWAP Spectrum overshoot parameter	3.0
Filling Ratio	83.3% (25%-S, 6.2%-E, 52.1%-C)	

Table 14 Properties of Inner Fluids

	Density	Kinematic viscosity	Surface Tension
Sea Water	$1025 \text{ kg} / \text{m}^3$	$1.0 \times 10^{-6} \text{ m}^2 / \text{s}$	$0.072 \text{ N} / \text{m}$
Ethylene-Vinyl acetate Copolymer	$950 \text{ kg} / \text{m}^3$	$4.43 \times 10^{-7} \text{ m}^2 / \text{s}$	$0.032 \text{ N} / \text{m}$
Crude Oil	$900 \text{ kg} / \text{m}^3$	$1.0 \times 10^{-4} \text{ m}^2 / \text{s}$	$0.0379 \text{ N} / \text{m}$

Table 15 Specifications of Wash Tank

Designation	Magnitude
Tank aft from aft perpendicular	143.0 m
Tank bottom from keel line	2.0 m
Tank Length, Breadth and Height	$32 \text{ m} \times 24 \text{ m} \times 24 \text{ m}$

The coupled program is used not only to simulate ship-motions influenced by the sloshing effect, but also to measure oscillations of interfaces to reflect the design for a proper wash-tank. The interface oscillations are measured at the left wall of the tank and they are plotted in Figs. 64 and 66. Their spectra are shown in Figs. 65 and 67. Interestingly, under the beam-sea condition, oscillation of the free surface is much larger than that of other interfaces due to violent motions; however, under relatively mild conditions including the head-sea condition, all interfaces have similar amplitudes of interface elevation. It is obvious that the wave profile is the same for both cases; the trends of internal waves are similar to each other except for magnitude.

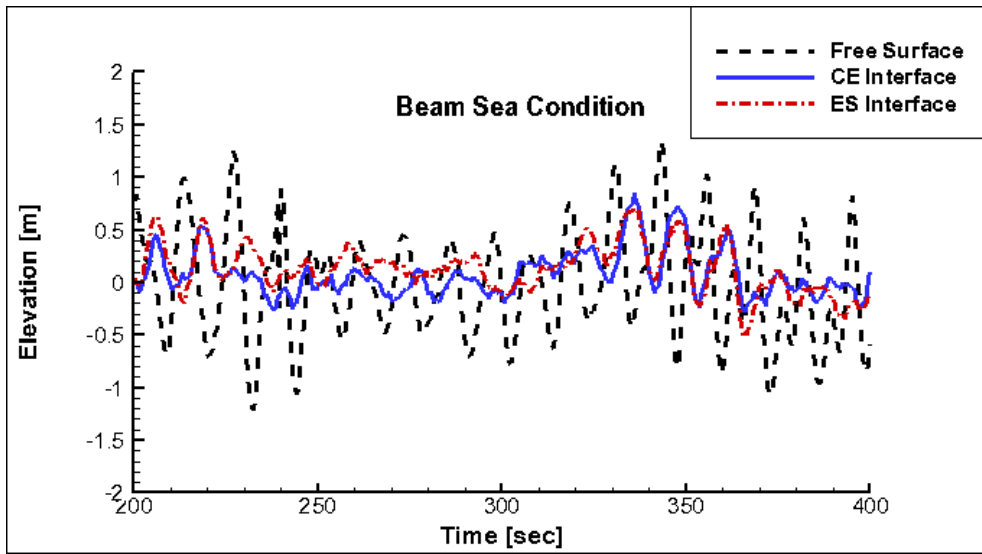


Figure 64 Elevations of interface for beam-wave

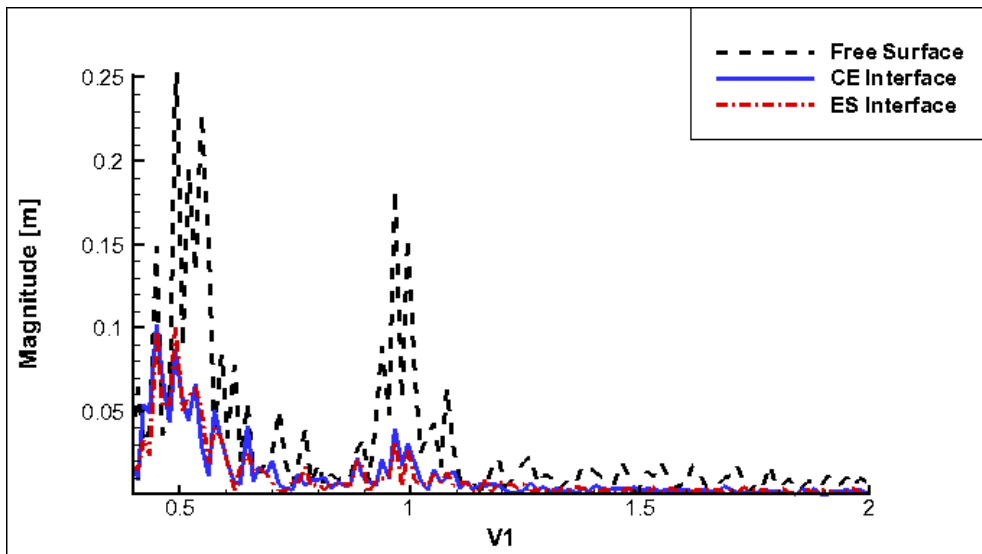


Figure 65 Spectra of interface for beam-wave

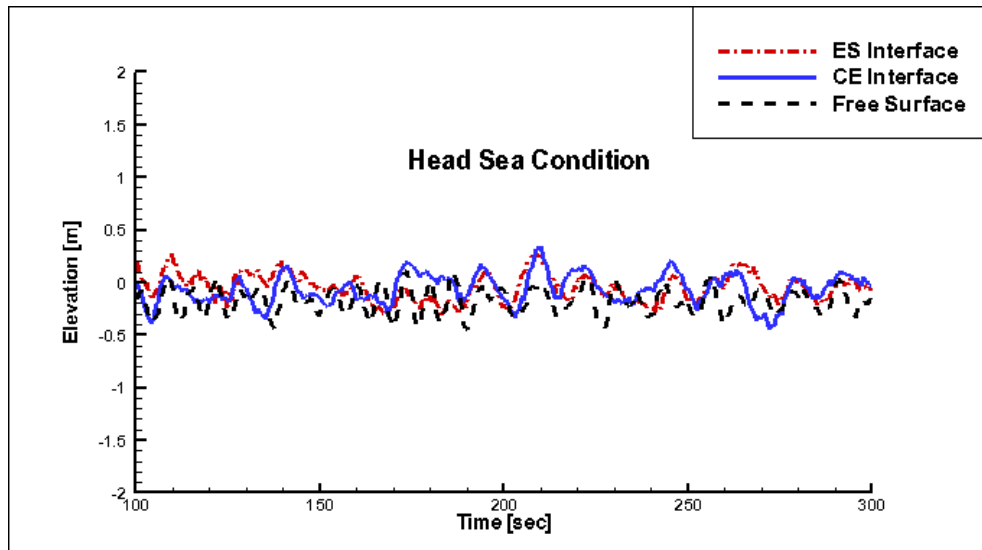


Figure 66 Elevations of interface for head-wave

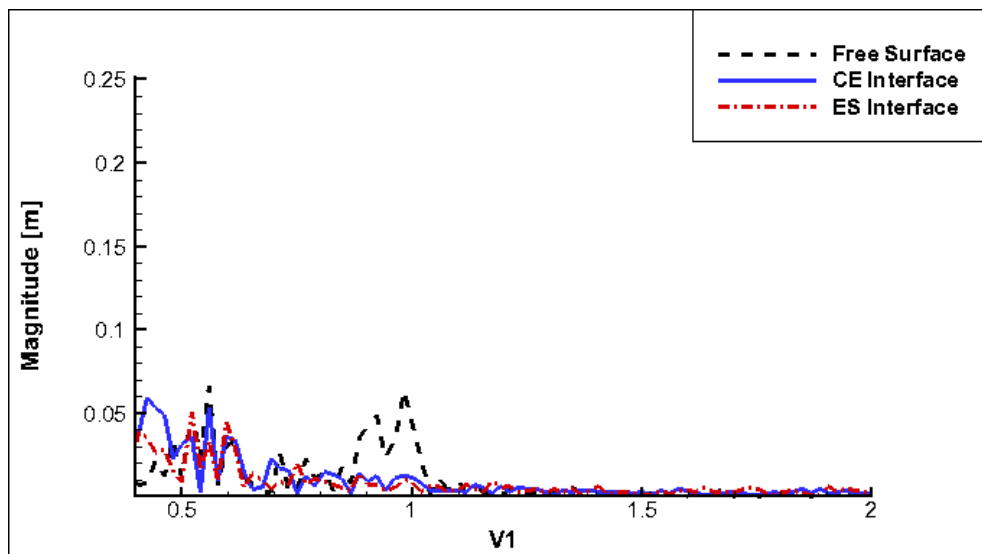


Figure 67 Spectra of interface for head-wave

After obtaining the natural frequencies of the wash tank, the fully coupled program between the ship-motion and the multi-liquid sloshing is simulated. Figs. 68

and 69 show vessel motion histories under beam-sea and head-sea conditions, respectively. Since the incoming waves are irregular, the motions of inner liquids are also very irregular. Ship-shaped floating structures are vulnerable to beam waves due to an aspect ratio of the vessel. In this regard, the case of beam wave has larger motion than that of head wave; thus the inner liquid motions become violent in the case of beam wave. The interesting point of the present simulation is that the oscillation of free surface is much larger than others under violent motions. On the other hand, all oscillations of interface are almost identical to each other under mild motions. The RAOs of motions can be calculated by the method suggested by Blackman and Tukey (1958). The calculated RAOs are compared by the different wave headings as shown in Fig. 70. The maximum roll angle and standard deviation for the case of beam-wave are 5.79-degrees and 1.85-degrees, respectively. For the case of head-wave, the maximum pitch angle and standard deviation are 0.86-degrees and 0.22-degrees, respectively.

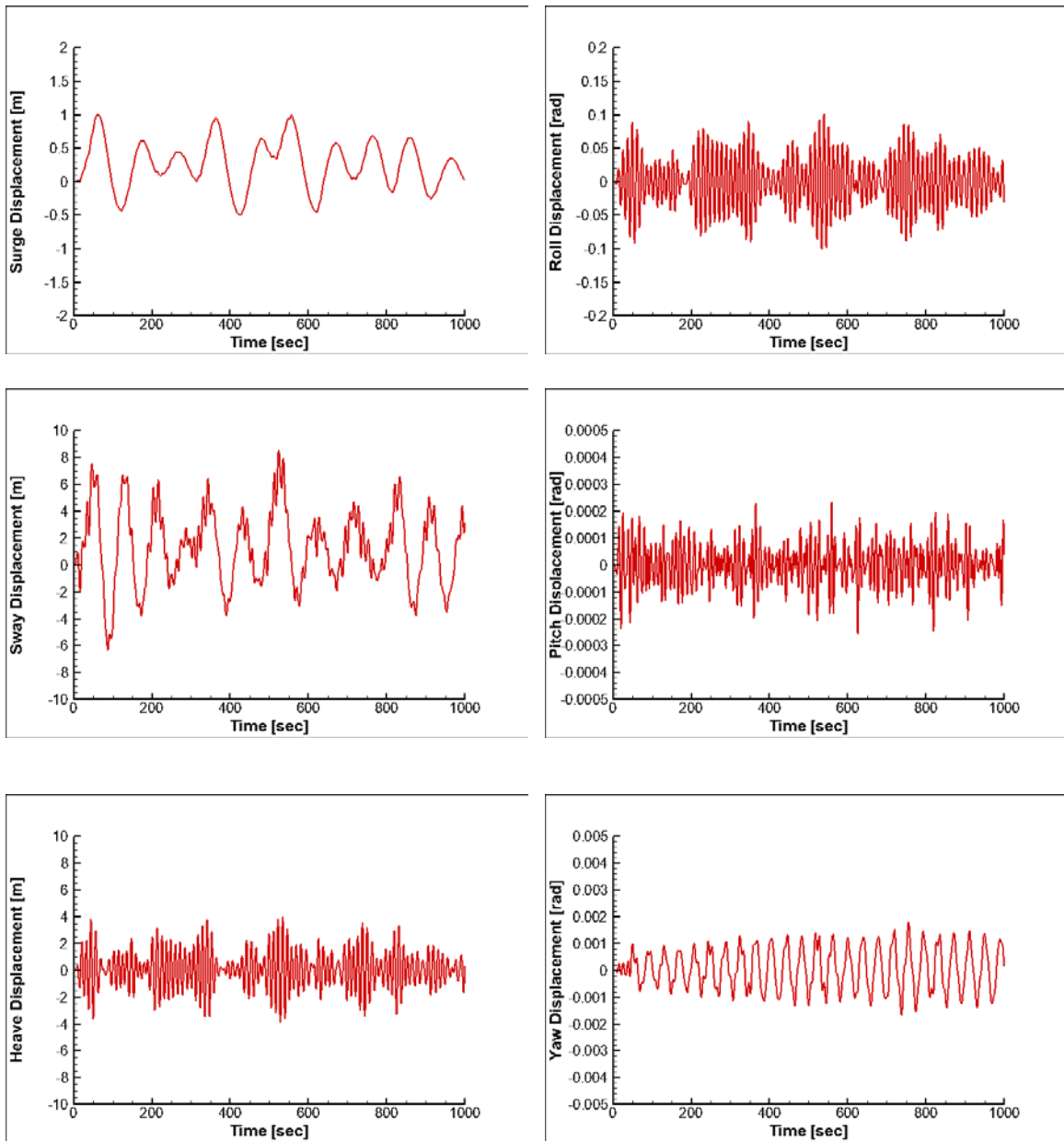


Figure 68 Displacements of vessel at beam-sea condition

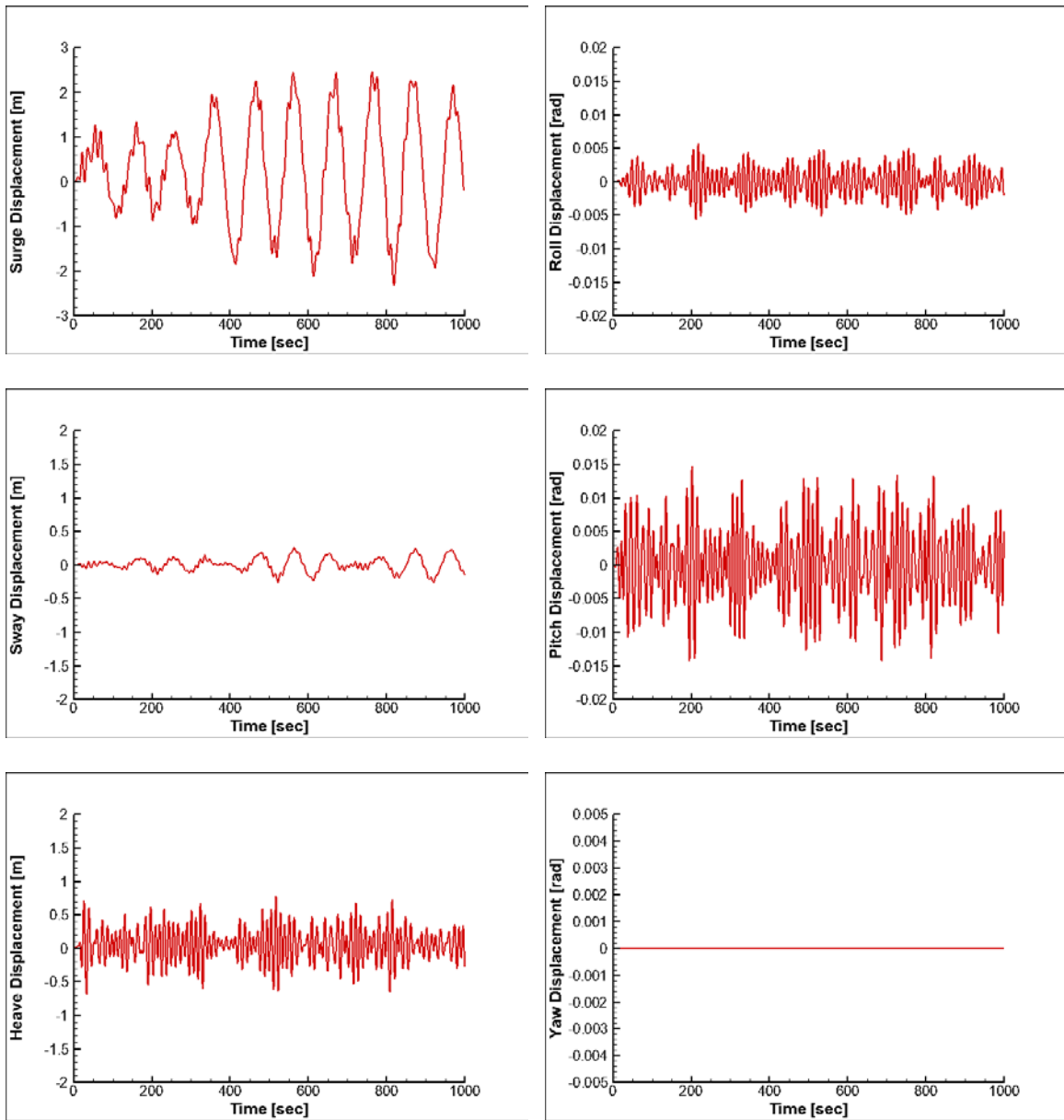


Figure 69 Displacement of vessel at head-sea condition

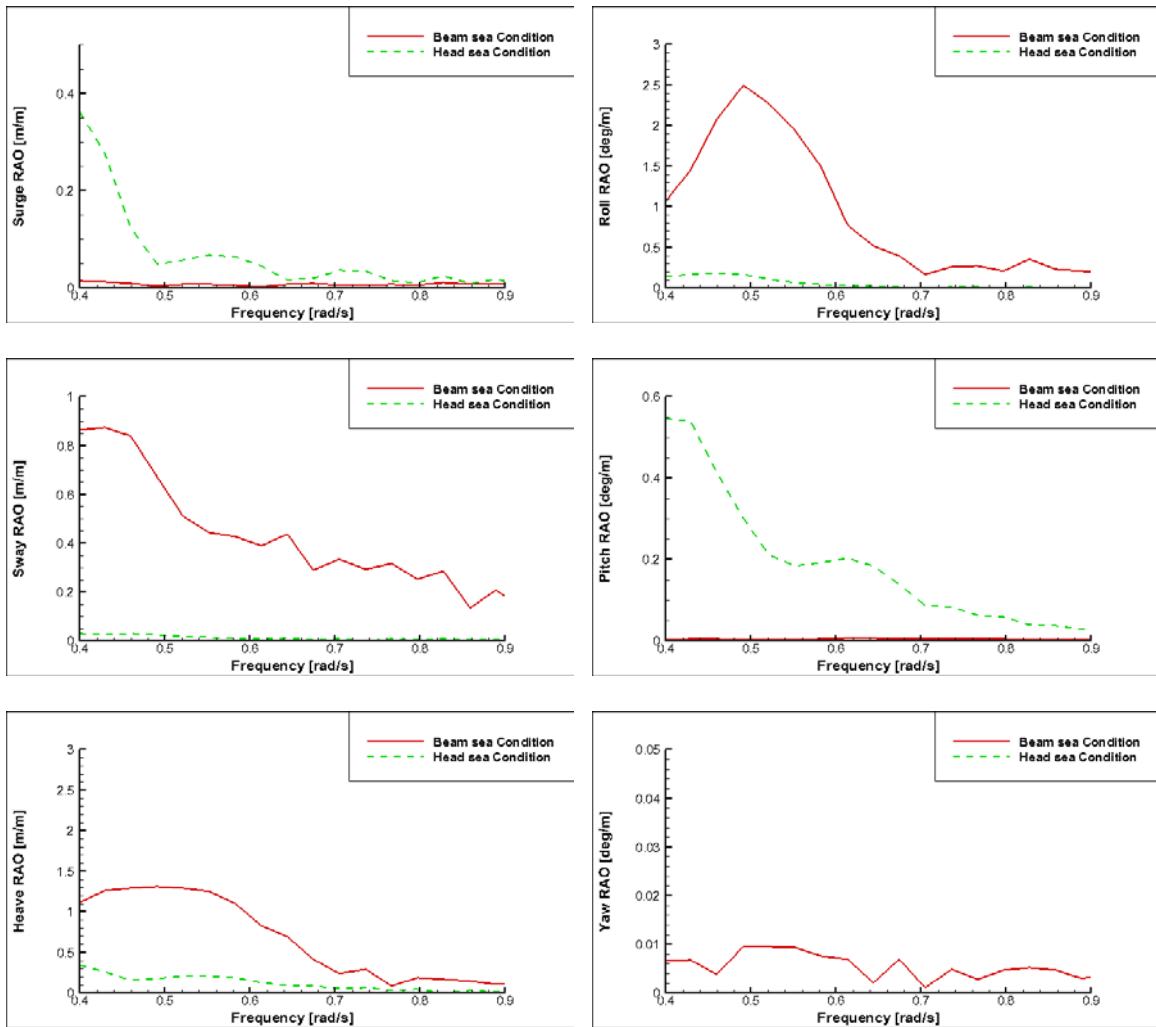
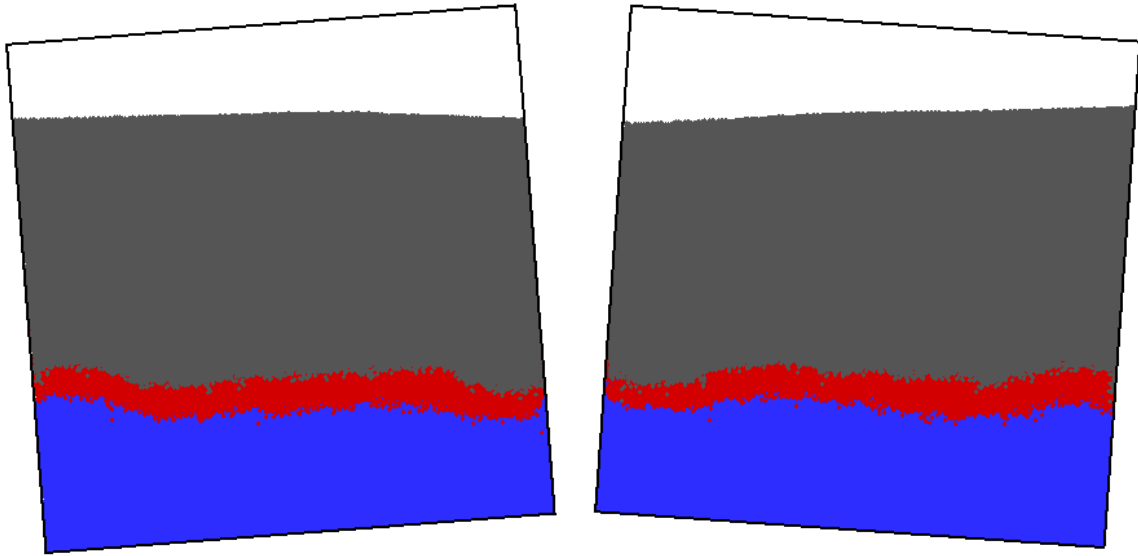


Figure 70 Comparisons of RAOs

In order to investigate the sloshing effects more clearly, the cases of liquid- and rigid-cargos were simulated and compared. The latter is the simplest approximation one can use without a more sophisticated sloshing program. In this method, the inner liquids are regarded as large block with the same density of fluids and they are rigidly connected to the tank wall. Subsequently, only inertia forces and moments were considered; this means that the impact loads induced by sloshing were not contemplated. Nevertheless,

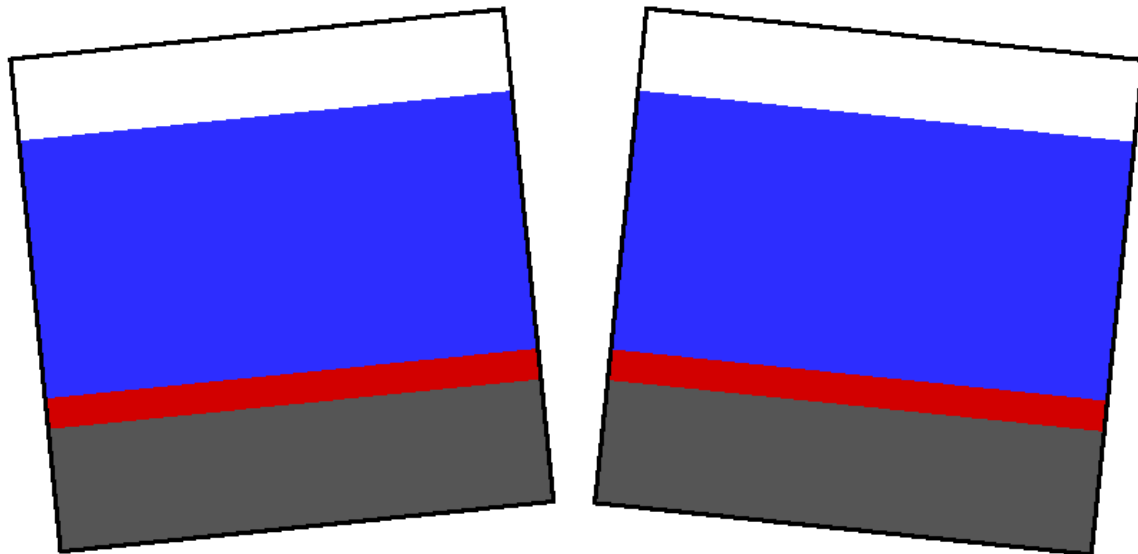
the inertia forces and moments were included to external forces of the ship motion program, but the free surface effects were not considered when calculating them. Figs. 71 and 72 show snapshots for the two cases. In the rigid cargo case, the interfaces did not fluctuate as expected. On the other hand, inner liquids are deformed by tank motion and the free surface and interfaces also fluctuate. Along the deformed liquid shape, the inertia forces and moments can be changed; thus the two cases have different inertia forces and moments. Since the ship-type FPSO is sensitive to roll motion, the beam wave is considered as incoming waves. The simulation condition is the same as already mentioned above. Figs. 73 and 74 represent the comparison of displacement and RAOs between two cases of roll, respectively. According to comparisons of displacement and RAOs, interestingly, liquid cargo reduces vessel roll motion, similar to a passive anti-rolling tank which can potentially be extra advantage of including the wash tank inside the hull. Additionally, the peak frequency is also slightly shifted to a higher frequency. In the case of rigid cargo, the maximum roll angle and standard deviation are 7.45-degrees and 2.38-degrees. This example explains that the simple approximation using equivalent rigid cargo and ignoring effects of liquid sloshing cannot guarantee reliability in the design stage.



(a)

(b)

Figure 71. Snapshots of inner liquid cargo in wash tank



(a)

(b)

Figure 72 Snapshots of inner solid cargo in wash tank

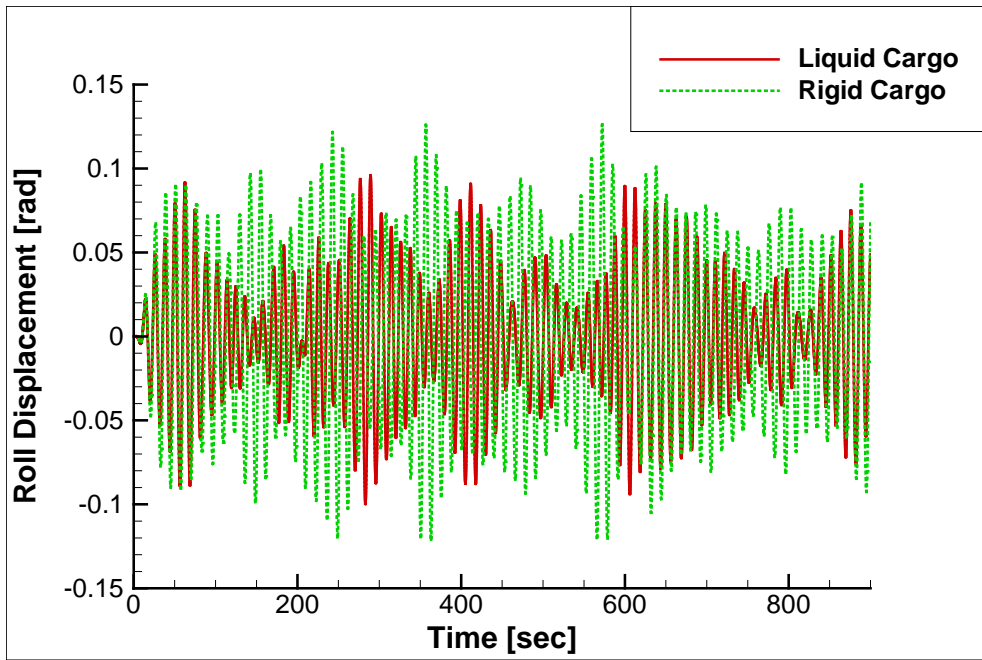


Figure 73 Roll Motion history for liquid- and rigid-cargo

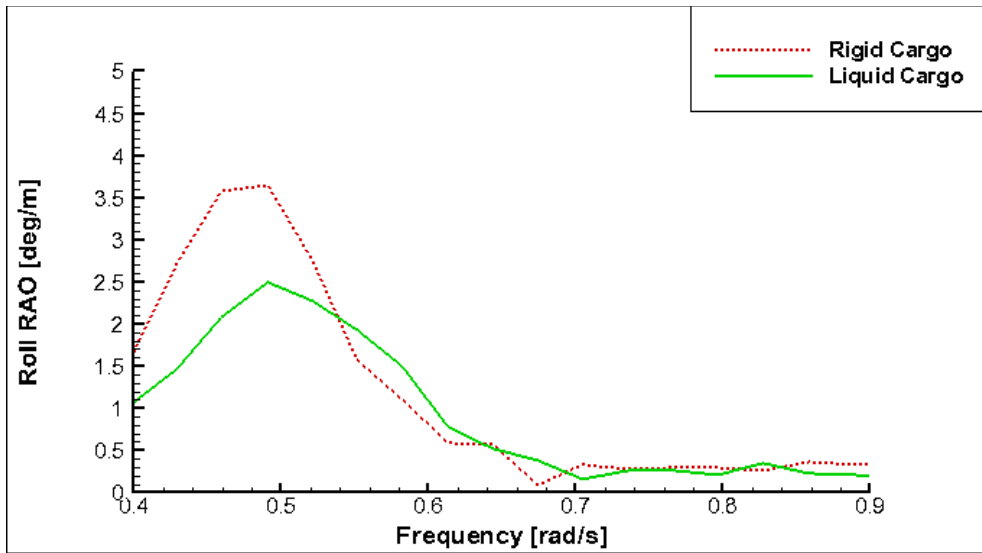


Figure 74 Comparison of roll RAO between liquid- and rigid-cargo

Now the operational condition of the floating structure has been considered. Previous cases (HS=5m, TP=12s) have assumed violent conditions, and actually under violent conditions, most floating structures stop operation to avoid accidents. In this regard, vessel motion analysis coupled with sloshing is usually necessary to estimate operational limits with proper predictions. The HS=2m and TP=7s are used in this simulation for operational condition of FPSO. Figs. 75 and 76 show vessel motion history and its RAOs. The maximum angle and standard deviation for the roll motion are 0.11-degrees and 0.023-degrees, respectively. Fig. 76 represents roll RAO and shows that the resonant was seen near the frequency 5.54-rad/s. Another interesting point in present case is that the elevation amplitude of interfaces is similar to that of violent condition although the roll displacement of operational condition is much less than that of violent condition which is shown in Figs. 77 and 78. In this regard, inner liquids behavior should be considered although the ship motion is small. In other words, not only proper analysis of coupling is required, but appropriate prediction of sloshing motion should be considered.

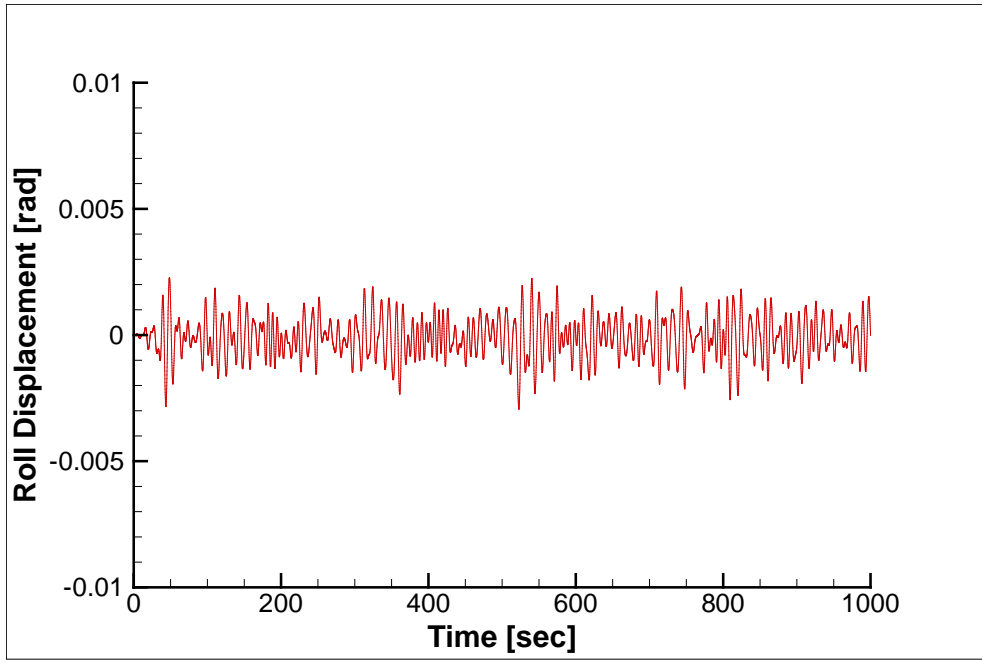


Figure 75 Roll Displacement under operational condition

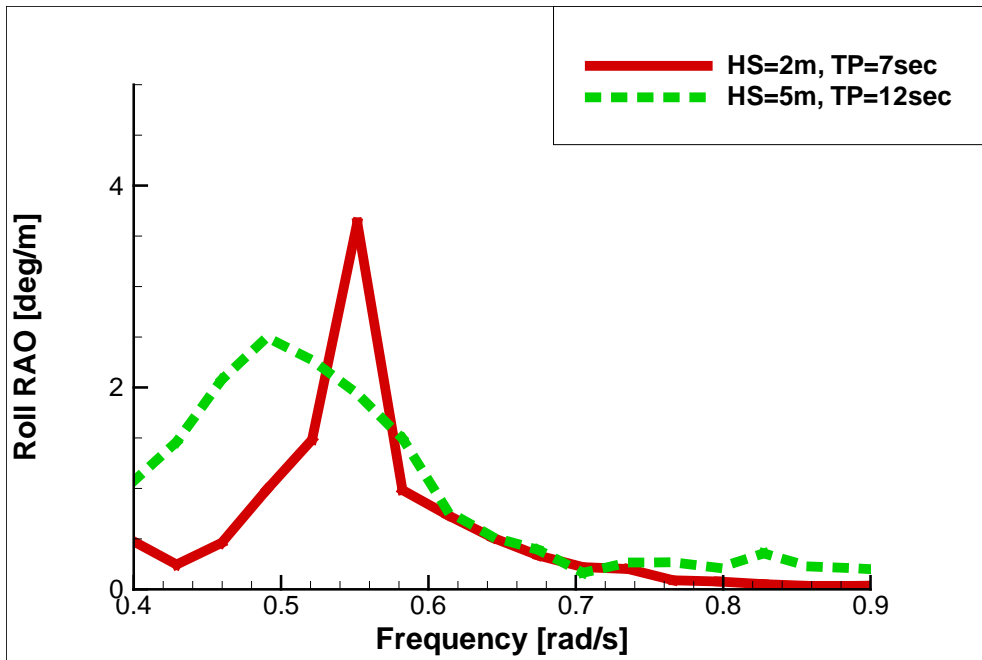


Figure 76 Comparisons of roll RAOs between severe and operational condition

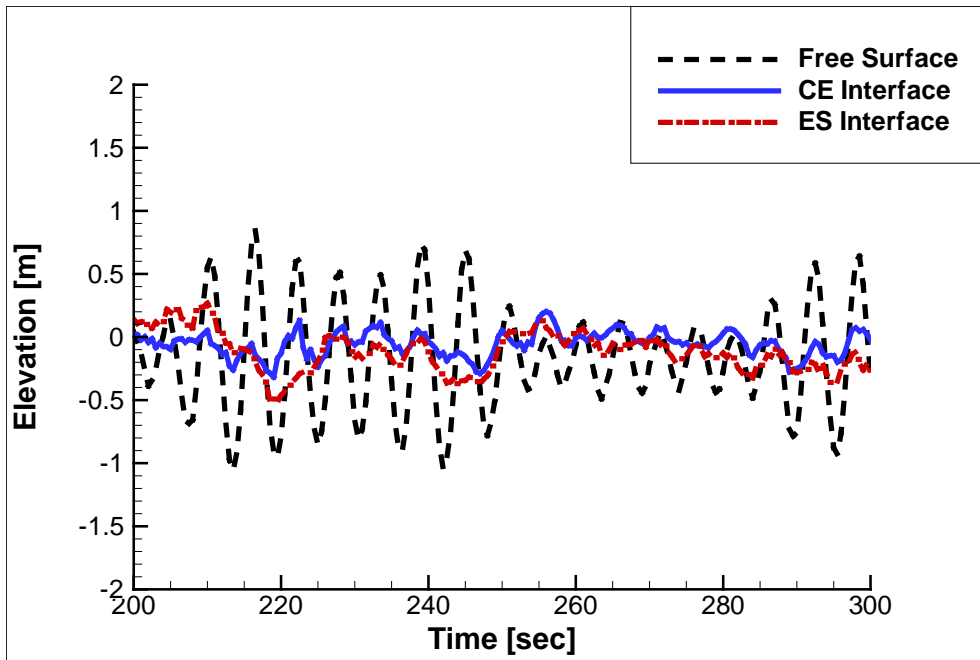


Figure 77 Elevation of interfaces under operational condition

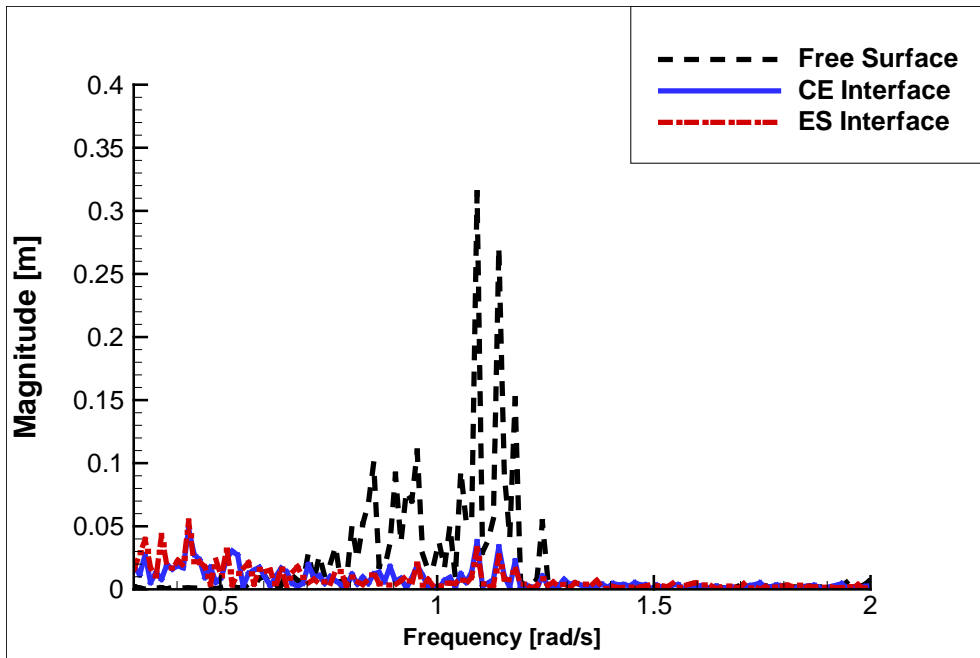


Figure 78 Spectra of interfaces under operational condition

CHAPTER VI

CONCLUSION

The sloshing effects with free surface fragmentation were investigated numerically by using a Lagrangian-based particle program, MPS originally proposed by Koshizuka and Oka (1996). In the MPS, all terms of governing equations are replaced with particle interaction models. The particle interaction models consist of gradient, collision, Laplacian, and incompressibility. Moreover, boundary conditions at wall and free surface were also considered. The free surface searching method was required to account for applying free-surface boundary conditions.

The improvement of MPS was achieved by (a) modifying Poisson source terms to reduce non-physical pressure fluctuation, (b) finding proper parameters for the collision model and free surface searching method, and (c) adding a hydrostatic pressure correction model to correct hydrostatic pressure from excluding the weight of the free surface particle due to the free surface boundary condition. The improved MPS was used to simulate well-known examples for validation such as dam breaking, and sloshing under harmonic tank motion. The obtained results were compared with corresponding experiments. Since the MPS is based on the Lagrangian approach, the violent fluid behaviors (i.e. wave breaking, splash, over-turning, etc.) can be demonstrated without special mathematical treatment between grids which was used in conventional CFD. Not only were liquid motions well-agreed with experiments, but the impact loads induced by collision between fluids and solid particles also had good agreement with the experiment.

The aforementioned MPS program was developed to extend its applicability and performance to multi-liquid systems. The new MPS method for multi-liquid systems includes (a) extra search methods for interface particles, (b) boundary condition at interface, (c) buoyancy-correction, and (d) a surface tension model for interface particles. The extra search method for interface can be accomplished by modifying the free surface searching method with extra criteria for the interface particle. The kinematic boundary conditions at interface can be satisfied by tracing the interface particle directly; however, the dynamic boundary condition can be satisfied by carrying out an imaginary particle across the interface layer exactly the same distance as the averaged physical quantities. The concept of self-buoyancy was considered to resolve underestimated buoyancy forces due to a numerical configuration disorder. Finally, a surface tension model was used to reduce the amplitude of short waves at interface. According to the description of the Kelvin-Helmholtz instability, the growth-rate can reach infinity unless surface tension is applied. The newly developed MPS for multi-liquid system is demonstrated through simulation of three-liquid sloshing; then the obtained results are compared against experimental results. The comparisons show that numerical results are well matched with the experimental results.

The interaction between ship motion and inner-tank liquid sloshing were investigated in the present study. The potential based BEM ship motion program, CHARM3D, is used to analyze vessel motion in an irregular sea state. Before coupling the two programs, the reliability of each program was fully verified with corresponding experimental results. The two programs were then coupled to exchange respective data

at each time stop. All the hydrodynamics coefficients were obtained by a 3-dimensional panel-based radiation/diffraction program, called WAMIT, in the frequency domain; and all the corresponding coefficients were converted in order to be used in the time domain. A fully coupled program between ship motion and sloshing using MPS was simulated for dynamic analysis for various filling ratios of liquid cargo. Results from numerical simulation were compared with the respective experimental results conducted by MARIN. Through the comparisons, it was seen that the predicted results correlated well with the measured data. The sensitivity of the amount of liquid cargo was observed in both numerical and experimental results. Especially, the roll RAOs can be increased by a factor of 2 or 3 in some wave frequency ranges compared to the bare-hull case. The nonlinearity of sloshing effects is also clearly manifested. It can vary the RAOs in relatively high waves with a peak period near the resonant frequency of sloshing. Furthermore, in order to see the influence of the liquid cargo and its sloshing effects more clearly, the case was compared to the case of rigid cargo. In the case of rigid cargo, the liquid in the sloshing tanks was regarded as one large solid block connected to the tank wall. The comparison clearly demonstrates the need for reliable vessel-motion/liquid-sloshing coupled dynamic analysis programs.

The case of multi-liquid sloshing was also studied in the present research account of the wash tank inside the hull. The coupling method between the ship motion program and the sloshing program was exactly the same manner as mentioned above; the only difference is that the MPS for the multi-liquid was used for the sloshing analysis. Two cases with different wave headings are simulated numerically, and the comparison

shows that the case under the head sea condition was much more robust than that in the beam sea condition due to the shape of the floating body. This robustness is due to the relatively mild motion of the vessel; a typical operation sea state with beam-wave was simulated. The vessel motions with the three liquids cargo and the corresponding solid cargo were also compared. It is seen that the liquids cargo can also function as a passive anti-rolling device. The simplest approximation method using the equivalent rigid cargo can be unreliable in the design stage. This coupled simulation also reproduced vessel motions under typical operational sea state and the results were compared with a severe case. In the comparison of RAOs between cases of operational and survival conditions, the resonant frequency can be changed by different sea states. Furthermore, since the vessel motions are much smaller than severe condition, the interface elevations have similar amplitude. In this regard, case studies for applicable conditions should be incorporated in the design stage.

In the future, more realistic sloshing simulations including a 3-dimensional sloshing tank, on- and off-loading configurations, and oil/gas leakage from a damaged vessel, will be investigated with this coupled program. As size of the liquid tank increased, 3-dimensional effects also rise to become one of the important factors. The present study has used the 2-dimensional sloshing program with equivalent effects of 3-dimensional. Thus far, 2-dimensional sloshing can be an appropriate method to predict the global motions of vessel equipped liquid tanks, yet 3-dimensional effects should be considered when the liquid tank becomes large enough to consider this issue. Additionally, with oil leakage from the damaged vessel, the hole would be relatively

much smaller compared to the tank. Therefore, 3-dimensional simulation can be used rather than 2-dimensional program in special cases.

REFERENCES

- Abramson, H.N., Bass, R.L., Faltinsen, O., and Olsen, H.A., (1974), "Liquid slosh in LNG carrier," In: *Proceedings of 10th Symposium on Naval Hydrodynamics*, pp. 371-388
- Arcandra, T., (2001), "Hull/Mooring/Riser coupled dynamic analysis of a deepwater floating platform with polyester lines," Ph.D Dissertation, Texas A&M University, College Station
- Barnea, D., and Taitel, Y., (1993), "Kelvin-Helmholtz stability criteria for stratified flow: viscous versus non-viscous (inviscid) approaches," *Int. J. Multiphase Flow*, Vol. 19, No. 4, pp. 639-649
- Blackman, R.B., and Tukey, J.W., (1958), "The measurement of power spectra from the point of view of communications engineering," *Bell System Technical Journal*, Vol. 37, pp. 185-282
- Chen, H.C., (2011), "CFD Simulation of compressible two-phase sloshing flow in a LNG tank," *Ocean Systems Engineering*, Vol. 1, No. 1, p. 29-55
- Cho, S., Hong, S.Y., Kim, J., and Park, I., (2007), "Studies on the coupled dynamics of ship motion and sloshing including multi-body interactions," In: *Proceedings of the Seventeenth International Offshore and Polar Engineering Conference*, Lisbon, Portugal, ISOPE, Vol. 3, pp. 1900-1904
- Funada, T., and Joshep, D.D., (2001), "Viscous potential flow analysis of Kelvin-Helmholtz Instability in a channel," *Journal of Fluid Mechanics*, Vol. 445, pp. 263-283
- Gaillarde, G., Ledoux, A., and Lynch, M., (2004), "Coupling between liquefied gas and vessel's motion for partially filled tanks: Effect on seakeeping," *Design & Operation of Gas Carriers*, The Royal Institution of Naval Architects, London, UK
- Gotoh, H., (2009), "Lagrangian particle method as advanced technology for numerical wave flume," *International Journal of Offshore and Polar Engineering*, ISOPE, Vol. 19, No. 3, pp. 161-167
- Hu, X. Y. and Adams, N. A., (2006), "A multi-phase SPH method for macroscopic and mesoscopic flows," *Journal of Computational Physics*, Vol. 213, No. 2, pp. 844-861
- Hwang S.C., Lee, B.H., Park J.C., and Sung H.G., (2010), "Particle-Based Simulation for sloshing in a rectangular tank," *Korean Society of Ocean Engineering*, Vol. 24, No. 2, pp. 964-989

- Joseph D.D., and Liao, T.Y., (1994), "Potential flows of viscous and viscoelastic fluids," *Journal of Fluid Mechanics*, Vol. 265, pp. 1-23
- Kang, H.Y., and Kim, M.H., (2011), "Hydrodynamic interactions and coupled dynamics between a container ship and multiple mobile harbors," *Ocean Systems Engineering, An International Journal* Vol. 2, No. 3, 217-228
- Khayyer, A., and Gotoh, H., (2013), "Enhancement of performance and stability of MPS mesh-free particle method for multiphase flows characterized by high density ratios," *Journal of Computational Physics*, Vol. 242, No. 1, pp.211-233
- Kim, M.H., (1992), "Difference-frequency wave loads on a large body in multi-directional waves," *Applied Ocean Research*, Vol. 14, pp. 353-370
- Kim, M.H., Ran, Z., Zheng, W., Bhat, S., and Beynet, P., (1999), "Hull/mooring coupled dynamic analysis of a truss spar in time-domain," In: *Proceedings of the International Offshore and Polar Engineering Conference*, ISOPE, Vol. 1, pp. 301-308
- Kim, K.S., Lee, B.H., Kim, M.H., and Park, J.C., (2011), "Simulation of sloshing effect on vessel motions by using MPS (Moving Particle Simulation)," *Computer Modeling in Engineering and Sciences*, Vol. 79, No 3, pp. 201-221
- Kim, K.S., Kim, M.H., and Park, J.C., (2013), "Dynamic coupling between ship motion and three-layer-liquid separator by using MPS (Moving Particle Simulation)," In: *Proceedings of the Twenty-Third International Offshore and Polar Engineering Conference*, ISOPE, Anchorage, Alaska, USA, Vol. 3, pp. 366-371
- Kim, W.J., and Lee, Y.Y., (2001), "A preliminary study for the prediction of leaking-oil amount from ruptured tank," *Journal of The Korean Society of Marine Environmental Engineers*, Vol. 4, pp. 21-31
- Kim, Y., Shin, Y., Kin, W., and Yue, D., (2003), "Study on sloshing problem coupled with ship motion in waves," *The 8th International Conference on Numerical Ship Hydrodynamics*, Busan, Korea
- Kim, Y., Nam, B.W., Kim, D.W., Kim, Y.S., (2007), "Study on coupling effect of ship motion and sloshing," *Ocean Engineering*, Vol. 34, pp. 2176-2178.
- Kishev, Z., Hu, C., and Kashiwagi, M., (2006), "Numerical simulation of violent sloshing by a CIP-based method," *Journal of Marine Science and Technology*, Vol. 11, No. 2, pp. 111-122

- Koshizuka, S., Tamako, H. and Oka, Y., (1995), "A particle method for incompressible viscous flow with fluid fragmentation," *Computational Fluid Dynamics Journal*, Vol. 4, pp. 29-46
- Koshizuka, S., and Oka, Y., (1996), "Moving particle semi-implicit method for fragmentation of incompressible fluid," *Numerical science and Engineering*, Vol. 123, No. 3, pp. 421-434
- La Rocca M., Sciortion, G., Adduce, C., and Boniforti, M.A., (2005), "Experimental and theoretical investigation on the sloshing of a two-liquid system with free surface," *Physics of Fluids*, 17, 062101, [DOI: 10.1063/1.1922887]
- Lamb, H., (1945), *Hydrodynamics*, Cambridge Univ. Press.
- Lee, B.H., Park, J.C., and Kim, M.H., (2010), "Numerical simulation of impact loads using a particle method," *Ocean Engineering*, Vol. 37, No. 2, pp.164-173
- Lee, B.H., Hwang, S.C., Nam, J.W., and Park, J.C., (2011), "Numerical prediction for the performance of a floating-type breakwater by using a two-dimensional particle method," *International Journal of Ocean System Engineering*, Vol. 1, No. 1, pp. 36-44
- Lee, B.H., Park, J.C., Kim, M.H., and Hwang, S.C., (2011), "Step-by-step improvement of MPS method in simulating violent free-surface motions and impact-loads," *Journal of Methods in Applied Mechanics and Engineering*, Vol. 200, No. 9, pp.1113-1125
- Lee, C.H., Newman, J., Kim, M.H., Yue, D.K.P., (1991), "The computation of second-order wave loads," In: *the 10th International Conference on Offshore Mechanics and Arctic Engineering*, Stavanger, Norway, pp. 113-123
- Lee, S.J. and Kim, M.H., (2010), "The effects of inner liquid motion on LNG vessel responses," *Journal of Offshore Mechanics and Arctic Engineering*, Vol.132, No. 2, 021101, [DOI: 10.1115/1.4000391]
- Loysel, T., Gervaise, E., Moreau, S. and Brosset, L., (2013), "Results of the 2012-2013 sloshing model test benchmark," In: *Proceedings of the Twenty-Third International Offshore and Polar Engineering Conference*, ISOPE, Anchorage, AK, U.S.A, Vol. 3, pp. 141-152
- Miles, J.W., (1959), "On the generation of surface waves by shear flows, part 3. Kelvin-Helmholtz instability," *Journal of Fluid Mechanics*, Vol. 6, No. 4, pp. 583-598

- Molin, B., Remy, F., Audiffren, C., and Marcer, R., (2012), "Experimental and numerical study of liquid sloshing in a rectangular tank with three fluids", in: *Proceedings of the Twenty-Second International Offshore and Polar Engineering Conference*, ISOPE, Rhodes, Greece, Vol. 3, pp. 331-340
- Monaghan, J.J., (1985), "Particle methods for hydrodynamics," *Computer Physics Report*, Vol. 3, pp. 71-124
- Monaghan, J.J., (1988), "An introduction to SPH," *Computer Physics Communications*, Vol. 48, pp. 89-99
- Monaghan, J.J., and Kocharyan, A., (1995), "SPH simulation of multi-phase flow," *Computer Physics Communications*, Vol. 87, No. 1, p. 225-235
- Newman, J.N., (1967), "Drift force and moment on ships in waves," *Journal of Ship Research*, Vol. 11, pp. 51-60
- Newman, J.N., (2005), "Wave effects on vessels with internal tanks," In: *The 20th Workshop on Water Waves and Floating Bodies*, Spitsbergen, Norway
- Nomura, K., Koshizuka, S., Oka, A., and Obata, H., (2001), "Numerical analysis of droplet breakup behavior using particle method," *Journal of Nuclear Science and Technology*, Vol. 38, No. 12, pp. 1057-1064
- Ogilvie, T.F., (1983), "Second-order hydrodynamics effects on ocean platforms," In: *International Workshop on ship and platform Motions*, Berkeley, pp. 205-265
- Sueyoshi, M. and Naito, S., (2003), "A Numerical Study of Violent Free Surface Problem with Particle method for Marine Engineering," In: *Proceedings of 8th Numerical Ship Hydrodynamics*, pp. 330-339
- Shakibaeinia, A., and Jin, Y.C., (2012), "MPS mesh-free particle method for multiphase flows," *Computational Methods in Applied Mechanics and Engineering*, Vol. 229, pp. 13-26
- Shirakawa, N., Horie, H., Yamamoto, Y., and Tsunoyama, S., (2001), "Analysis of the void distribution in a circular tube with the two-fluid particle interaction method," *Journal of Nuclear Science and Technology*, Vol. 38, No. 6, pp. 392-402
- Tahar, A., and Kim, M.H., (2003), "Hull/mooring/riser coupled dynamic analysis and sensitivity study of a tanker-based FPSO," *Journal of Applied Ocean Research*, Vol. 25, No. 6, pp. 367-382

- Tanaka, M., and Masunaga, T., (2010), “Stabilization smoothing of pressure on MPS method by quasi-compressibility,” *Journal of Computational Physics*, Vol. 229, No. 311, pp. 4279-4290
- Toyota, E., Akimoto, H. and Kubo, S., (2005), “A particle method with variable spatial resolution for incompressible flows,” In: *Proceedings of 19th Japan Society of Fluid Mechanics*, A9-2
- Wehausen, J.V., (1971), “The motion of floating bodies,” *Annual Review of Fluid Mechanics*, Vol. 3, No. 1, pp. 237-268
- Yang, C.K. and Kim, M.H., (2011), “The Structural safety assessment of a tie-down system on a tension leg platform during hurricane events,” *Ocean Systems Engineering, An International Journal*, Vol. 1, No. 4, 263-293